Design and Evaluation of a Quasi-Passive Variable Stiffness Ankle-Foot Prosthesis to Improve Biomechanics Across Walking Speeds

by

Emily Rogers-Bradley

S.B., Harvard University (2015)
S.M., Massachusetts Institute of Technology (2019)

Submitted to the Department of Mechanical Engineering
in partial fulfillment of the requirements for the degree of

Doctor of Philosophy

at the

MASSACHUSETTS INSTITUTE OF TECHNOLOGY

February 2023

© Massachusetts Institute of Technology 2023. All rights reserved.

Author .....
Department of Mechanical Engineering
January 11, 2023

Certified by .....
Hugh M. Herr
Professor, Program in Media Arts and Sciences
Thesis Supervisor

Accepted by .....
Nicolas Hadjiconstantinou
Chair, Department Committee on Graduate Theses

Design and Evaluation of a Quasi-Passive Variable Stiffness Ankle-Foot Prosthesis to Improve Biomechanics Across Walking Speeds

by

Emily Rogers-Bradley

Submitted to the Department of Mechanical Engineering
on January 11, 2023, in partial fulfillment of the
requirements for the degree of
Doctor of Philosophy

Abstract

Currently there are an estimated 875,000 people with major lower limb loss in the United States, with numbers projected to increase 1.6-fold by 2050 due to increasing prevalence of diabetes, obesity, and related dysvascular conditions [1]. Lower limb amputation often leads to secondary conditions such as knee pain, knee osteoarthritis, osteopenia, back pain, postural changes, and general deconditioning [2]. For people with transtibial (below-knee) amputation, prevalence of knee osteoarthritis in the contralateral limb is 17x higher than in the general population, with 27% of people with unilateral amputation developing knee osteoarthritis [3]. This large increase in incidence is likely due to insufficient push-off power from the prosthesis and increased limb loading on the contralateral side [4].

This thesis presents an ankle-foot prosthesis which increases energy storage and return, increases peak power, and decreases contralateral limb loading in a low-mass, quasi-passive device. This is achieved by automatically adjusting prosthesis stiffness to maximize energy storage across walking speeds. A novel quasi-passive variable stiffness ankle-foot prosthesis is presented with high resolution stiffness adjustment from 352 - 479 Nm/radian, corresponding to biological ankle quasi-stiffness during level ground walking from 0.75 - 1.5 m/s for a 50th percentile male. This thesis presents the development of a novel mechanism for varying bending stiffness of leaf springs which utilizes independently controlled lockable linear actuators which constrain relative sliding of parallel leaf springs relative to a mechanical ground to control bending stiffness. The detailed device design and analysis of the variable stiffness ankle-foot prosthesis is described, including a parametric model for approximating device stiffness, contact stress analysis, fatigue life calculations, and bolted joint analysis. The benchtop testing results demonstrate that the device successfully achieves the targeted stiffness range, device mass, and structural integrity.

A study was conducted with 7 participants with unilateral transtibial amputation in order to evaluate the kinetic and kinematic effects of the variable stiffness prosthesis

during walking compared to a passive energy storage and return foot. During the experiment, subjects walked on an instrumented treadmill at the speeds of 0.75 m/s, 1.0 m/s, 1.25 m/s, and 1.5 m/s while force and motion data was recorded. This thesis presents results from the clinical study which demonstrate a 15.5 - 19.3% greater peak ankle angle during walking across all speeds with the variable stiffness ankle compared to a passive control, 5.4 - 14.8% greater peak joint power, 10.5 - 23.7% greater energy return, and a 4.0 - 6.7% lower contralateral limb knee external adduction moment across walking speeds.

This thesis presents the first of its architecture variable stiffness ankle-foot prosthesis utilizing a novel locking parallel leaf spring mechanism for stiffness control. The prosthesis has a lower device mass compared to existing powered and quasi-passive devices, and increases biomimetic functionality beyond standard passive prostheses. This thesis presents significant clinical results demonstrating the benefits of such a device on the biomechanics and energetics of people with transtibial amputation while walking. This device has the potential to improve health outcomes in people with transtibial amputation by normalizing biomechanics and increasing energy storage and return, and decreasing contralateral limb loading and unwanted knee external adduction moment. This prosthesis has the potential to expand access to high performance prosthesis technology by creating a device that is low mass, low power, and lower cost compared to fully powered devices.

Thesis Supervisor: Hugh Herr, Professor, Program in Media Arts and Sciences

Acknowledgments

Thank you first and foremost to Professor Hugh Herr. The support, resources, trust, and autonomy that you've given me for pursuing this work was immense, and I am grateful for all I have been able to learn from you during the past 5 years. Thank you also to Professor Amos Winter for your valuable insight into the design of prosthetic devices, and for serving as my committee chair. Thank you to Professor Marty Culpepper for serving as a member of my thesis committee and for your valuable machine design knowledge, I have learned so much from you.

To the Biomechatronics Lab, thanks for being a wonderful group of people to work with. A non-exhaustive list of the Biomech members who have supported me and this work is: Lindsey Reynolds, Seong Ho Yeon, Lucy Du, Christian Landis, Cameron Taylor, Mike Nawrot, Aaron Jaegar, and many more. Thank you especially to Lindsey Reynolds for all of your administrative and logistical support, Seong Ho Yeon for your contributions on the design of the custom embedded system for the VSA prototype, Christian Landis for helping run the clinical study, and Lucy Du for your precision machine design advice.

To Dan and Jasper Rogers-Bradley, thank you for your unconditional love and support. Thank you for keeping our house functional (Dan), reminding me there is more to life than grad school (Jasper & Dan), and taking me on long walks everyday (Jasper).

Thank you to my parents, Rick and Phyllis Rogers, for your endless love and support, and being so proud of me no matter what. Thank you to Heidi, Alice, Lauren, and Dwight for your support and encouragement. Thank you to all my amazing friends who've provided life/PhD advice, support, perspective, and fun times over the past 5 years and beyond. Thank you especially to Melanie, Kriti, Alex, Julia, Bethany, Amy, Jen, and Maile.

Contents

List of Figures

List of Tables

Chapter 1

Thesis Overview

1.1 Thesis Objective

The objective of this thesis is to design and develop a low-mass ankle-foot prosthesis to increase energy return and peak power across walking speeds in order to decrease contralateral limb loading during walking and to decrease potential risk factors for knee osteoarthritis development.

1.2 Specific Aims

The specific aims of this work are as follows:

- Design and develop a low-mass quasi-passive ankle-foot prosthesis with adjustable ankle stiffness through rigorous precision mechanical design and through exploiting biomechanical properties of human gait to allow for optimized stiffness control during walking and standing.
- Validate device performance through mechanical and mechatronic benchtop testing to characterize mechanical properties, verify system behavior, predict reliability, and confirm device safety.
- Evaluate the biomechanical impacts of walking with a stiffness-optimized prosthesis across various speeds on persons with unilateral transtibial amputation

through a clinical study.

1.3 Thesis Contributions

The major contributions of this thesis are summarized below. Details of thesis contributions are presented in Chapters 2-5.

- Developed novel mechanism for adjusting the stiffness of leaf springs [5].
- Designed and evaluated variable stiffness ankle-foot prosthesis to match biological levels of ankle quasi-stiffness during walking [6].
- Designed and conducted clinical study with n=7 study participants with unilateral trans-tibial amputation to evaluate the effects of adjusting device stiffness on biomechanics of walking.
- Demonstrated a statistically significant increase in energy storage, increase in peak power, and decrease in contralateral limb loading and knee external adduction moment across walking speeds in clinical study.

1.4 Thesis Outline

This thesis presents the mechanical and mechatronic design of a novel quasi-passive variable stiffness ankle-foot prosthesis (VSA) for walking speed adaptation. In this thesis I present the device design, benchtop device validation, and human study results. The aim of this research is to evaluate the performance of the VSA prosthesis design and to collect extensive clinical data on the effect of the prosthesis during level ground walking at variable speeds for persons with transtibial amputation. I present results from the clinical study which demonstrate device functionality while walking at variable speeds and demonstrate an improvement in kinematics and kinetics for a person with transtibial amputation walking with the novel prosthesis compared to a standard passive prosthesis. Results from the study demonstrate that this quasi-passive ankle-foot prosthesis increases range of motion, increases energy return, in-

creases peak power, and decreases contralateral knee external adduction moment for people with unilateral transtibial amputation through the use of a robust, low-mass, low-power device. This thesis comprises 5 chapters. Chapter 2 reviews important principles of the biomechanics of human walking, prior art in the field, and the fundamental principles behind the motivation of adjusting prosthesis stiffness during walking. Chapter 3 presents the design, analysis, and benchtop evaluation of the variable stiffness prosthesis. Chapter 4 describes the clinical study design, presents clinical results, and discusses implications of such results. Finally, Chapter 5 discusses future directions and conclusions of this research.

Chapter 2

Introduction and Background

Currently there are an estimated 875,000 people with major lower limb loss in the United States, with numbers projected to increase 1.6-fold by 2050 due to increasing prevalence of diabetes, obesity, and related dysvascular conditions [1]. Lower limb amputation often leads to secondary conditions such as knee pain, knee osteoarthritis, osteopenia, back pain, postural changes, and general deconditioning [2]. Furthermore, it has been shown that energy expenditure during walking increases by 10-55% for people using transtibial prostheses [7]. Altered biomechanics, asymmetry in gait, and poor prosthetic fit contribute to energetic inefficiencies of walking and the aforementioned musculoskeletal pathologies [2]. This chapter outlines existing technological options for lower limb prosthesis users, an overview of the relevant biomechanical functionality and pathology, and motivation for this thesis.

2.1 Prior Art

This section outlines existing ankle-foot prostheses. These prostheses are categorized as powered devices, which use electromechanical transmissions to add positive power to the user's stride; passive devices, which store and return energy passively; and quasi-passive devices, which use electrical energy to change device state or mechanical behavior but do not perform net positive work on the user during walking.

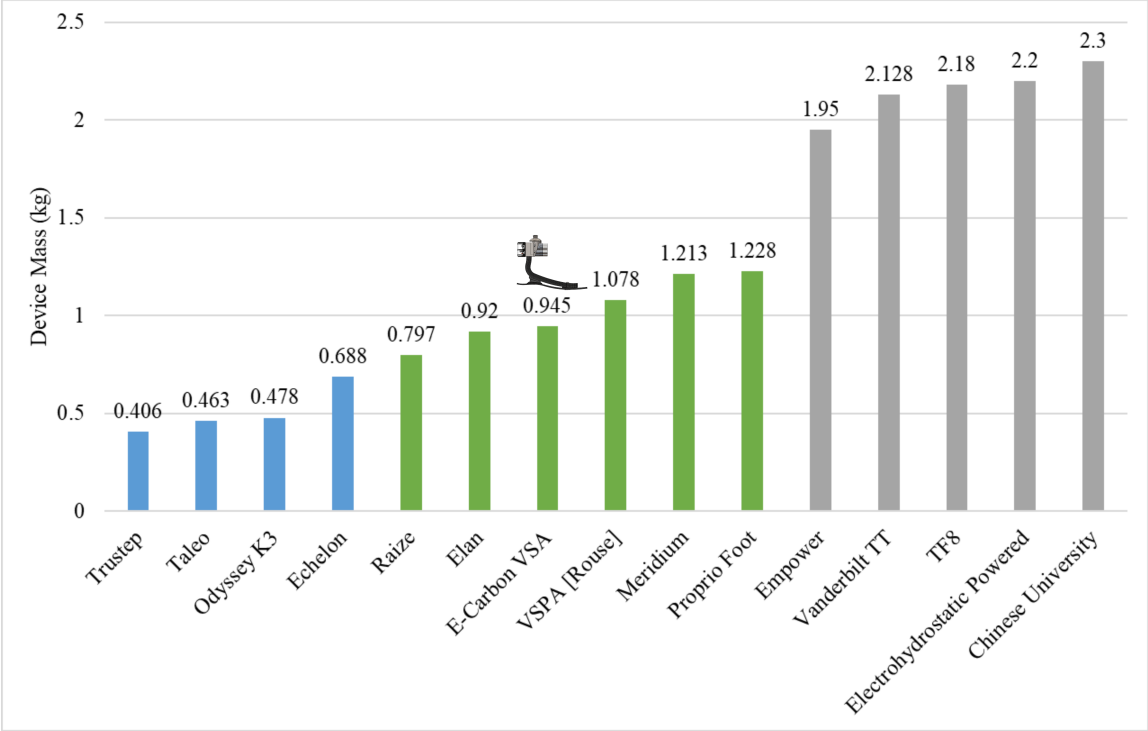

Figure 2-1: **Mass of existing prostheses.** Passive (blue), quasi-passive (green), and powered (grey) prostheses.

2.1.1 Powered Prostheses

Powered prostheses exist that can largely normalize gait during walking, providing physiologic levels of ankle work and power during walking, and decreasing metabolic cost of walking compared to passive devices (Figure 2-3) [12]. Despite the potential advantages of such devices, it is estimated that 5% or less of the population with below-knee amputation use robotic prostheses, primarily due to the high cost and lack of reimbursement by insurance [13, 14]. Powered prostheses are also high in mass, with the only existing common commercial powered ankle prosthesis having a device mass of 1.95 kg (Figure 2-3a) [9]. Figure 2-1 shows the masses of existing prostheses, current powered devices range in mass from 1.95 - 2.3 kg. Mass added distally has a large impact on the metabolic cost of transport; mass added to the foot increases metabolic cost of walking by 12%/kg [15]. Therefore, device mass should be a critical consideration during the design of lower limb prostheses.

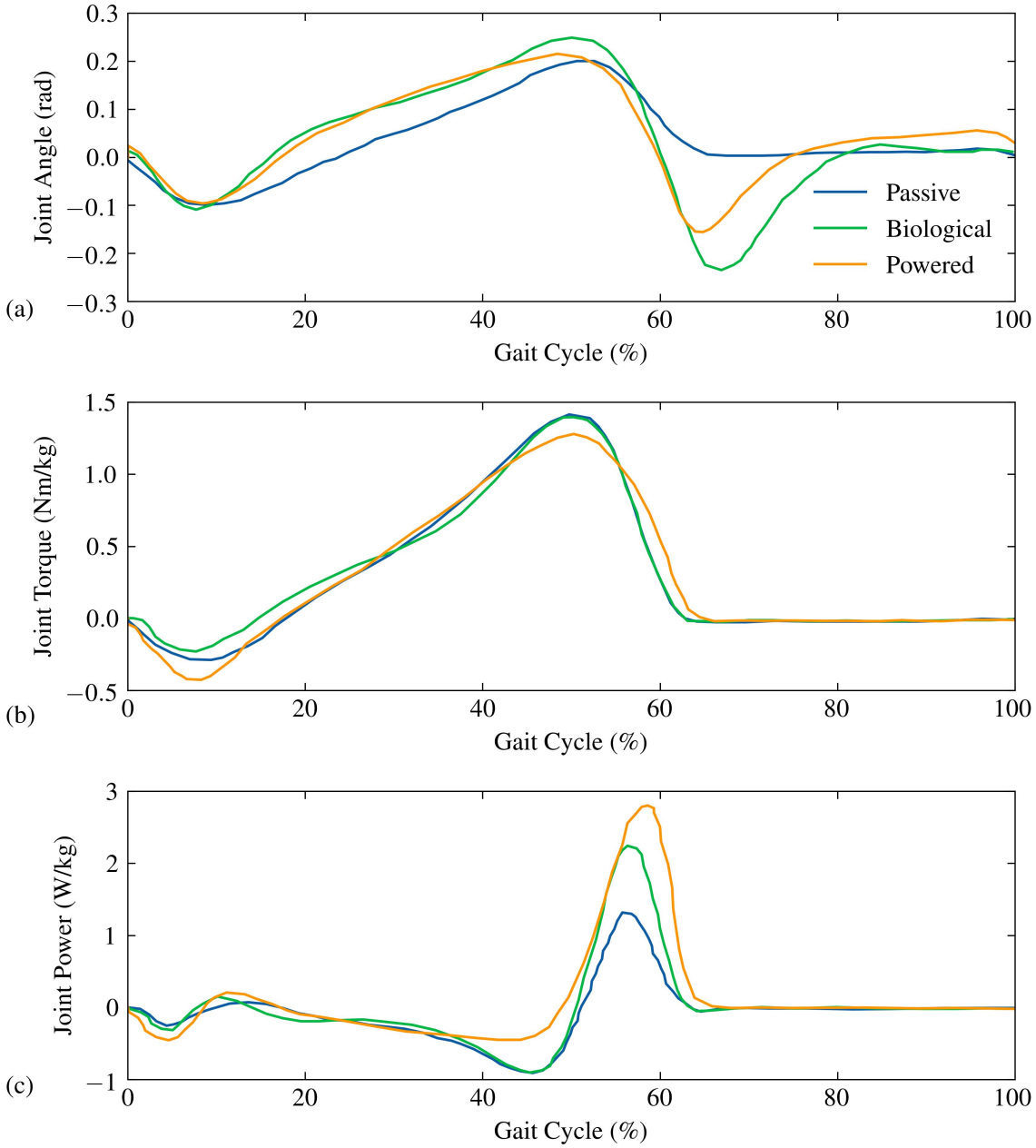

Figure 2-2: **Passive prostheses provide low peak power during walking.** (a) Joint angle, (b) joint torque, and (c) joint power during walking from passive prosthesis, biological limb, and powered prosthesis (data from [8])

.

2.1.2 Passive Prostheses

The majority of people with lower limb amputation in the United States use energy storage and return (ESR) prostheses, which are lower in mass than powered devices

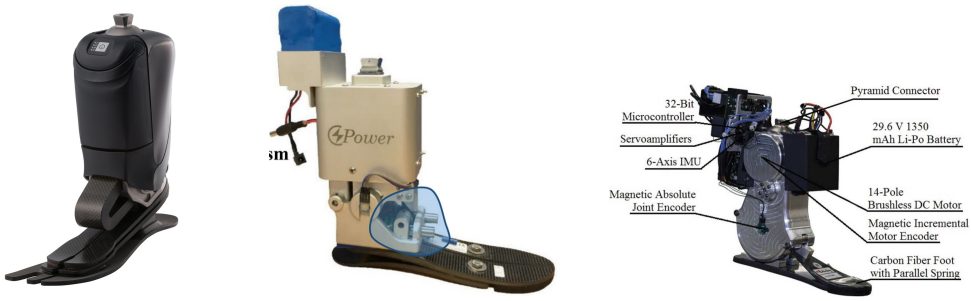

(a) (b) (c)

Figure 2-3: **Powered ankle-foot prostheses.** (a) Ottobock Empower [9], (b) Powered ankle from Chinese University of Hong Kong [10], and (c) Powered ankle from Vanderbilt [11].

(a) (b) (c)

Figure 2-4: **Passive prostheses.** (a) Ottobock Taleo [16], (b) Fillauer AllPro [17], and (c) Ossur Pro-Flex [18].

but provide more limited functionality (Figure 2-4). ESR prostheses act as a spring to store and return energy during gait and have been shown to help normalize biomechanics of those with lower limb amputation [19]. This type of prosthesis is much lower in mass than powered prostheses, ranging in mass from 406 - 688 grams (Figure 2-1). ESR prostheses are able to largely match biological levels of joint angle and torque during stance at a single walking speed (Figure 2-2a and 2-2b). However, these devices provide much lower levels of peak power during walking than the biological ankle or powered prostheses (Figure 2-2c). Additionally, passive prostheses are unable to adapt to changing walking speeds or terrain, and are optimized for performance at a single walking speed. This lack of functionality means that widely used prosthetic

feet are unable to match fundamental behavior of the human ankle-foot complex.

2.1.3 Quasi-Passive Prostheses

(a) (b) (c)

Figure 2-5: **Quasi-passive prostheses.** (a) Ossur Proprio Foot [20], (b) Fillaur Motion Foot SLX [21], and (c) University of Michigan VSPA Foot [22].

Commercial quasi-passive prostheses exist that control joint angle during swing to increase ground clearance (Figure 2-5a) [20], and that use computer controlled hydraulic dampers to adjust joint stability and range of motion during stance to adapt to terrain (Figure 2-5b) [21,23,24]. Quasi-passive research devices include: a variable stiffness foot that varies forefoot bending stiffness though adjustment of the fulcrum point of a beam in bending using a belt drive to change the position of a sliding fulcrum [25], a variable stiffness prosthetic ankle-foot that uses a lead screw driven actuator to change the effective length of a cantilever beam in bending (Figure 2-5c) [22], an energy recycling prosthesis that captures energy from heel strike and returns the additional energy during push-off [26], and a neurally-controlled 2-degree-of-freedom prosthesis which provides position control to the user during swing [27]. Existing quasi-passive devices range in mass from 0.8 - 1.2 kg (Figure 2-1). Quasi-passive devices have the potential to optimize the properties of a prosthesis to adapt to terrain and environment, while keeping device mass, size, power consumption, auditory noise, and cost to a much lower level than fully powered systems, though no device currently exists which successfully optimizes energy storage and peak power across walking speeds. No commercial devices exist that adjust quasi-stiffness of the ankle prosthesis

during walking as the biological ankle does, and existing research devices remain too high in mass and current device architectures do not take advantage of the large energy storage exhibited in passive ESR prostheses.

2.2 Biomechanics Overview

This section summarizes key biomechanical phenomena that are important for understanding the work presented in this thesis, including stiffness modulation of the biological ankle during walking and gait pathologies typically seen in prosthesis users.

2.2.1 Stiffness Modulation of Biological Ankle

One critical property of the biological ankle-foot complex that has demonstrated importance during walking is variable joint compliance [28]. For persons with intact biological ankle-foot complexes, the stiffness of the ankle joint is automatically controlled by the nervous system through contracting and co-contracting the muscles in series with the Achilles tendon to modulate stiffness [29]. The Achilles tendon acts as a large series spring that stores and releases energy during walking [29]. This modulation of series spring stiffness contributes to very efficient power generation and energy storage in the ankle [28, 30]. Furthermore, ankle quasi-stiffness – the torque exhibited over a certain change in joint ankle during a stride or portion of the stride – changes based on walking speed and an individual's body mass and height [31]. Figure 2-6 shows joint angle (a) and moment (b) plotted over gait cycle for slow, medium, and fast walking speeds [32]. Figure 2-7a presents this same data plotted with joint angle on the x-axis and moment on the y-axis - the slope of the dashed lines represent the quasi-stiffness of the biological ankle for each speed, demonstrating the increase in quasi-stiffness of the ankle as walking speed increases [32, 33]. Figure 2-7b presents the stiffness for slow, medium, and fast walking speeds as well as standing [32, 33]. While few variable stiffness prostheses exist, the stiffness of passive ESR prostheses has been shown to impact biomechanics and energetic of walking for people with transtibial amputation. Decreasing prosthesis stiffness increases range of

motion, increases energy storage and return, increases propulsion from the prosthesis, and decreases collision forces on the sound limb [34–36].

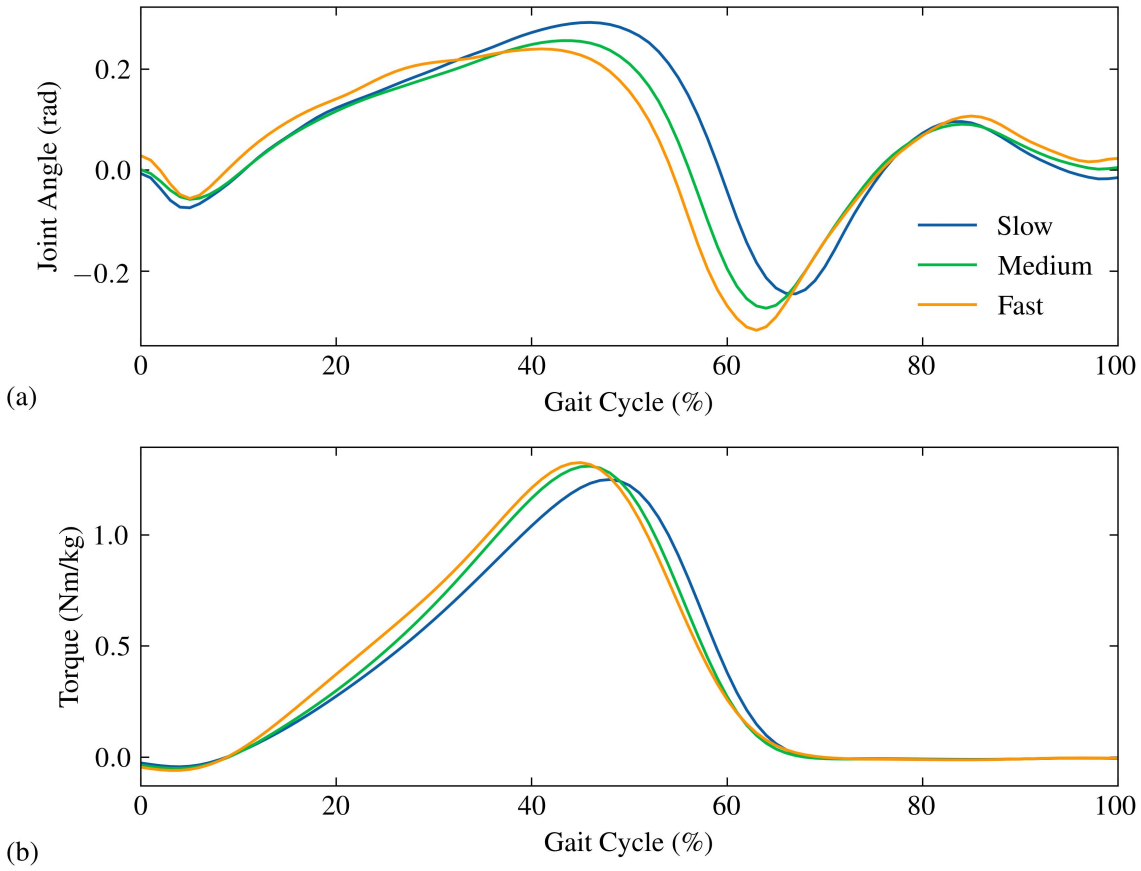

Figure 2-6: **Biomechanics of the ankle during walking.** (a) Joint angle of the biological ankle during walking at various speeds (data from [32]), (b) Joint moment during walking

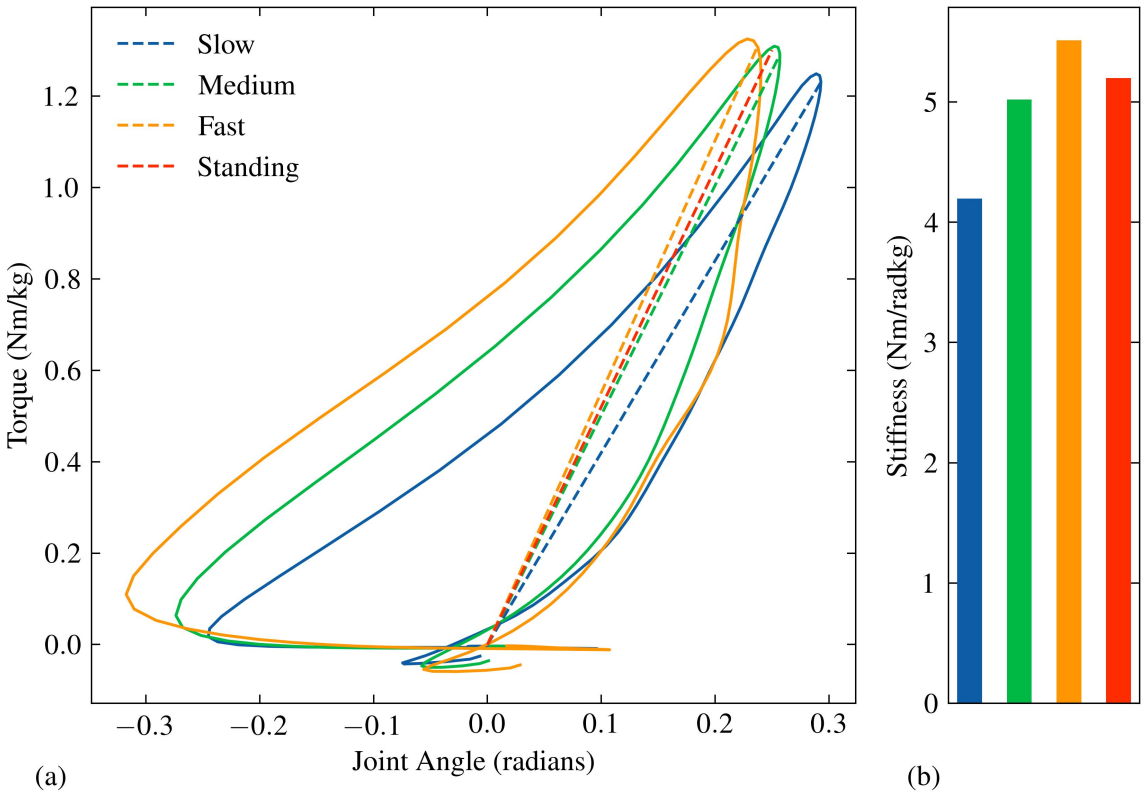

Figure 2-7: **Stiffness of biological ankle during walking.** (a) Torque/angle curve of the biological ankle during walking at various speeds (data from [32,33]), (b) corresponding quasi-stiffness of ankle.

2.2.2 Contralateral Limb Loading Correlated with Knee Osteoarthritis

For people with unilateral transtibial amputation (TTA), prevalence of knee osteoarthritis (OA) in the contralateral limb is up to 17x higher than in the general population, with 27% of people with unilateral TTA developing knee OA [3]. Interestingly, while the prevalence of knee OA and knee pain are significantly more likely in the contralateral limb for people with unilateral TTA, the prevalence of knee pain on the prosthesis side is 20% of the prevalence for the general public [37]. Osteoarthritis is a degenerative joint disease effecting the cartilage in joint, with the knee being the most frequently affected joint [38]. Knee OA most commonly effects the medial compartment of the knee, where loads are the highest during walking [38]. As external adduction moment (EAM) of the knee increases during walking, loads on the

medial compartment of the knee increase [38]. In fact, the magnitude of knee external adduction moment (EAM) during walking has been shown to be a strong predictor of knee OA development [38, 39]. Specifically, the magnitude of the 1st peak of knee EAM is strongly correlated with knee OA [38]. It has been hypothesized that the large increase in contralateral knee OA and decrease in prosthesis side knee pain is due to gait asymmetry, increased loading on the contralateral limb, and decreased loading on the prosthesis side [2, 37]. Specifically, there is an increase in knee EAM in people with unilateral TTA, which is likely associated with the increase in knee pain and knee OA [4, 40]. This increase in contralateral limb loading is hypothesized to be due to decreased push off power from the prosthesis side during step transitions [4]. Figure 2-8a (from [4]) demonstrates that as the leading limb is contacting the ground during heel strike, the trailing limb is pushing off, which works to re-direct the center of mass and decrease the impact of the leading limb. For a prosthesis with insufficient push-off power, such as ESR prostheses, there is insufficient push-off from the trailing (prosthesis side) limb, which increases impact loads on the leading (contralateral) limb, increasing ground reaction forces and knee EAM (Figure 2-8c, d, and e). It has been demonstrated that prostheses which provide higher levels of push-off power can decrease knee EAM and vertical GRF on the contralateral limb, further demonstrating the correlation between prosthesis push-off power and contralateral limb loading [4, 41].

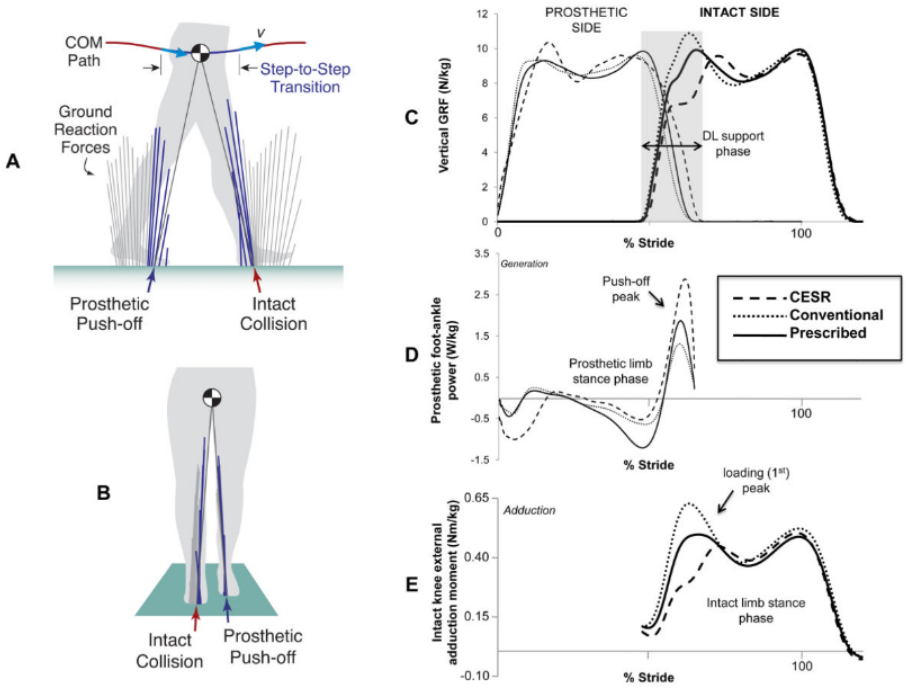

Figure 2-8: **Increased push-off power from prosthesis decreases contralateral limb loading.** (Figure from [4])

2.3 Thesis Aim

The aim of this thesis is to develop a low-mass, quasi-passive ankle-foot prosthesis that increases peak stance power and decreases contralateral limb loading across a range of walking speeds. This thesis aims to develop a prosthesis which provides higher levels of peak power during walking, while keeping device mass and size to a minimum. Specifically, I aim to develop a quasi-passive device which improves walking kinematics and kinetics by varying prosthesis stiffness based on walking speed, restoring an important physiological function of the biological ankle-foot complex. I hypothesize that through optimal tuning of prosthesis ankle joint stiffness during walking to more closely replicate the stiffness of the biological ankle at a given walking speed, gait symmetry will improve, range of motion of the ankle will increase, and peak power and energy return from the prosthesis will increase. I hypothesize that increasing peak power will lead to a decrease in contralateral limb loading and knee EAM, potentially decreasing risk factors for developing knee OA. I hypothesize

that standard ESR prostheses are overly stiff for most walking speeds, and therefore are wasting potential energy storage and return. I hypothesize that by decreasing prosthetic stiffness for a given walking speed to match biological ankle stiffness, we will see an increase in joint angle for a given ground reaction force, and therefor increase energy storage and return and subsequently peak power. In other words, I aim to harness the θ^2 term in energy storage (Equation 2.1) in order to increase energy storage in early stance and increase energy return and therefore peak power, and subsequently decrease unwanted contralateral limb external adduction moment. The approach for increasing energy storage and return through a quasi-passive prosthesis is illustrated in Figure 2-9. For some arbitrary stiffness k_1, we have some angular displacement that occurs for a given torque on the spring, and the energy that is stored by this spring is the integral of torque over angle, which is the blue shaded portion of the plot. If stiffness is decreased to k_2, we see a larger angular displacement for the same torque value, and the energy storage, shown by the green shaded region, is larger. Larger energy storage and return will correspond to greater power. Therefore, by adjusting prosthesis stiffness to biological stiffness levels, I hypothesize that we can increase energy storage and decrease contralateral limb loading. In other words, a passive prosthesis with a fixed stiffness is overly stiff for the majority of walking speeds, and therefore is wasting potential energy storage and return.

$$E = \int \tau d\theta \approx k\theta^2 \tag{2.1}$$

This thesis aims to develop a quasi-passive device which optimizes stiffness in order to decrease detrimental knee EAM on the contralateral limb, improving biomechanics of walking for people with TTA while doing no net positive work. I believe that by developing a device that remains lightweight and low-cost, but has the increased functionality of automatic stiffness control, we can help restore function and decrease risk of disease development for people with lower limb amputations.

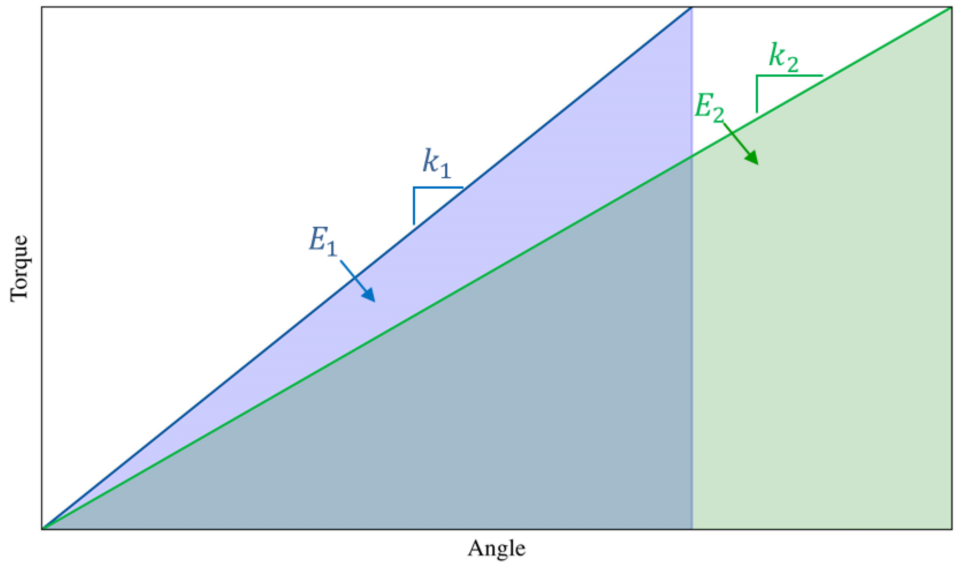

Figure 2-9: **Energy storage in spring.** For a given torque, decreasing spring stiffness leads to an increase in energy storage and return.

Chapter 3

Design and Analysis

This chapter presents the design and evaluation of the novel quasi-passive variable stiffness ankle-foot prosthesis (Fig. 3-1). This chapter first outlines the functional requirements, design specifications, and details of the developed stiffness adjustment mechanism, and then provides details on the the overall device architecture, design calculations and analysis, subsystems design, and system characterization and validation.

3.1 Device Design

This section describes the mechanical and mechatronic design of the variable stiffness prosthesis, linear actuators, and electronics and software design. The prosthesis consists of the following subsystems: composite leaf springs, mechanical housing, linear actuators, and embedded control system and electronics (Fig. 3-2). The prosthesis interfaces with a prosthetic socket via a standard pyramid adapter. The following subsections outline the detailed design and mechanical and structural analysis of the system.

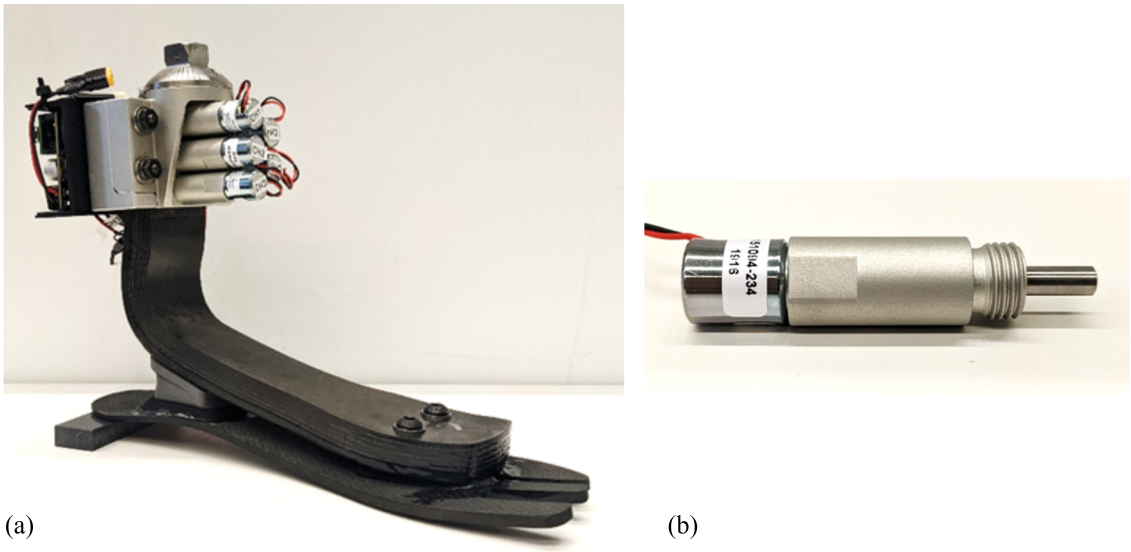

Figure 3-1: **Photos of final variable stiffness ankle-foot prosthesis prototype.** (a) Overall VSA prototype assembly, and (b) custom solenoid driven linear actuators.

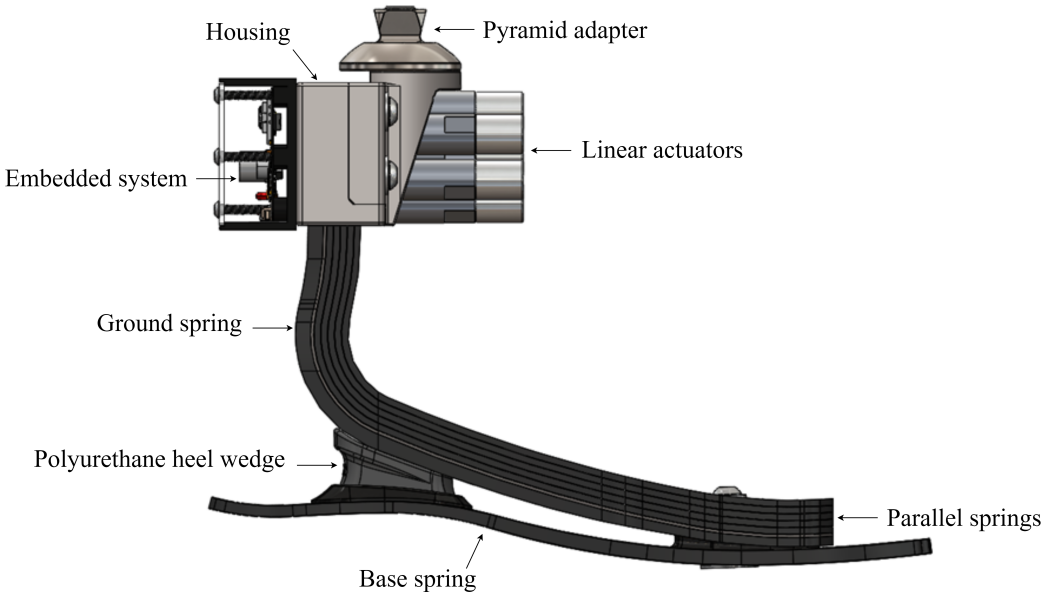

Figure 3-2: **Variable stiffness ankle-foot prosthesis prototype.** Rendering of final VSA prosthesis prototype including composite carbon fiber leaf springs (base spring, ground spring, and parallel springs), solenoid driven linear actuators, actuator housing, and custom embedded system.

3.1.1 Design Specifications

Design specifications were determined based on review of physiological functionality of the ankle-foot complex, anthropometric data, and comparison with existing state-

of-the-art prostheses. The design requirements and achieved values are outlined in Table 3.1. The total device mass including battery and electronics is 945 grams, the build height is 162 mm, and the stiffness range is 352 - 479 Nm/rad. The prosthesis is designed for users with a body mass of up to 88 kg, has a battery life of 11 hours, and is expected to have a cycle life of at least 2.0×10^6 cycles.

Table 3.1: Device specifications

Specification	**Requirement**	**Achieved Value**	**Description**
Mass	$<$ 1000 grams	945 grams	Anthropometric data [42]
Build height	162 mm	162 mm	Anthropometric data [43]
Stiffness range	350 - 475 Nm/rad	352 $\sim$ 479 Nm/rad	Calculated from [32]
Battery life	$>$ 10 hours	10 $\sim$ 11 hours	Standard testing session
Cycle life	$> 2.0 \times 10^6$ cycles	2.0×10^6 steps	ISO Standards [44]

Device mass

The variable stiffness ankle-foot prosthesis is designed based on body mass and height of a 50th percentile male: 78.4 kg and 1.76 m [43]. I estimate the mass of the lower limb that the prosthesis is replacing based on anthropometric data which indicates that the lower leg and foot make up 6.1% of total body mass [42]. Data is lacking on the distribution of residual limb lengths, so I assume the residual limb is 50% the length and mass of the biological lower leg and foot, for a mass of 2.4 kg. Data suggests that prosthetic devices attached to the body via a conventional socket are perceived as an external load, and should therefore have a mass lower than the biological limb which they are replacing [45]. Additionally, mass added distally to the body has large negative consequences on metabolic efficiency of walking [15]. Based on this data I set the target device mass as less than 1000 grams (Table 3.1).

Build height

Design parameters for build height were determined based on similar assumptions to those for the mass specification, outlined above: a 50th percentile male with a height of 1.76 m and a lower limb length of 0.50 m [43]. Assuming the residual limb is 50% the

length of the biological lower leg and foot the maximum device build height would be 250 mm. However, in order to allow for the necessary height for the prosthetic socket and pyramid adapters, the maximum build height should be 200 mm. Additionally, in order to facilitate comparison between the developed device and a passive control, I aim to match the build height of the passive ESR prosthesis (Taleo 27-5 or 27-6, Ottobock, Duderstadt, Germany) which will be used as a control, for a build height of 162 mm (Table 3.1) [16].

Stiffness range

The desired stiffness range of the device was specified based on matching biological ankle joint stiffness of a 50th percentile male for a range of walking speeds from a slow walk to a fast walk: 0.75 m/s - 1.5 m/s. I used joint torque and joint angle data from [32] to calculate ankle joint quasi-stiffness for each speed as the slope of line from heel strike to mid stance (Table 3.1), where the ankle dorsiflexion ankle is at a maximum.

Battery life

The battery life of the prototype should be sufficient for a typical day of walking, or about 10-12 hours. Expected battery life was calculated based on the energy consumption of the actuators, sensors, and embedded system, and the assumption that the actuators will be utilized 50% of the time during a typical use session (Table 3.1).

3.1.2 Stiffness-Change Mechanism

The variable stiffness prosthesis utilizes a novel stiffness changing mechanism in which computer-controlled solenoid-driven micro linear actuators lock relative sliding between parallel composite leaf-springs, increasing the bending stiffness. Each parallel leaf spring is independently controlled, and locking non-adjacent springs to a mechanical ground increases the number of possible stiffness settings. The parallel axis

theorem explains that the moment of inertia increases as the bending axis is moved farther from the centroid, as shown in Equation 3.1, where I_c is the centroidal moment of inertia, A is the cross-sectional area, and d is the distance between the centroidal axis and the bending axis. As each leaf spring is locked to the mechanical ground, springs farther from the bending axis have a greater moment of inertia and therefore greater bending stiffness. For example, locking spring 1 to ground is stiffer than locking spring 5 to ground, due to increasing d. Therefore, each distinct combination of locked and unlocked springs has a different bending stiffness, such that the total number of stiffness configurations for the device with 1 ground spring and 5 parallel springs is equal to 32, as shown in Equation 3.2.

$$I_{parallel} = I_c + Ad^2 \tag{3.1}$$

$$n_{combinations} = \sum_{n=0}^{5} C(5, i) = 32 \tag{3.2}$$

This novel stiffness-change mechanism enables the design of the variable stiffness ankle-foot prosthesis with several key functionalities that distinguish it from existing devices. The locking mechanism architecture allows for rapid state changes between stiffnesses, and the time of state transitions is constant regardless of the magnitude of stiffness increase. Changing device stiffness from the lowest to the highest stiffness setting occurs in the same time as changing device stiffness to the next closest setting. This allows for rapid state changes during the swing phase of walking, with a state transition time of approximately 20 ms. The binary state of the solenoid driven actuators allows for robust control of device properties in a simple actuator package.

3.1.3 Parametric Model

A parametric model was developed in order to approximate the stiffness of the device for a given spring geometry, as well as the expected stiffness increase when each spring is locked. The spring assembly is modeled as a ground spring, and 5 parallel lockable leaf springs. In the lowest stiffness configuration (Fig. 3-3a), when all locking

actuators are unlocked, the total device stiffness is approximated by the stiffness of the ground spring in parallel with the 5 lockable springs as in Equation 3.3. In the highest stiffness configuration (Fig. 3-3b), the total device stiffness is represented as the ground spring, 5 lockable springs, and 5 actuators in parallel as in Equation 3.4 .

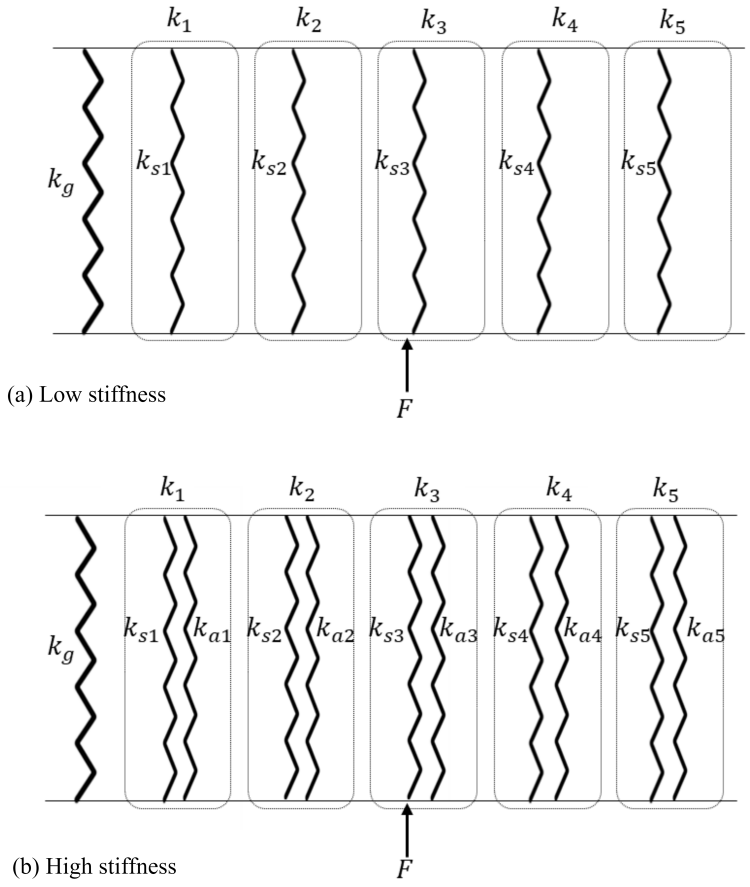

Figure 3-3: **Stiffness model.** (a) Lowest stiffness configuration is modeled as the ground spring in parallel with 5 locking springs, (b) highest stiffness state is modeled as the ground spring in parallel with 5 locking springs and 5 locking actuators.

$$k_{unlocked} = k_{ground} + k_{s1} + k_{s2} + k_{s3} + k_{s4} + k_{s5} \tag{3.3}$$

$$k_{locked} = k_{ground} + \sum_{n=1}^{5} k_{s(n)} + \sum_{n=1}^{5} \delta_{ratio} k_{actuator} \tag{3.4}$$

$$\delta_{ratio} = \frac{\delta_{proximal}}{\delta_{distal}} = \frac{\frac{\theta_{deflection}}{2\pi}(r_o - r_i)2\pi}{\delta_{distal}} = \frac{sin^{-1}(\frac{\delta_{distal}}{l_2})(r_o - r_i)}{\delta_{distal}} \tag{3.5}$$

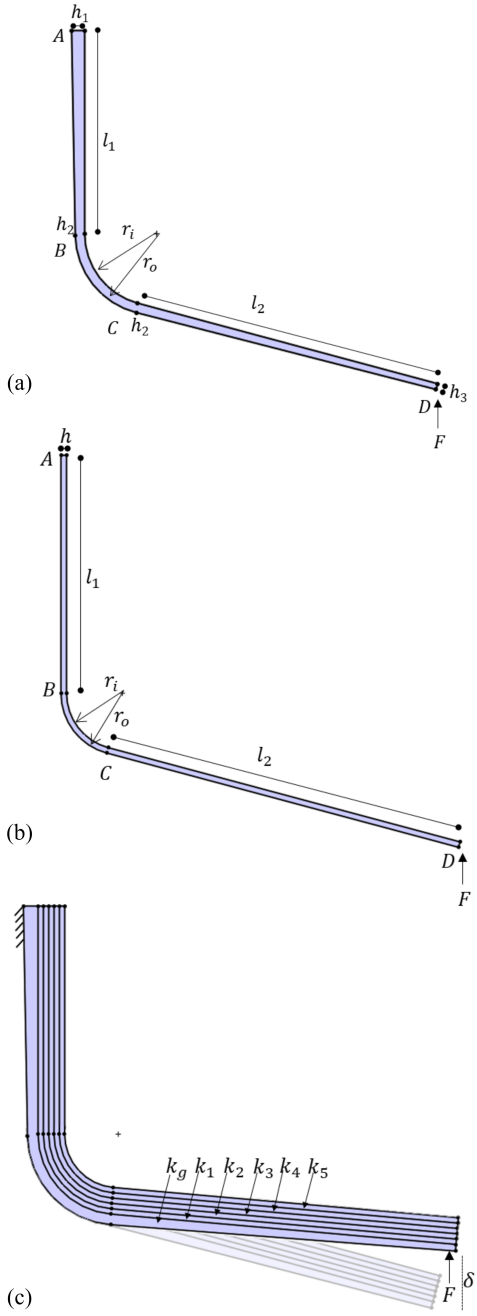

Figure 3-4: **Parametric model of spring stiffness.** (a) Simplified model of base spring geometry showing variables of interest, leaf springs are modeled as straight cantilever beam section AB, curved section BC, and straight cantilever beam section CD (b) parallel spring geometry, (c) total spring assembly.

In Equations 3.3 and 3.4, k_{ground} is the stiffness of the ground spring, k_{s1}, k_{s2}, k_{s3}, k_{s4}, and k_{s5} are the stiffnesses of the five lockable springs, $k_{actuator}$ is the actuator

stiffness, and δ_{ratio} is the deflection ratio between the distal (δ_{distal}) and proximal ($\delta_{proximal}$) ends of the springs, which is determined by the geometry of the springs due to the change in circumference on the inner and outer radius of the spring as it deflects. Equation 3.5 calculates δ_{ratio}, where $\theta_{deflection}$ is the angular deflection of the distal end of the spring, r_o is the outer radius of the spring, r_i is the inner radius, and l_2 is the length of the distal segment of the spring.

Leaf spring stiffness model

The stiffness of the leaf springs is calculated using Castigliano's Theorem, by taking the partial derivative of the strain energy with respect to force to calculate deflection (Equation. 3.6) [46]. The geometry of the leaf springs is simplified as a straight cantilever beam section in series with a curved section (Fig. 3-4a and Fig. 3-4b). For the straight portion of the springs the deflection of the spring under load F is calculated in Equation 3.7, where E is the bulk elastic modulus of the composite material, I is the moment of inertia, M is the bending moment, and A is the cross-sectional area. Bending moment of inertia, I, and cross-sectional area, A, of the ground spring vary along length l, as the spring is tapered.

$$\delta = \frac{\partial U}{\partial F_i} \tag{3.6}$$

$$\delta_{ab} = \int_0^{l_1} \frac{1}{EI}\left(M\frac{\partial M}{\partial F}\right)dx + \int_0^{l_1} \frac{1}{AE}\left(F\frac{\partial F}{\partial F}\right)dx \tag{3.7}$$

$$\delta_{ab} = \frac{1}{2EI}F(l_2+R)l_1^2 + \frac{Fl_1}{AE} \tag{3.8}$$

$$\delta_{cd} = \int_0^{l_2} \frac{1}{EI}\left(M\frac{\partial M}{\partial F}\right)dx + \int_0^{l_2} \frac{1}{AE}\left(F\frac{\partial F}{\partial F}\right)dx \tag{3.9}$$

$$\delta_{cd} = \frac{Fl_2^3}{3EI} \tag{3.10}$$

I calculate deflection of curved section as the partial derivative of the strain energy in terms of force, F, integrated over θ from 0 to $\pi/4$ (Equation 3.11 and Equation 3.12), where M is bending moment, E is modulus of elasticity, and e is eccentricity. The geometric parameters are shown in Fig. 3-4 for the ground spring (Fig. 3-4a) and the parallel springs (Fig. 3-4b).

$$\delta_{bc} = \int_0^{\pi/2} \frac{M}{AeE}\left(\frac{\partial M}{\partial F}\right) d\theta + \int_0^{\pi/2} \frac{F_\theta R}{AE}\left(\frac{\partial F_\theta}{\partial F}\right) d\theta - \int_0^{\pi/2} \frac{1}{AE}\frac{\partial (MF_\theta)}{\partial F} d\theta + \int_0^{\pi/2} \frac{CF_r R}{AG}\left(\frac{\partial F_r}{\partial F}\right) d\theta \quad (3.11)$$

$$\delta_{bc} = \int_0^{\pi/2} \frac{1}{AeE}\left(F(Rsin\theta + l_2)^2\right) d\theta + \int_0^{\pi/2} \frac{R}{AE}\left(F_\theta sin\theta^2\right) d\theta - \int_0^{\pi/2} \frac{1}{AE}\left(2FRsin\theta^2\right) d\theta + \int_0^{\pi/2} \frac{CF_r Rcos\theta}{AG} cos\theta d\theta \quad (3.12)$$

The total deflection for each spring is shown in Equation 3.13, and spring stiffness is calculated in Equation 3.14.

$$\delta_{total} = \delta_{ab} + \delta_{bc} + \delta_{cd} \quad (3.13)$$

$$k_s = \frac{F}{\delta_{total}} \quad (3.14)$$

Actuator stiffness

In order to determine the stiffness of the device when the actuators are locked, I calculate the stiffness of the actuator assembly. I calculate the stiffness of the actuator assembly by determining the axial displacement at the pin slot interface on the leaf spring for a given load, accounting for deflection of the bearing (Equation

Table 3.2: Spring stiffness parametric model variables and values

Parameter	**Value**	**Description**
E	70 GPa	Elastic modulus carbon fiber composite
G	5 GPa	Shear modulus carbon fiber composite
C	1.2	rectangular cross-section correction factor
L_1	0.08 m	Length of segment AB of springs
L_2	0.12 m	Length of segment CD of springs
R	0.019 m	Radius of curvature
r_o	0.01986 m	Outer radius
r_i	0.01814 m	Inner radius
b	40.0×10^{-3}	width leaf springs
h	1.742×10^{-3} m	thickness lockable springs
h_1	5.0×10^{-3} m	thickness ground spring h_1
h_2	4.0×10^{-3} m	thickness ground spring h_2
h_3	3.0×10^{-3} m	thickness ground spring h_3
e	7.3×10^{-4}	eccentricity $e = R - \frac{h}{ln(\frac{r_o}{r_i})}$
δ_{ratio}	0.0145	$\frac{\delta_{proximal}}{\delta_{distal}}$ deflection ratio of leaf spring
k_s	$1.22 \times 10^3 N/m$	Stiffness parallel springs
k_g	$2.56 \times 10^4 N/m$	Stiffness ground spring
$k_{actuator}$	$1.64 \times 10^5 N/m$	Actuator stiffness

3.15 and Equation 3.16), the shaft (Equation 3.17 and Equation 3.18), axial compression of the leaf spring (Equation 3.19), and the axial clearance in the slot interface (Equation 3.20). The total displacement at the actuator/slot interface due to these displacements is calculated using homogeneous transformation matrices. The parametric model was implemented in MATLAB (MATLAB R2021a, MathWorks, Natick, MA, USA). See Appendix C for details and full model code.

$$\delta_{ybearing} = \frac{F}{k_{bearing}} \tag{3.15}$$

$$\delta_{\theta zbearing} = \frac{F(l_{shaft} + l_{bearing/2})}{\frac{F(l_{bearing}/2)}{sin^{-1}(\frac{F/k_{bearing}}{l_{bearing}/2})}} \tag{3.16}$$

$$\delta_{yshaft} = \frac{Fl_{shaft}^3}{3EI} \tag{3.17}$$

$$\delta_{\theta zshaft} = \frac{F l_{shaft}^2}{2EI} \tag{3.18}$$

$$\delta_{axial} = \frac{F l_{spring}}{A E_{cf}} \tag{3.19}$$

$$\delta_{slot} = \frac{F}{k_{slot}} \tag{3.20}$$

Scaling parametric model

Spring stiffness In order to increase the stiffness of the prosthesis, there are several design variables that may be adjusted. Increasing the thickness of the ground spring or the parallel springs will increase the overall stiffness of the prosthesis, and scales with h^3.

Stiffness range In order to change the stiffness range that is achievable with the variable stiffness prosthesis, there are several design variables that may be adjusted. The possible range of stiffness control can be adjusted by (1) decreasing the clearance at the pin/slot interface, (2) increasing actuator stiffness, or (3) decreasing stiffness of the leaf springs will lead to a larger increase in stiffness range between the lowest and highest stiffness configuration.

Resolution In order to adjust the resolution of stiffness control, I can adjust the number of lockable leaf springs. Adding additional lockable leaf springs with corresponding locking actuators will allow for a greater number of independent stiffness states and higher resolution stiffness control. Equation 3.21 demonstrates the number of independent stiffness configurations which exist for a given number of lockable springs/actuator pairs.

$$n_{combinations} = \sum_{n=0}^{m} C(m, i) \tag{3.21}$$

3.1.4 Leaf Spring Design

The leaf spring subsystem consists of a ground spring, base spring, and 5 parallel leaf springs. Parallel leaf springs are 1.742 mm thick (13 plies), and the ground spring is tapered with a thickness of 4.96 mm (37 plies) at the proximal end and 2.95 mm (22 plies) at the distal end. The custom leaf springs were fabricated (Ottobock Manufacturing, Ottobock, Salt Lake City, UT, USA) using unidirectional carbon fiber sheets with a ply thickness of 0.134 mm. Between each parallel spring a layer of PTFE with a thickness of 0.127 mm is co-cured to the springs to decrease the coefficient of friction between the sliding surfaces.

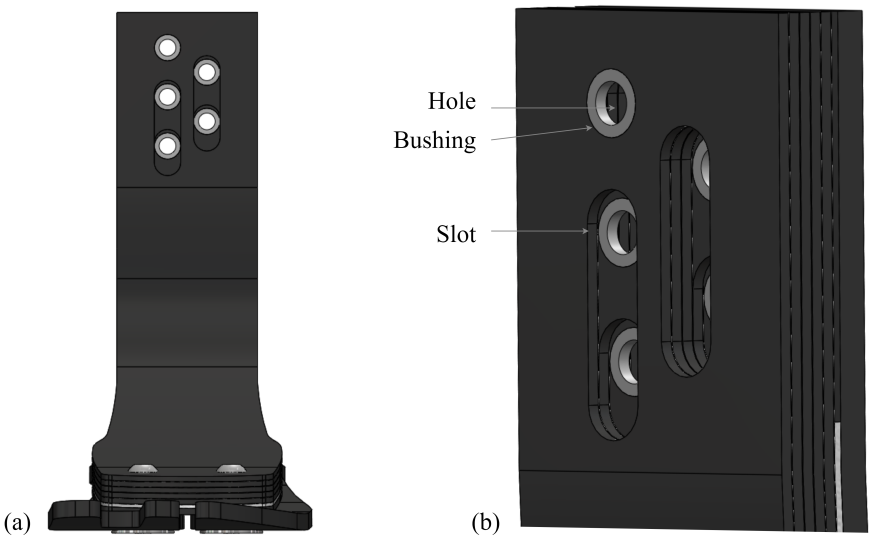

Figure 3-5: **Leaf spring design.** (a) Carbon fiber composite leaf spring assembly consists of a ground spring and 5 parallel lockable springs. (b) Close up of slot/hole configuration. A pin driven by each locking actuator engages with the hole in the corresponding leaf spring.

Finite element modeling of leaf springs

I modeled stiffness and structural properties of the composite leaf springs in Ansys Composite PrepPost (ACP, Ansys, Inc., Canonsburg, PA, USA) finite element analysis (FEA) software. I built an FEA model representing the ply geometry and fiber orientation of the leaf springs. Bonded contacts are used at the toe to simulate the

epoxy and bolted joint, and between the ground spring and the housing. Frictional contacts are used at the sliding surface of each spring, with a coefficient of friction of 0.10. The model is set to large deflection mode, weak springs is turned off, and 100 steps are used. The housing is a fixed support and a ramped vertical load of 700 N is applied to the toe of the prosthesis to replicate the benchtop test conducted during device validation.

Stress in carbon fiber springs

I performed stress analysis to estimate the maximum expected stress in the carbon fiber leaf springs. The maximum expected stress in the carbon fiber springs was calculated as 480 MPa as an upper bound using standard beam bending equations and approximating the spring as a cantilever beams shown in Equation 3.22, where M is the bending moment, c is the maximum distance from the centroidal axis, and I is bending moment of inertia. The Ansys FEA model predicts a maximum stress of 350 MPa. Assuming an ultimate stress of unidirectional 0° carbon fiber (σ_{ult}) of 1500 MPa [47], the safety factor to failure is 5. I performed fatigue analysis to ensure the carbon fiber will likely withstand cyclic loading of up to 2 million cycles at our expected load, in order to meet the ISO standards for cycle life [44]. Experimental data from the literature indicates a fatigue limit of 700 MPa for unidirectional 0° carbon fiber at 10^7 cycles [48, 49]. This gives us a factor of safety (FOS) of 2 at our max expected loading, indicating that based on these preliminary conservative calculations a fatigue failure of the carbon fiber springs is unlikely.

$$\sigma_{max} = \frac{Mc}{I} \approx \frac{(80Nm)(.0025m)}{\frac{(0.04m)(0.005^3m)}{12}} \approx 480MPa \tag{3.22}$$

Contact stress at spring interface

I modeled the contact loading at the interface between the parallel springs (Fig. 3-6) based on contact mechanics of normal loading and frictional sliding. This loading can be described as a normal force pressing the springs together combined with a frictional force due to the relative sliding between the springs. As the thin PTFE

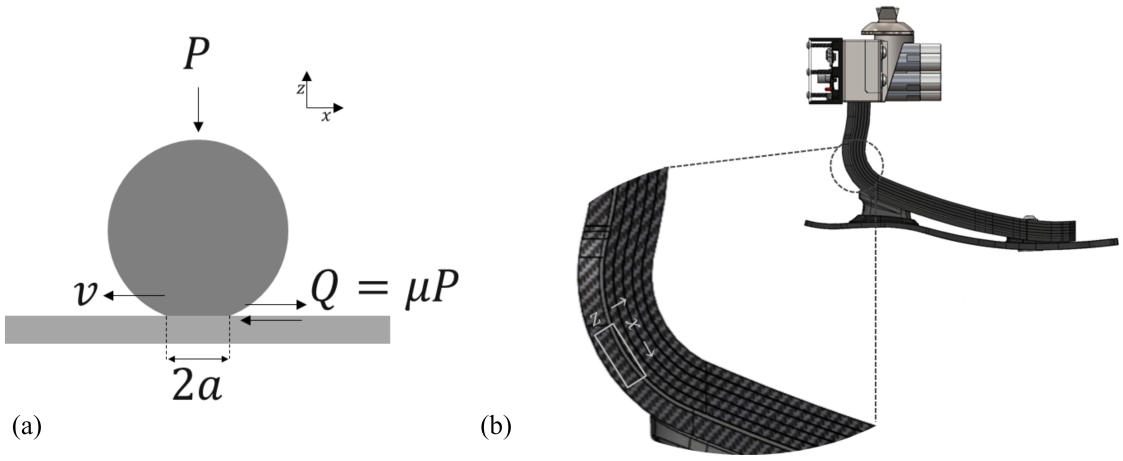

Figure 3-6: **Contact stress at spring interface.** Contact stress at leaf spring interface is calculated using Hertzian contact theory, (a) the contact area between the springs is modeled as a cylinder in contact with a flat plate, (b) the maximum contact stress occurs at the inner radius of the ground spring.

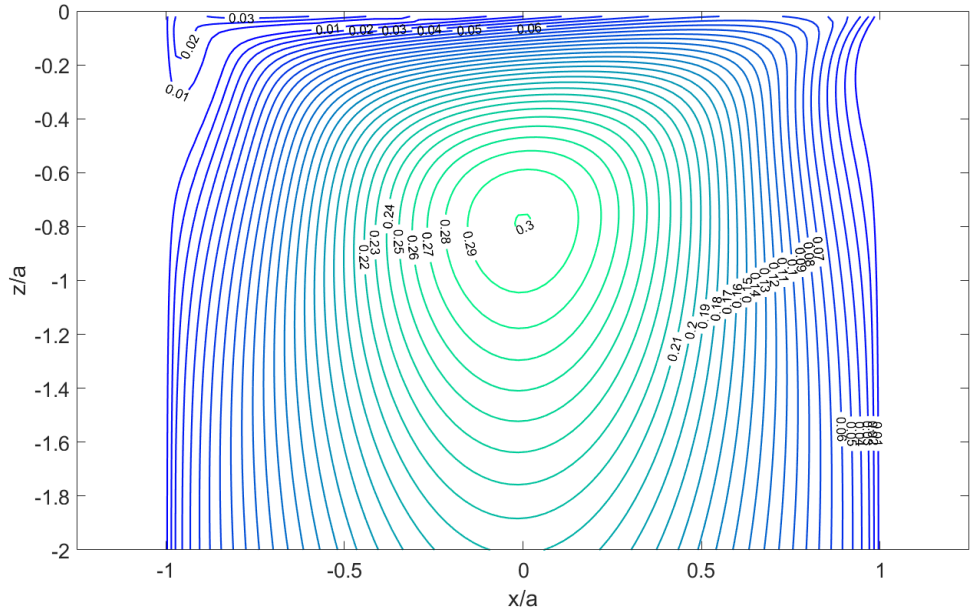

Figure 3-7: **Subsurface shear stress at spring interface.** Subsurface shear stress plotted relative to contact area half-width, a, and subsurface depth as a ratio of contact area half-width, z/a. The maximum subsurface shear stress occurs at a depth of -0.79a.

film is less than 5 times the half-width of the contact area, the stiffness of the contact area is not affected by the thin film and can be treated as two equal stiffness carbon fiber components in contact [50]. Because the coefficient of friction is much less than

1, the effect of frictional force on contact area is very small and can be neglected. I therefore assume that the normal pressure and tangential traction are independent and may be superposed [51]. I assume Amontons' law of sliding friction, and the tangential traction can be defined by Equation 3.24 [51], where P is the load per unit length at the contact area (Equation 3.23) and μ is the coefficient of friction.

$$P = \frac{F}{l} \tag{3.23}$$

$$Q = \mp \mu P \tag{3.24}$$

The spring interface is approximated as a cylinder on a flat plate (Fig. 3-6a). Because the contact area half-width is $< 10\times$ the contact radius, the contact stress is calculated based on Hertzian contact mechanics [52]. The contact area half width, a, is calculated in Equation 3.25. The equivalent radius of curvature, r_c is defined in Equation 3.26, where r_1 is the radius of the internal leaf spring (convex) and r_2 is the radius of the external leaf spring (concave). The equivalent elastic modulus, E_c, is defined in Equation 3.27, where in this case E_1 is equal to E_2, which is the bulk elastic modulus of carbon fiber composite, and v_1 is equal to v_2, which is the Poisson's ratio of carbon fiber composite.

$$a = \sqrt{\frac{4Pr_c}{\pi E_c}} = 0.0017m \tag{3.25}$$

$$r_c = \left(\frac{1}{r_1} + \frac{1}{r_2}\right)^{-1} = 4.02m \tag{3.26}$$

$$E_c = \left(\frac{1 - v_1^2}{E_1} + \frac{1 - v_2^2}{E_2}\right)^{-1} = 5.49 \tag{3.27}$$

The contact pressure for a given location x is defined as Equation 3.28, where P is the normal force per unit length at the line contact. The tangential traction for a given location x along the cylinder is shown by q in Equation 3.29

$$p(x) = \frac{2P}{\pi a^2}\sqrt{a^2 - x^2} \tag{3.28}$$

$$q(x) = \mp\frac{2\mu P}{\pi a^2}\sqrt{a^2 - x^2} \tag{3.29}$$

The maximum contact pressure occurs in the center of the contact at x=0, as defined by Equation 3.30.

$$p_{max} = \frac{2P}{\pi a} = 1.19MPa \tag{3.30}$$

The stress due to a combination of frictional traction and pressure is given in Equation 3.31 - Equation 3.34.

$$\sigma_x = -p_{max}\{(1 - \frac{x^2}{a^2})^{1/2} + \frac{2\mu x}{a}\} \tag{3.31}$$

$$\sigma_z = -p_{max}(1 - \frac{x^2}{a^2})^{1/2} \tag{3.32}$$

$$\sigma_y = -2vp_{max}\{(1 - \frac{x^2}{a^2})^{1/2} + \frac{\mu x}{a}\} \tag{3.33}$$

$$\tau_{xz} = -\mu p_{max}(1 - \frac{x^2}{a^2})^{1/2} \tag{3.34}$$

$$\tau_1 = \frac{1}{2}\{(\sigma_x - \sigma_y)^2 + 4\tau_{xz}^2\}^{\frac{1}{2}} \tag{3.35}$$

$$\tau_{max} = 0.3p_{max} = 0.36MPa \tag{3.36}$$

The maximum contact stress at the spring interface is estimated to be 1.19 MPa (Equation 3.30), for a safety factor of 38x above the yield stress of the epoxy in the composite ($\sigma_{yieldepoxy}$). This analysis demonstrates that the bending stress dominates in the carbon fiber and epoxy degradation due to contact stress is not a concern. Fig.

3-7 shows the subsurface principle shear stress, τ_1 (Equation 3.35). The maximum subsurface shear stress, τ_{max} (Equation 3.36), occurs at a depth of -.79a, which is beneath the thin film PTFE layer.

Table 3.3: Variables and values for leaf spring contact stress calculations

Parameter	**Value**	**Description**
a	0.0017 m	Contact area half-width
F	130 N	Load
l	0.04 m	Contact area length
P	3.24 $\frac{kN}{m}$	Load per unit length
Q	324 $\frac{N}{m}$	Frictional force per unit length
μ	0.10	Coefficient of friction
r_c	4.02 m	Equivalent contact radius
r_1	0.02 m	Radius of internal leaf spring (convex > 0)
r_2	-0.0201 m	Radius of external leaf spring (concave < 0)
E_c	5.5 GPa	Equivalent elastic modulus contact area
E_1	10 GPa	Elastic Modulus UD carbon fiber composite 90° [47]
E_2	10 GPa	Elastic Modulus UD carbon fiber composite 90° [47]
v_1	0.30	Poisson's Ratio UD carbon fiber composite [47]
v_2	0.30	Poisson's Ratio UD carbon fiber composite [47]
p_{max}	1.19 MPa	Maximum contact stress
τ_{max}	0.36 MPa	Maximum subsurface shear sress
$\sigma_{yieldepoxy}$	52 MPa	Yield stress epoxy [53]

Interspring wear at PTFE interface

I calculated the expected sliding wear rate of the PTFE film at the sliding contact area between the leaf springs. The wear depth per operating cycle is calculated in Equation 3.37, where W is the wear rate of PTFE (mm^3/Nm) [54], l is the sliding distance per cycle (m), and p is the contact pressure at the interface (MPa).

$$t_{wear} = Wlp \tag{3.37}$$

$$t_{wear} = W \int_0^l p(x)dx \tag{3.38}$$

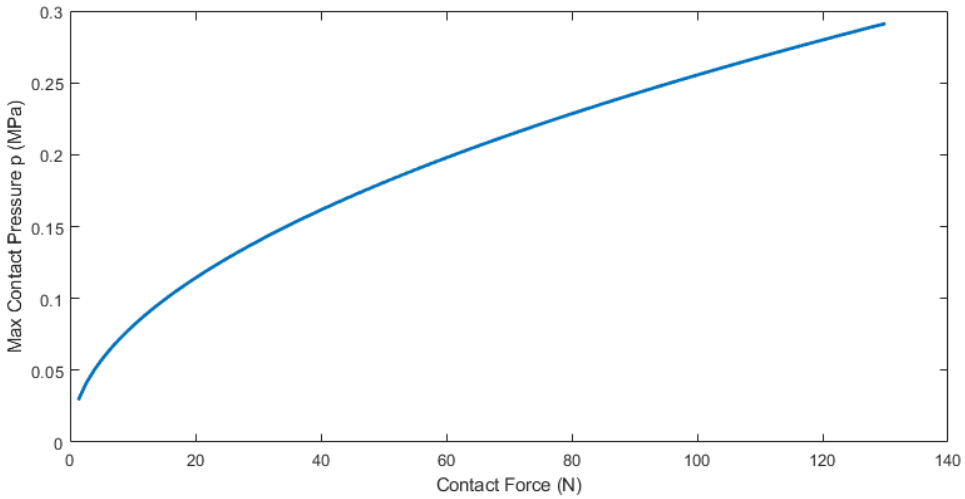

Figure 3-8: **Contact pressure at sliding interface.** Maximum contact pressure at PTFE coated spring interface.

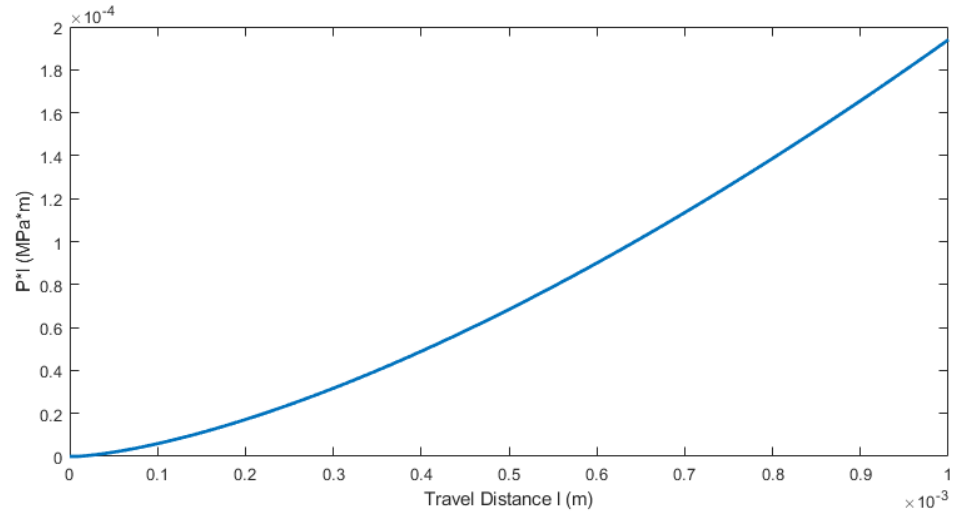

Figure 3-9: **Contact pressure $\times$ travel distance.** Maximum contact pressure integrated over travel distance $\int_0^l P(x)dx$

The worst-case wear scenario is calculated assuming a contact area equal to the Hertzian line contact. The contact stress is calculated as in in the previous section, replacing the material properties of PTFE (Table 3.4) in Equation 3.27 and Equation 3.25. Fig. 3-8 shows the maximum contact stress at the PTFE interface for a given load. As the contact pressure is not at a maximum during the entire linear sliding distance, we must take the integral of the contact pressure as a function of sliding

distance over distance from 0 to l, as in Equation 3.38. Fig. 3-9 shows how pl increases as travel distance increases. For this worst-case wear scenario of line contact, the wear thickness per cycle is 6.78×10^{-8} mm, and the expected cycle life, n, is 1.9×10^{6} cycles. A more realistic scenario is an increasing contact area as wear occurs, so in reality we expect a lifetime longer than 1.9×10^{6} cycles.

Table 3.4: Variables and values for PTFE wear rate calculations

Parameter	**Value**	**Description**
W	$35 \times 10^{-5} \frac{mm^3}{Nm}$	Wear rate PTFE [54]
t_{PTFE}	0.127 mm	Thickness PTFE thin film
l	0.001 m	Maximum length of travel
E_{PTFE}	0.60 GPa	Elastic modulus PTFE [54]
p_{max}	0.29 MPa	Maximum contact pressure
t_{wear}	6.79×10^{-8} mm	Wear thickness per cycle
n	1.9×10^{6} cycles	Cycle life PTFE

3.1.5 Actuator Design

The linear actuators are driven by a solenoid (STA-50M-STA 151094-234, Johnson Electric, Hong Kong, China) which drives an attached shaft to an extended or contracted state. The solenoid-driven architecture allows for rapid changing between binary spring states (locked or unlocked). The pins engage with a slot on each parallel spring, when the pin is engaged is prevents the corresponding spring from sliding relative to the base spring, increasing the bending stiffness.

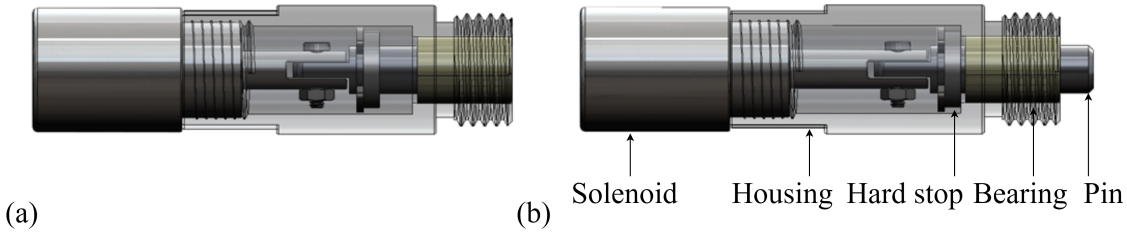

Figure 3-10: **Actuator design.** Rendering of final actuator design, (a) shows actuator in unlocked state, (b) shows actuator in locked state and highlights the solenoid, actuator housing, hard stop, bearing, and pin.

Solenoid selection

The linear actuators are driven by a solenoid (STA-50M-STA 151094-234, Johnson Electric, Hong Kong, China). The solenoid has a nonlinear output force of at least 2N, a stroke length of 2.5 mm, and a no-load speed of 6 ms/2.5 mm. These solenoids, with a minimum operating voltage of 6 V, draw electrical current lower than 1 A during transient transitions. The transient actuation of the actuators occurs within a duration of less than 30 ms for bi-linear state transition. The solenoid was selected based on the expected force required to actuate the pin at our desired acceleration while overs=coming the holding force of the solenoid spring.

$$F = \eta(ma + F_{spring}) = \eta(m_{pin} + m_{solenoidshaft}) \tag{3.39}$$

Bearing selection

Table 3.5: Variables and values for contact stress calculations at bearing interface

Parameter	**Value**	**Description**
v_1	0.29	Poisson's ratio pin [55]
v_2	0.40	Poisson's ratios bearing [56]
E_1	205 GPa	Elastic modulus pin [55]
E_2	2.5 GPa	Elastic modulus bearing [57]
E_c	2.9 GPa	Equivalent Elastic modulus
r_1	2.50 mm	Radius pin
r_2	-2.534 mm	Radius bearing
r_c	0.186 m	Equivalent contact radius
l	10 mm	Length contact area
a	6.77×10^{-4} m	Contact area half-width
p_{max}	5.6 MPa	Maximum contact stress
σ_{yield}	50 MPa	Yield stress bearing [57]

A sleeve bearing (iGlide P210, igus, Inc., Rumford, RI, USA) supports the end of the pin within the actuator housing. The bearing was selected in order to support the loads induced from the loading of the spring while the pin is engaged, the polymer bearing is preferable to a metal bearing due to the intermittent motion of this

application. A Hertzian model of line contact was used to calculate the maximum expected contact stress on the bearing. I first determine the expected loads on the bearings based on the stiffness ratio of the actuator stiffness to total system stiffness to calculate the portion of the total load on the actuator and therefore on the bearing. I calculate the maximum contact pressure on the bearing as 5.6 MPa [51]. I selected the bearing based on this expected load and the unique requirements of intermittent motion and intermittent load application.

$$a = \sqrt{\frac{4Pr_c}{\pi E_c}} = .677mm \tag{3.40}$$

$$r_c = \left(\frac{1}{r_1} + \frac{1}{r_2}\right)^{-1} = 186.3mm \tag{3.41}$$

$$E_c = \left(\frac{1-v_1^2}{E_1} + \frac{1-v_2^2}{E_2}\right)^{-1} = 2.9GPa \tag{3.42}$$

The maximum contact pressure occurs in the center of the contact at x=0, as defined by Equation 3.43.

$$p_{max} = \frac{2P}{\pi a} = 5.3MPa \tag{3.43}$$

Contact stress at pin-slot interface

I modeled the contact stress at the interface between the locking pins and the slots in the carbon fiber leaf springs. I calculated the portion of the total load seen by the pin-slot interface during loading by the stiffness ratio between each parallel spring and the total stiffness from our parametric stiffness model. The portion of the total load seen by each spring is equivalent to the total load times the stiffness ratio of the spring of interest to the total stiffness. In order to calculate the maximum stress at the contact area between the pin and slot, the Hertzian theorem of line contact is used [52]. I calculate the contact area half-width a (Equation 3.44), equivalent contact radius r_c (Equation 3.45), and equivalent elastic modulus E_c (Equation 3.46)

using the values in Table 3.6. I calculate an estimated maximum contact stress of 373 MPa (Equation 3.47), which gives us a safety factor of 3.3 above the yield stress of 4140 PH steel. Fig. 3-12 shows the subsurface shear stress in the bushing, which is a maximum at a depth of 0.78a, which is within the bushing.

$$a = \sqrt{\frac{4Pr_c}{\pi E_c}} = 0.107mm \tag{3.44}$$

$$r_c = \left(\frac{1}{r_1} + \frac{1}{r_2}\right)^{-1} = 19.1mm \tag{3.45}$$

$$E_c = \left(\frac{1-v_1^2}{E_1} + \frac{1-v_2^2}{E_2}\right)^{-1} = 110.5GPa \tag{3.46}$$

The maximum contact pressure occurs in the center of the contact at x=0, as defined by Equation 3.47.

$$p_{max} = \frac{2P}{\pi a} = 308.6MPa \tag{3.47}$$

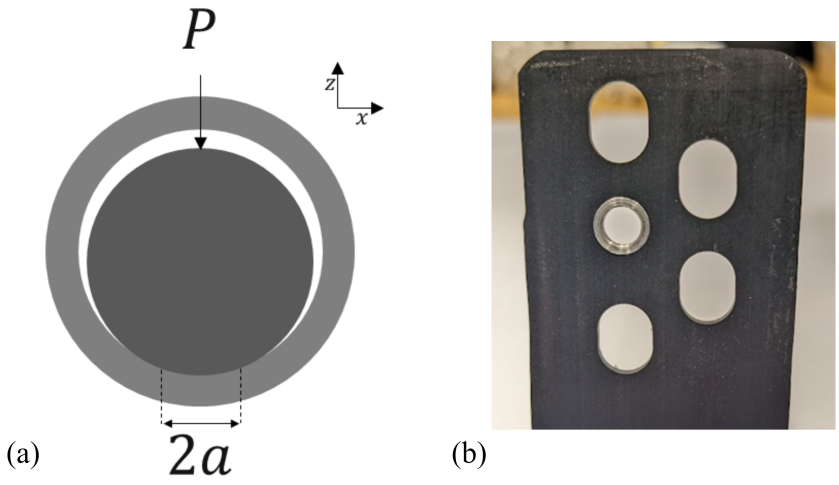

Figure 3-11: **Contact stress at pin - slot interface.** Contact stress at slot interface is calculated using Hertzian contact theory, (a) the contact area between the pin and the slot is modeled as a cylinder in contact with a flat plate, (b) the maximum contact stress occurs at the inner radius of the bushing.

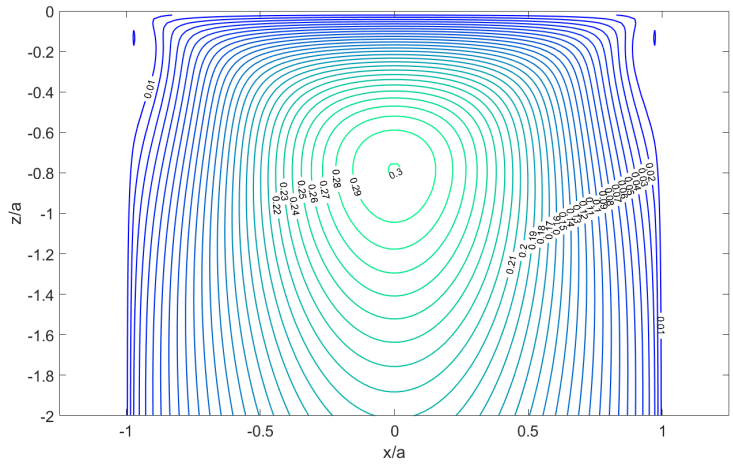

Figure 3-12: **Subsurface shear stress at pin-slot interface.** Subsurface shear stress plotted relative to contact area half-width, a, and subsurface depth as a ratio of contact area half-width, z/a. The maximum subsurface shear stress occurs at a depth of -0.78a.

Table 3.6: Variables and values for contact stress calculations at pin interface

Parameter	**Value**	**Description**
v_1	0.29	Poisson's ratio pin [55]
v_2	0.29	Poisson's ratios bushing [55]
E_1	205 GPa	Elastic modulus pin [55]
E_2	205 GPa	Elastic modulus bushing [55]
E_c	112 GPa	Equivalent Elastic modulus
r_1	2.3 mm	Radius pin
r_2	-2.6 mm	Radius bushing
l	1.742 mm	Length contact area
a	0.107 mm	Contact area half-width
p_{max}	308.6 MPa	Maximum contact stress
τ_{max}	92.6 MPa	Maximum subsurface shear stress
σ_{yield}	1240 MPa	Yield stress 4140 PH [58]

3.1.6 Housing Design

The prosthesis housing is fabricated from 7075 aluminum. The base spring is bonded to the housing with an adhesive and bolted joint. A pyramid adapter is mounted on the front of the housing, allowing the prosthesis to be mounted to a prosthetic socket via standard mounting hardware.

Finite element analysis of housing

I performed finite element analysis (FEA) on all structural components of the system using SolidWorks Simulation (SolidWorks, Dassault Systems, Vélizy-Villacoublay, France). I used a static structural analysis with a load of 1.5x body mass. I determined that the maximum stress in the housing components is lower than the fatigue limit of 7075 aluminum for 2×10^6 cycles.

Bolted joint design

The bolted joint between the anterior and posterior housing components as well as the bolted joint between the pyramid adapter and housing were analyzed to determine sufficient joint strength for our expected loads. The housing, which encloses the springs and transfers load from the pyramid adapter to the ground spring, consists of two components held together with a bolted joint connection. I first calculate the portion of the force seem by each bolted joint for a force applied to the toe of the prosthesis (worst case loading scenario). There are two bolted connections at each r_1 and r_2 that we assume will see equal forces.

$$M = F_l l = 2F_1 r_1 + 2F_2 r_2 \tag{3.48}$$

$$tan\theta = \frac{\delta_1}{r_1} = \frac{\delta_2}{r_2} \tag{3.49}$$

$$\frac{\delta_1}{\delta_2} = \frac{r_1}{r_2} \tag{3.50}$$

$$k_{joint1} = k_{joint2} = k_{joint} \tag{3.51}$$

$$F_1 = k_{joint}\delta_1 \tag{3.52}$$

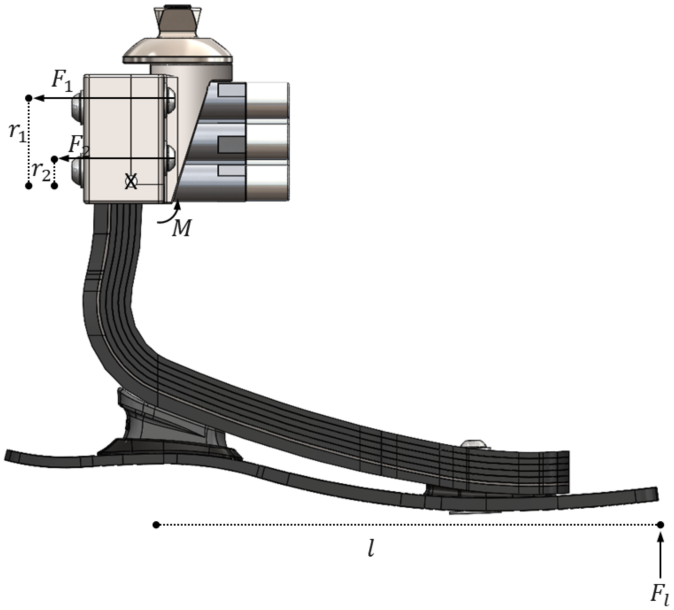

Figure 3-13: **Bolted joint analysis housing.** Free body diagram to determine loading on bolts in housing for a worst case scenario loading of a load applied to the distal end of the prosthesis.

$$F_2 = k_{joint}\delta_2 = k_{joint}\delta_1\frac{r_2}{r_1} \tag{3.53}$$

$$F_1 = \frac{r_1}{r_2}F_2 \tag{3.54}$$

$$F_l l = 2F_1 r_1 + 2F_2 r_2 = 2F_2\frac{r_1}{r_2}r_1 + 2F_2 r_2 \tag{3.55}$$

$$F_2 = \frac{\frac{1}{2}F_l l}{\frac{r_1^2}{r_2} + r_2} \tag{3.56}$$

$$F_1 = \frac{r_1}{r_2}F_2 = \frac{\frac{1}{2}F_l l r_1}{r_1^2 + r_2^2} \tag{3.57}$$

We now have the force on each bolted joint as a function of the applied load on the prosthesis. We now can calculate the force seen by both the bolt and the material by calculating the stiffnesses of each component. Equation 3.58 is used to calculate the

Table 3.7: Variables and values for bolted joint analysis housing

Parameter	**Value**	**Description**
F_l	1133 N	Applied load on prosthesis
$F_{preload}$	1780 N	Bolt preload
l	180 mm	Moment arm applied load to bolted joint
r_1	30 mm	moment arm to bolted connection 1
r_2	10.5 mm	moment arm to bolted connection 2
α	0.524 rad	Half-apex angle
E_{bolt}	210 GPa	Young's Modulus of bolt (steel)
d_{bolt}	4.134 mm	Minor diameter of bolt
A_{bolt}	$1.34 \times 10^{-5} m^2$	Cross sectional area of bolt
L_{bolt}	20 mm	Length of bolt
σ_{yield}	720 MPa	Yield stress of bolt (Class 10.9 Alloy Steel) [59]
$E_{material}$	70 GPa	Young's Modulus of housing material (7074-T6 Al)
d_{hole}	6 mm	Diameter of clearance hole in housing material
d_{washer}	12.5 mm	Diameter of washer
t	11 mm	Thickness of housing material section
k_b	$1.41E+08 N/m$	Bolt stiffness
k_{m1}	$2.23E+09 N/m$	Material stiffness section 1
k_{m2}	$1.47E+09 N/m$	Material stiffness section 2
k_{joint}	$1.03E+09 N/m$	Material stiffness total bolted section
F_1	3028 N	Force on bolted connection 1
F_2	1060 N	Force on bolted connection 2
F_{b1}	415 N	Force on bolt 1
F_{b2}	145 N	Force on bolt 2
F_{m1}	2613 N	Force on material 1
F_{m2}	1228 N	Force on material 2
σ_{bolt}	164 MPa	Stress on bolt
FOS_σ	4.40	Safety factor for yield stress of bolt
$FOS_{separation}$	6.11	Safety factor for separation of bolted joint

material stiffness of the housing in the bolted joint connection [59]. Equation 3.59 calculates the total stiffness of the material based on the two housing components loaded in series. The stiffness of the bolt is calculated in Equation 3.60 [59]

$$k_m = \frac{\pi E d tan\alpha}{ln\frac{(2ttan\alpha+D-d)(D+d)}{(2ttan\alpha+D+d)(D-d)}} \tag{3.58}$$

$$k_{mtot} = (\frac{1}{k_{m1}} + \frac{1}{k_{m2}})^{-1} \tag{3.59}$$

$$k_b = \frac{A_b E_b}{l} \tag{3.60}$$

$$k_{joint} = k_m + k_b \tag{3.61}$$

$$F_{bolt} = \frac{k_b}{k_{joint}} F_{total} \tag{3.62}$$

$$F_{material} = \frac{k_m}{k_{joint}} F_{total} \tag{3.63}$$

$$F_{b1} = \frac{k_b}{k_{joint}} F_1 \tag{3.64}$$

$$F_{m1} = \frac{k_m}{k_{joint}} F_1 \tag{3.65}$$

I use these equations to calculate the force seen by each the bolt and the material of the bolted connection when a load is applied to the system. The load in each bolt (F_{b1} and F_{b2}) is seen as an elongation force on the bolt. A failure mode of the bolted joint will occur if the elongation force is greater than the preload force such that the material held together by the bolted joint is allowed to separate, subjecting the bolts to a shear load. Therefore the preload force in the bolt must be greater than the portion of the applied force that is seen as an elongation force on the bolt for all loading scenarios. We must also consider the stress in the bolt under the loading of the bolt preload as well as elongation force on the bolt.

$$\sigma_{bolt} = \frac{F_{preload}}{A_{bolt}} + \frac{F_{bolt}}{A_{bolt}} \tag{3.66}$$

Table 3.8: Variables and values for bolted joint analysis pyramid adapter

Parameter	**Value**	**Description**
F_l	1133 N	Applied load on prosthesis
$F_{preload}$	8322 N	Bolt preload
l	180 mm	Moment arm applied load to bolted joint
r_3	20 mm	moment arm to bolted connection 1
α	0.524 rad	Half-apex angle
E_{bolt}	210 GPa	Young's Modulus of bolt (steel)
d_{bolt}	8.4 mm	Minor diameter of bolt
A_{bolt}	$5.5 \times 10^{-5} m^2$	Cross sectional area of bolt
L_{bolt}	12.5 mm	Length of bolt
σ_{yield}	720 MPa	Yield stress of bolt (Class 10.9 Alloy Steel) [59]
$E_{material1}$	110 GPa	Young's Modulus of pyramid (Ti)
$E_{material2}$	70 GPa	Young's Modulus of housing (7075-T6 Al)
d_{hole}	11 mm	Diameter of clearance hole in housing material
d_{washer}	20 mm	Diameter of washer
t_1	3.5 mm	Thickness of housing material section 1
t_2	9 mm	Thickness of housing material section 2
k_b	$9.31E+08 N/m$	Bolt stiffness
k_{m1}	$8.84E+09 N/m$	Material stiffness section 1
k_{m2}	$4.59E+09 N/m$	Material stiffness section 2
k_{joint}	$3.95E+09 N/m$	Material stiffness total bolted section
F_1	10197 N	Force on bolted connection 1
F_{b1}	2400 N	Force on bolt 1
F_{m1}	7794 N	Force on material 1
σ_{bolt}	194 MPa	Stress on bolt
FOS_σ	3.72	Safety factor for yield stress of bolt

$$\sigma_{b1} = \frac{F_{preload} + F_{b1}}{A_{bolt}} \tag{3.67}$$

This process is repeated for the bolted joint between the pyramid adapter and the housing. Fig. 3.1.6 shows the loading on the bolted joint, where F_3 is the elongation force on the bolt for applied loads F_l. r_3 is the moment arm between the elongation force and the pivot point of the pyramid adapter. l is again the moment arm between the load and the pivot point.

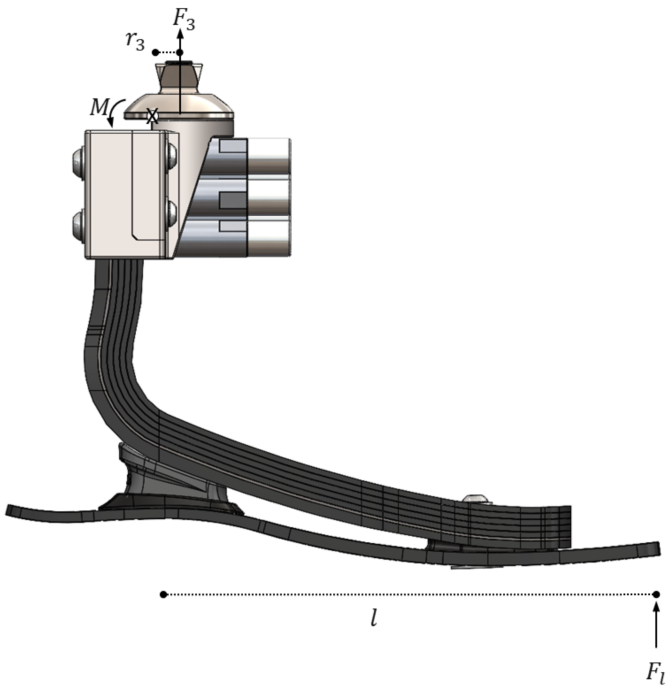

Figure 3-14: **Bolted joint analysis pyramid adapter.** Free body diagram for bolted joint analysis to determine loads on pyramid adapter.

3.1.7 Control System and Electronics Design

As the novel actuator architecture exhibits unique electromechanical properties, designing a custom embedded system for the VSA provides significant benefits in order to reduce redundancy and optimize performance compared to using a generic motor driver system. We therefore designed and implemented a custom embedded system to drive the solenoid actuators, interface with the onboard sensors, and to enable running closed-loop control. The variable stiffness prosthesis has higher controllable degrees-of-freedom compared to standard powered prostheses, with five individual actuators, and therefore has unique requirements for the embedded system. This system demonstrates much lower current requirements and a faster transient response than continuous rotary actuation, and therefore the use of traditional motor drivers in the variable stiffness ankle would cause system redundancy and inefficiency.

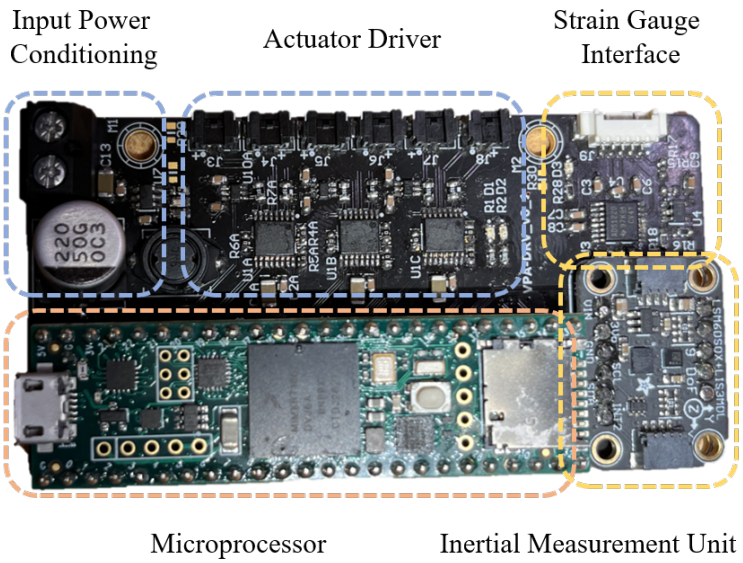

Figure 3-15: **Embedded system.** Prototype of the designed and fabricated embedded system for the VSA.

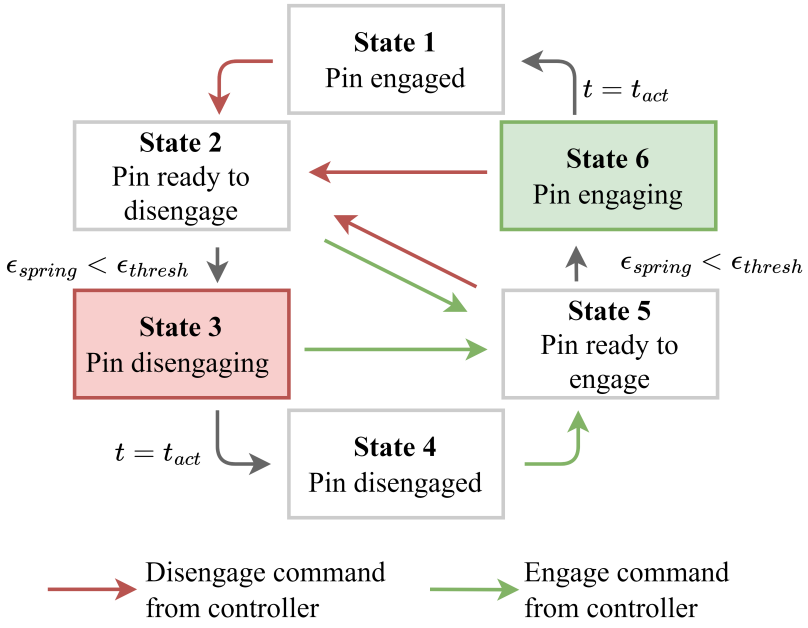

Figure 3-16: **Low-level finite state machine of the VSA driver.** The energy efficient control scheme only requires energy for the actuator when the actuator is actively engaging in State 6 (green) or disengaging in State 3 (red). During State 1, State 2, State 4, and State 5 (grey), no additional power is required to hold actuator position due to the device architecture.

Approximation of actuator dynamics

The proposed actuator exhibits complex electromechanical dynamics. With an electrical solenoid, mass of mechanical pin, and quasi-static magnetic interaction, modeling

dynamics of the system becomes significantly complex. Additionally, utilizing the full characterization of electromechanical dynamics into the controller would require high-bandwidth closed-loop control on the order of $> 10kHz$ as well as sensing of the mechanical states of the actuators. Given the engineering trade-offs of such an implementation, we created a simplified model of the actuator dynamics with a constant input voltage and pre-determined minimum actuation time for each direction of actuation. This approach guarantees convergence of the system to the desired final state from a known initial state and enables the desired performance of the mechatronics system without necessitating additional mechanical state sensing modalities.

Embedded system hardware

The embedded system hardware for the variable stiffness ankle is shown in Fig. 3-15. We designed the hardware with an emphasis on 1) the unique actuators characteristics, 2) scalability to ensure compatibility with future iterations of the variable stiffness ankle, 3) multiple sensors for thorough analysis of the system behaviors, and 4) a researcher-friendly user interface. On the actuator driving front-end, three dual channel motor driver chips (DRV8847PWR, Texas Instruments, Dallas, TX, USA) control five solenoid actuators with a maximum root-mean-square (RMS) current of 1 A. There are six driving output channels to allow for the use of additional actuators during potential future iterations of hardware. The current output of each channel is monitored through a serial current sensing resistor (10 mOhm) and an instrumental amplifier (INA186A3, Texas Instruments, Dallas, TX, USA). The embedded system is also equipped with a strain-gauge interface front-end including a precision 24-bit analog-to-digital-converter (ADC, ADS1220IPW, Texas Instruments, Dallas, TX, USA) and active analog excitation driver (OPA376, Texas Instruments, Dallas, TX, USA) powered with a separate low-noise power conditioning chip (TPS79301, Texas instruments, Dallas, TX, USA) for the strain-gauge installed on the leaf spring. A commercial inertial measurement unit (IMU) protoboard (ISM303DHCX, Adafruit Industries, New York, NY, USA) is used for possible kinematics estimation. A 32-bit commercial prototyping microprocessor board (Teensy 4.1, PJRC, Portland, OR,

USA) controls all the drivers and peripherals on the board. Use of the commercial board enables greater accessibility to control system and enables faster development and iteration. The embedded system is designed to operate with a bandwidth of 2kHz to interface with all sensors and control actuators while the actual bandwidth could be lower depending on the desired control algorithm. The operating voltage of the system is in between 6-24V. The system is powered by a 4-cell (14.8 V) lithium polymer battery with a battery capacity of 650 mAh. A wide-range switched mode power supply (LMR50410Y-Q1, Texas Instruments, Dallas, TX, USA) converts to lower voltage level to operate the digital/analog peripherals on the board. The overall footprint of the system is 83.95 mm by 43.94 mm.

Onboard sensors

Sensors onboard the system monitor device parameters. A strain gauge (CEA-06-250UTA-350, Micro Measurements, Raleigh, NC, USA) is mounted to the ground spring, which allows for measuring spring strain during device use. An IMU (ISM303DHCX, Adafruit Industries, New York, NY, USA) on the embedded system allows for the potential to estimate walking speed and terrain during walking. Current sensors measure the current for each actuator.

Baseline control architecture

We established a baseline control architecture to ensure maximal efficiency of the variable stiffness ankle. The binary solenoid actuator should only be actuated when binary state transition is required. The actuator should be locked when the variable stiffness ankle prosthesis on stance phase of the gait bearing a subject's weight. We devised a simple finite state machine (FSM) to incorporate the safety conditions above on low-level controller for future high-level control development as shown in Fig. 3-16. A pre-determined time constant was utilized to estimate individual actuator states. We tuned voltage level and time constants of individual actuators empirically.

3.2 Benchtop Evaluation Methods

This section describes the methods and results from benchtop device evaluation.

3.2.1 Mechanical Evaluation

Stiffness characterization

(a) (b)

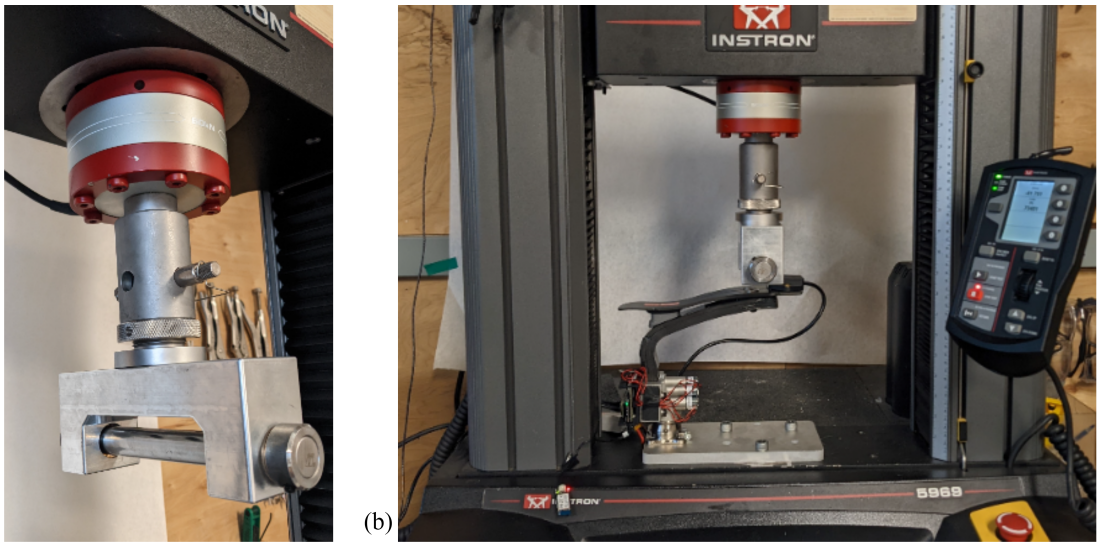

Figure 3-17: **Test fixture.** Custom test fixture integrates directly with material testing system for stiffness and stress evaluation tests.

I evaluated the stiffness of the prosthesis through benchtop testing performed on a material testing system (Model 5969 Material Testing System, Instron, Norwood, MA). For each of the 32 distinct stiffness settings, the device was loaded to a maximum load of 700N at a rate of 50N/s, and deflection of the prosthesis at the point of load application was measured. In order to conduct the benchtop evaluation experiments, a custom test fixture was designed to directly integrate with a material testing system (Figure 3-17). The test fixture applies the load in line with the load cell in order to remove moment induced errors from the load cell (Figure 3-18). A digital inclinometer (AXISENSE-2 USB90, TE Connectivity, Schaffhausen, Switzerland) is used to measure the angular deflection of the prosthesis during benchtop testing.

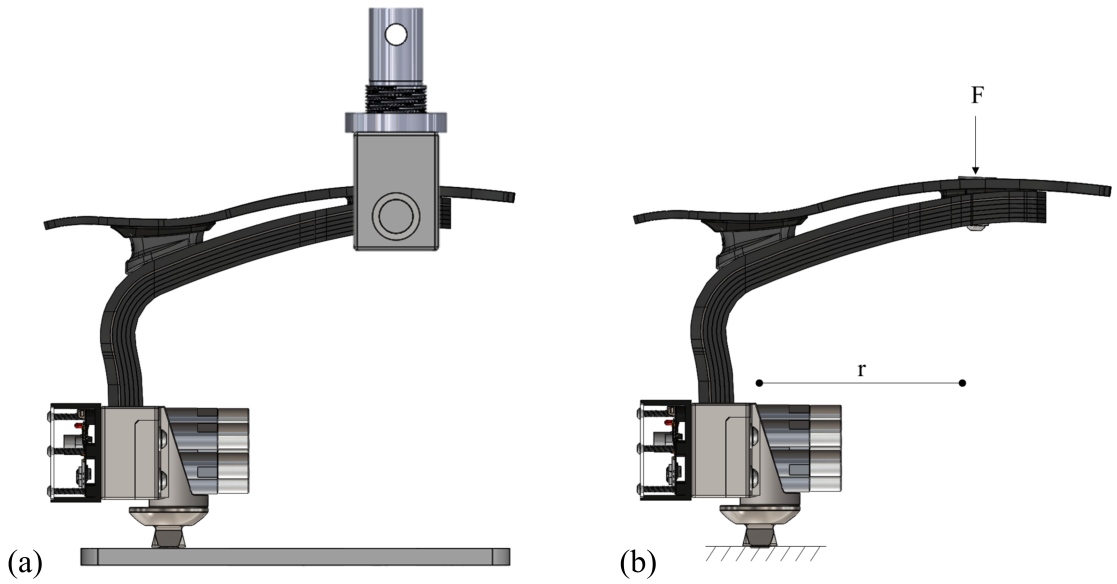

Figure 3-18: **Test fixture design.** Prosthesis testing test fixture is designed to isolate moment loads from the load cell in order to minimize measurement errors.

Stress measurements

Strain in the leaf spring was measured with a strain gauge installed on the ground spring, the gauge is configures in a half-bridge type I circuit. Details of strain gauge are outlined in Table 3.10. Strain was measured during benchtop testing on the custom Instron test fixture.

3.2.2 Electromechanical Evaluation

Actuator characterization

We performed electromechanical characterization of the actuator. First, we characterized the minimum required actuation time to engage and disengage the actuators for a given input voltage. We then observed transient current response of the actuator with the determined minimum actuation time of the actuator. Total energy consumption analyses were made based on the transient response analyses. During the actuator characterization, the embedded system ran with a bandwidth of 5 kHz.

3.3 Device Validation Results

3.3.1 Mechanical Characterization

Device mass

The mass of the device is presented in Table 3.9. The total device mass of 945 grams includes the battery and electronics, and excludes the cosmetic foot cover.

Max strain and stress

Max strain in the leaf springs was measured directly from a strain gauge mounted on the ground spring during bench top testing to validate mechanical modeling results of the spring design. A maximum strain of 0.16% was measured, corresponding to a maximum stress value of 210 MPa (Fig. 3-20). I calculate strain (in microstrain) from the raw strain gauge reading as in Equation 3.68. Stress is calculated from the strain reading as in Equation 3.69.

Table 3.9: Device Mass.

Component	**Mass (g)**	**Qty**
Leaf springs	370	1
Housing	170	1
Battery	78	1
Hardware	67	Various
Pyramid adapter	53	1
Embedded system	37	1
Actuator assembly	26	5
Urethane bumper	22	1
Electronics case	18	1
Total	**945**	

Stiffness characterization

Fig. 3-19a shows the torque angle plot of the variable stiffness ankle prosthesis from the data collected during benchtop Instron testing. Fig. 3-19b shows the correspond-

ing stiffness for each independent stiffness state. There are 32 distinct stiffness states, with the range of stiffnesses from lowest to highest stiffness settings creating a 36% increase in joint stiffness of the ankle. The target stiffness range of 352 Nm/rad - 479 Nm/rad was validated during benchtop testing.

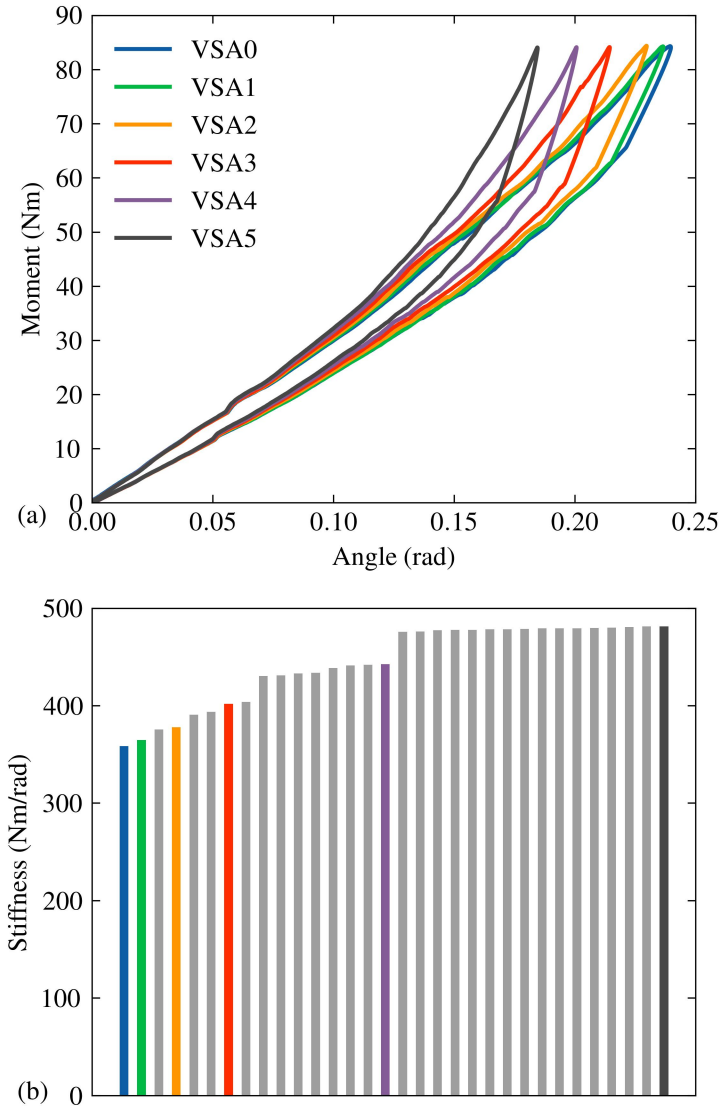

Figure 3-19: **Stiffness range of variable stiffness prosthesis.** (a) Torque – angular displacement curves of variable stiffness ankle-foot prosthesis from benchtop validation, (b) rotational stiffness of VSA at each stiffness state.

$$\epsilon = \frac{-4V_r}{GF[(1+v) - 2V_r(v-1)]}\left(1 + \frac{R_L}{R_G}\right) \tag{3.68}$$

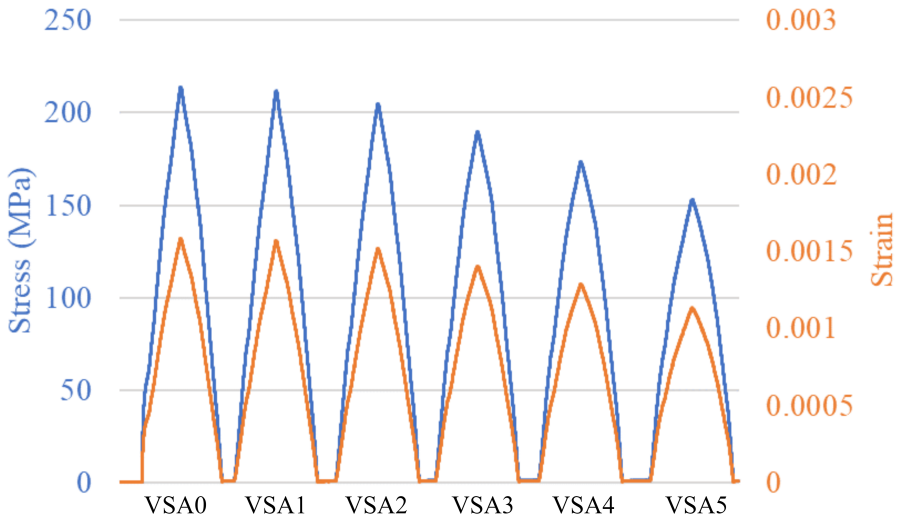

Figure 3-20: **Strain gauge data.** Measured strain and calculated stress values from benchtop testing.

Table 3.10: Strain gauge.

Parameter	Value	Description
ϵ		Strain
V_r		Voltage ratio
R_L	10 $m\Omega$	Lead resistance
R_G	350 Ω	Grid resistance [60]
v	0.5	Poisson's ratio of strain gauge [60]
GF	2.015	Gauge factor of strain gauge [60]
E	135 GPa	Elastic modulus of carbon fiber [47]
σ		Stress in carbon fiber

$$\sigma = E\epsilon \tag{3.69}$$

ISO standards

The structural analysis and initial benchtop evaluation suggest that the device would successfully meet ISO standards for structural evaluation of a prosthesis (Table 3.11). Further testing is necessary to evaluate if the prosthesis meets ISO standards for ultimate static loading and cyclic loading.

Table 3.11: ISO Standards

Parameter	**ISO Standard**	**Analysis meets standard?**
Ultimate static test	$3.4 - 4.6\times$ body mass [44]	Yes
Cyclic test (load)	$0.05 - 1.36\times$ body mass [44]	Yes
Cyclic test (# cycles)	2×10^6 cycles [44]	Yes

3.3.2 Electromechanical Characteristics

Actuator analysis

Table 3.12 summarizes the electromechanical characteristics of the system including minimum required actuation times for engaging and disengaging actuators, peak current during actuation, quiescent current, and idle power of the embedded system running at bandwidth of 1 kHz. A higher actuation voltage corresponds to faster actuation and higher actuation force, while actuation current levels increased proportionally to actuation voltage. A higher input voltage for the embedded system consumes greater idle energy due to the efficiency difference of the input-stage switched mode power supply (SMPS) converter. During actuation, a higher input voltage generally consumes more energy, although 9 V input voltage consumes less energy during actuator engagement than 6 V. Fig. 3-21 shows the transient electrical response of the actuator. The electromechanical evaluation demonstrates that for the selected battery voltage of 12 V, the battery life is approximately 10 hours if we assume 1 actuator state change every 10 steps, and 11 hours of standby power.

Table 3.12: Summary of electromechanical characteristics.

Voltage (V)	T Engage (ms)	T Disengage (ms)	Peak Current Engage (mA)	Peak Current Disengage (mA)	E Engage (mJ)	E Disengage (mJ)	Quiescent Current (mA)	Idle Power (mW)
6	7.6	20.4	382	413	15.5	48.8	99	594
9	3.4	10.6	537	617	13.45	56.9	71	638
12	2.6	7.4	685	815	17.3	69.2	57	684
15	2	5.8	813	1020	22.0	87.0	47	705

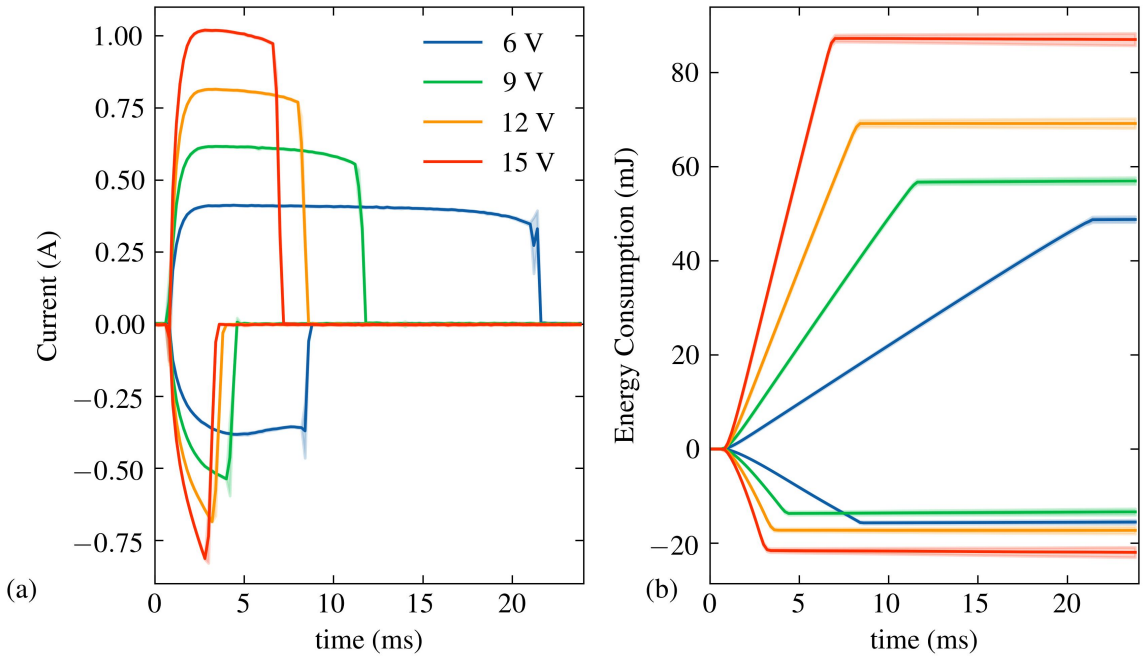

Figure 3-21: **Electrical transient characteristics of the actuator.** (a) Transient current response of linear actuator for a given voltage level. (b) Accumulated transient energy consumption of the actuator for a given voltage level.

3.4 Discussion

3.4.1 Design

This chapter presents the development of a novel mechanism for varying bending stiffness of leaf springs and the detailed design and analysis of a variable stiffness ankle-foot prosthesis for walking speed adaptation. I describe the fundamental concepts behind the stiffness control mechanism, and mathematically describe the method for achieving high-resolution stiffness control. I present mechanical design analysis of the device including parametric model for approximating device stiffness, contact stress analysis, fatigue life calculations, and bolted joint analysis.

3.4.2 Device Evaluation

Mechanical evaluation

The benchtop testing results demonstrate that the device successfully achieves the targeted stiffness range, device mass, and structural integrity. The benchtop stiffness characterization of the system demonstrates the high-resolution stiffness control of the prosthesis. The mass of the variable stiffness prosthesis is lower than all existing commercial quasi-passive devices, and lower mass than all research platforms. I demonstrate that the VSA prosthesis successfully matches biological levels of ankle stiffness for a person of our target body mass ranging from a slow walk (0.75 m/s) to a fast walk (1.5 m/s).

Electromechanical system

We also show that the proposed embedded system concept and low-level control architecture can provide stable control of the electromechanical actuators. The results demonstrate that the simplified dynamic model of the actuator provides effective means to construct the control system with minimal sensors. Lower input voltages generally consume less energy in the idle state and during transient actuation. While the electro-magnetic-mechanical system shows multi-order complex dynamics, the results demonstrate that the dynamics can be simplified with a constant actuation time and voltage to ensure stable end-state after actuation.

3.5 Future Work

Future work on the design of the system includes implementing closed loop real-time control, further testing and analysis on fatigue life of the system, and expanding the parametric model and design process to design devices for additional weight categories of users. In future iterations of the design, the embedded system can be greatly reduced in size and the continuous power consumption of the electronics can be greatly reduced through design optimizations of the electronics.

3.5.1 Real-Time Closed Loop Control

Walking speed optimization

Future work includes development of a real-time closed loop control system for stiffness control of the prosthesis. Prior art has demonstrated the detection of terrain and estimation of walking speed through the use of a single foot-mounted IMU [61–63]. By implementing similar techniques, we can estimate walking speed and terrain (steps, ramps) in real-time onboard the embedded system. This control system will determine optimal stiffness based on walking speed or terrain. A state machine in Figure 3-22 explains how this controller would function. Sensors onboard the prosthesis include a strain gauge and an IMU. Using the IMU we can estimate walking speed and terrain, and determine the optimal stiffness state for the conditions. Based on the desired stiffness state, the embedded system will send a command to the motor drivers to control the position of each actuator to that corresponding to the desired stiffness state. The strain gauge onboard the embedded system allow for future kinematics estimation onboard the device, in order to estimate walking speed and terrain in real time.

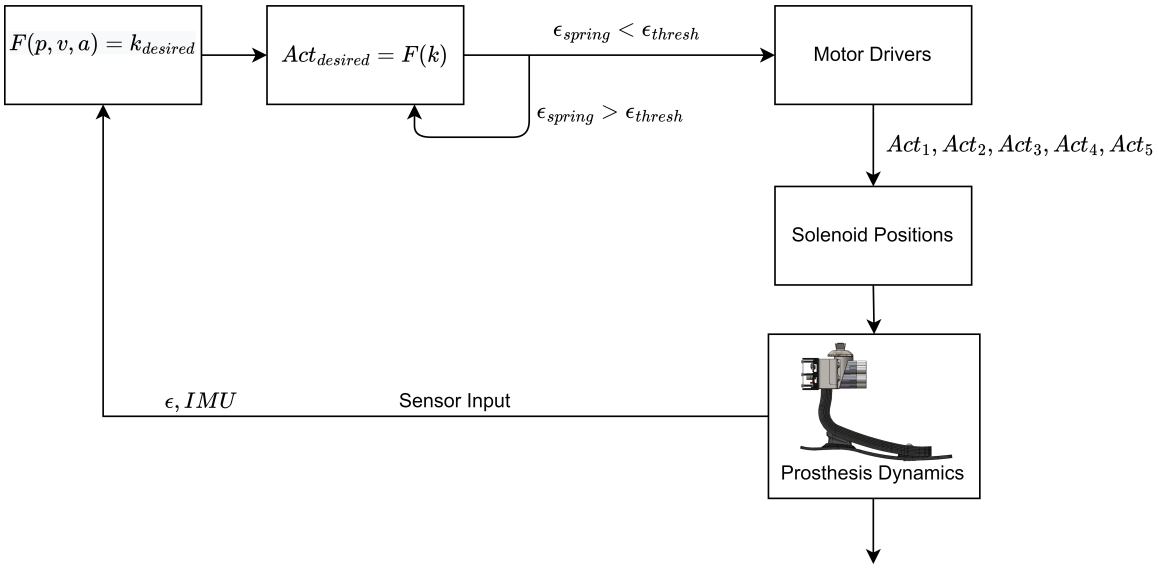

Figure 3-22: **Control diagram.**

Energy maximization

Another possible control strategy is to control device stiffness in order to maximize energy storage. Through the strain gauge measurement and known stiffness state of the prosthesis, we can estimate joint angle of the prosthesis and calculate energy storage.

User input

Another possible control paradigm is a user-controlled model in which the user is able to select prosthesis stiffness directly. In this paradigm, the user would have access to an adjustment through a mobile application or other user interface. Prior work has demonstrated that prosthesis users are able to select their preferred prosthesis stiffness with high repeatability [64].

3.5.2 Product Design Considerations

The variable-stiffness prosthesis can be scaled in order to correspond to users of different body masses, as discussed in Section 3.1.3. In addition to body mass, the device design will change based on foot size. In order to adjust to users of different masses, J-springs may be designed for each category of weight and activity category, similar to how passive protheses are manufactured. Figure 3-23 shows the standard weight categories that Ottobock uses for it's passive devices [16], as well as the stiffness range that should be implemented in a variable stiffness prosthesis for that weight range [32]. Foot size may be adjusted independently of body-mass range, by installing the base spring corresponding to foot size during assembly of the device.

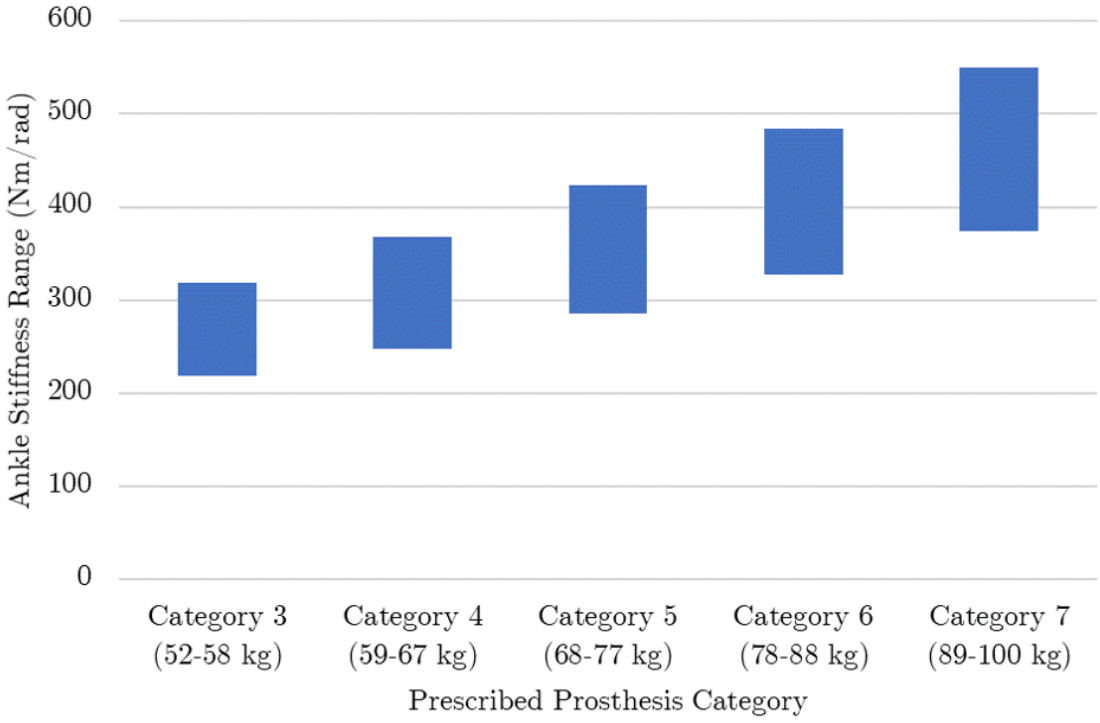

Figure 3-23: **Stiffness Range.**

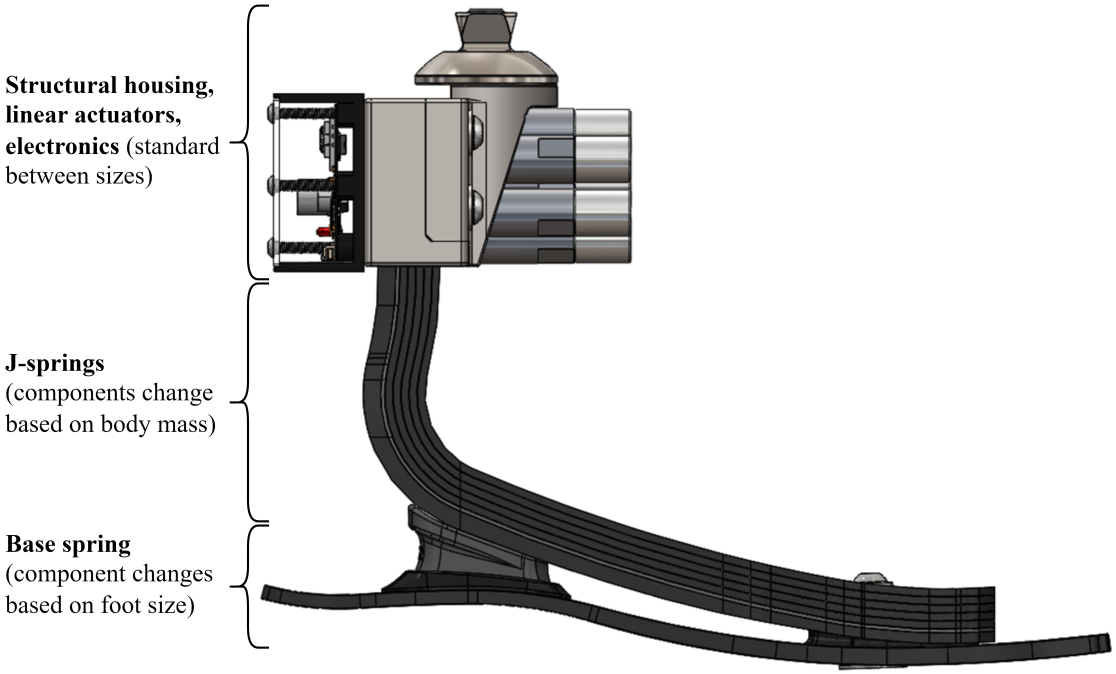

Figure 3-24: **Product design.** Designing variable stiffness prosthesis for various body masses and foot sizes.

Chapter 4

Clinical Evaluation

This chapter presents the clinical evaluation methods, results, and analysis. I first go over the experimental methods, data collection procedures, details of study participants, and statistical and data analysis methods. I then present kinematic and kinetic results from the study, discussion, and future work.

4.1 Experimental Methods

A study was conducted with 7 participants with unilateral transtibial amputation in order to evaluate the kinetic and kinematic effects of the variable stiffness prosthesis during walking compared to a passive ESR control foot. This study was approved by the MIT Committee on the Use of Humans as Experimental Subjects (protocol number: 1609692618A010, approval date: November 1, 2018), and written informed consent was obtained. During the experiment, subjects walked on an instrumented treadmill (FIT, Bertec, Columbus, OH) at the speeds of 0.75 m/s, 1.0 m/s, 1.25 m/s, and 1.5 m/s. Participants walked for 30 seconds for each trial for a total of 28 trials were performed. Study conditions included the variable stiffness prosthesis at 6 distinct stiffness states, as well as a standard passive ESR prosthesis of the subject's prescribed size and category (Taleo 27-5 or 27-6, Ottobock, Duderstadt, Germany). The order of the trials for each stiffness state was randomized.

4.1.1 Data Collection

A 12-camera motion capture system (Vero, Vicon Industries, Inc., Hauppauge, NY) was used to collect kinematic data (100 Hz). A custom full-body marker set based on the open source '3DGaitModelwithSimpleArms' marker set was used for kinematic data collection, with 5 markers on each foot, 7 on each shank, 7 on each thigh, 4 on the pelvis, 5 on the torso, 4 on each upper arm, 4 on each lower arm, 4 on each hand, and 5 on the head. A split belt treadmill with integrated force plates (FIT, Bertec, Columbus, OH) was used to collect kinetic data (1000 Hz). Video was recorded for each trial. Data from onboard sensors on the prosthesis (strain gauge, IMU, current sensors) was logged for each trial (500 Hz).

4.1.2 Study Participants

Seven people with unilateral transtibial amputation (body mass: 81.5 ± 4.4 kg, height: 1.81 ± 0.08 m, age: 49.9 ± 4.0 years, time since amputation: 18.7 ± 15.5 years, sex: male) participated in the study. Details the of study participants are outlined in Table 4.1.

Table 4.1: Study participant information.

Identifier	Body mass (kg)	Height (m)	Leg length (m)	Age (years)	Years since amputation	Sex
Subject 1	82.6	1.83	1.00	49	30	Male
Subject 2	86.5	1.91	1.05	51	29	Male
Subject 3	74.8	1.73	0.88	58	6	Male
Subject 4	78.5	1.81	0.92	46	5	Male
Subject 5	83.7	1.70	0.84	50	8	Male
Subject 6	86.1	1.91	0.98	48	44	Male
Subject 7	78.6	1.78	0.94	47	9	Male

4.1.3 Data Analysis

I processed the data using OpenSim (OpenSim 4.3, Simbios, Stanford, CA). I scaled the mass and inertial properties of the lower leg on the prosthesis based on standard

residual limb dimensions and properties [65]. I adjusted the mass of the lower leg segment to reflect the difference in mass between the variable stiffness device and the ESR device. AddBiomechanics was used to optimally scale the model and run inverse kinematics calculations [66]. Inverse dynamics was performed in OpenSim (OpenSim 4.3, Simbios, Stanford, CA). A 3rd order zero-lag low-pass Butterworth filter was used to filter kinematic (6 Hz) and kinetic (12 Hz) data. The data was segmented into individual gait cycles for each trial, and gait cycles were excluded if the force and torque data was greater than 2 standard deviations from the mean value. The optimal stiffness state for each subject for each speed is defined as the VSA stiffness which minimized contralateral limb external adduction moment.

4.1.4 Statistical Methods

A Shapiro-Wilk test is first performed on all paired results to test for normality of the differences between pairs. For all groups the Shapiso-Wilk test does not reject the null hypothesis, indicating that the distribution of the differences between paired results do not significantly differ from a normal distribution, and it is valid to apply a paired sample t-test to this data. All data is analyzed with a paired t-test with a significance level of 0.05. Statistical analysis is performed in Matlab (MATLAB R2021a, MathWorks, Natick, MA, USA).

4.1.5 Kinematic and Kinetic Analysis

Prosthesis ankle power

Power of the prosthesis is calculated using a unified deformable model due to the tendency of inverse dynamics calculations to inaccurately quantify joint power for a deformable prosthesis without a fixed ankle joint [67, 68]. Prosthesis power is calculated as is Equation 4.1, where F_{grf} is the ground reaction force, M_{grf} is the ground reaction moment, ω_{ud} is the angular velocity of the unified deformable segment, which is equivalent to the angluar velocity of the shank, and v_{ud} is the linear velocity of the unified deformable segment [68].

$$P_{prosthesis} = F_{grf} \cdot v_{UD} + M_{grf} \cdot \omega_{UD} \tag{4.1}$$

$$v_{UD} = v_{UD} + \omega_{UD} \times r_{UDcop} \tag{4.2}$$

Center of mass collision work

Center of mass collision work is calculated as the time integral of center of mass power for the leading limb during collision during the step transition. Center of mass power is determined by taking the dot product of ground reaction force and center of mass velocity, as in Equation 4.3.

$$W_{collision} = \int_{t_1}^{t_2} P_{collision} = \int_{t_1}^{t_2} F_{grfleading} \cdot v_{com} \tag{4.3}$$

Center of mass push-off work

Center of mass push-off work is calculated as the time integral of center of mass power for the trailing limb (prosthesis side) during the step transition. Center of mass power is determined by taking the dot product of ground reaction force and center of mass velocity, as in Equation 4.4.

$$W_{push-off} = \int_{t_1}^{t_2} P_{push-off} = \int_{t_1}^{t_2} F_{grfprosthesis} \cdot v_{com} \tag{4.4}$$

External adduction moment of the knee

External adduction moment of the contralateral limb is calculated through inverse dynamics (Opensim). The internal OpenSim inverse dynamics tool is used to calculate joint torques.

4.2 Clinical Pilot Study Results

4.2.1 Results Across All Subjects

Results from the study are summarized in Table 4.2. The variable stiffness prosthesis demonstrates an increase in peak joint angle, increase in peak power, increase in energy storage and return, and a decrease in contralateral limb external adduction moment for each walking speed compared to the passive prosthesis. Additionally, we see a decrease in the 1st peak of the contralateral limb ground reaction force, a decrease in center of mass collision work on the leading limb, and an increase in center of mass push-off work by the trailing limb across all walking speeds. Figure 4-1 shows the mean value for each VSA stiffness setting as well as the passive Taleo device averaged across all subjects for each speed. Figure 4-2 shows the mean value across gait cycle for all subjects for the optimal VSA stiffness compared to the Taleo at each speed.

Table 4.2: Results for the optimal VSA stiffness and prescribed Taleo at each walking speed. Mean ±s.d., percent change, and significance level are shown for each condition at each speed. Statistically significant results ($p<0.05$) are indicated with a *.

Variable	Prosthesis	Walking Speed			
		0.75 m/s	1.0 m/s	1.25 m/s	1.5 m/s
Peak ankle angle (rad)	Taleo	0.32±0.05	0.34±0.05	0.35±0.07	0.36±0.06
	VSA	0.38±0.04	0.39±0.04	0.40±0.06	0.42±0.06
	% change	+19.3%	+16.8%	+15.5%	+17.4%
	Significance	p<0.001*	p=0.008*	p=0.02*	p<0.001*
Peak prosthesis power (W/kg)	Taleo	1.44±0.29	2.29±0.55	3.06±0.64	3.97±0.91
	VSA	1.66±0.25	2.56±0.42	3.03±0.56	4.18±1.06
	% change	+14.8 %	+11.5%	-1.0%	+5.4%
	Significance	p=0.02*	p=0.02*	p=0.84	p=0.36
Prosthesis energy stored (J/kg)	Taleo	0.19±0.05	0.21±0.05	0.24±0.05	0.25±0.06
	VSA	0.23±0.04	0.26±0.05	0.28±0.04	0.30±0.04
	% change	+24.8%	+21.3%	+19.0%	+17.6%
	Significance	p<0.001*	p<0.001*	p=0.002*	p=0.005*
Prosthesis energy return (J/kg)	Taleo	0.14±0.04	0.17±0.06	0.19±0.05	0.21±0.07
	VSA	0.17±0.03	0.21±0.04	0.21±0.04	0.24±0.08
	% change	+23.6%	+23.7%	+10.5%	+16.4%
	Significance	p=0.04*	p=0.01*	p=0.21	p=0.06
1st peak EAM (Nm/kg)	Taleo	0.58 ±0.25	0.55 ±0.23	0.58 ±0.21	0.69 ±0.23
	VSA	0.54 ±0.24	0.51 ±0.23	0.56 ±0.24	0.64 ±0.22
	% change	-6.0%	-5.9%	-4.0%	-6.7%
	Significance	p=0.01*	p=0.006*	p=0.19	p=0.03*
1st peak GRF (N/kg)	Taleo	10.11±0.55	10.30±0.43	10.96±0.80	12.17±0.90
	VSA	10.08±0.61	9.93±0.66	10.47±0.62	11.77 ±0.80
	% change	-0.3%	-3.6 %	-4.4 %	-3.3%
	Significance	p=0.55	p=0.06	p=0.006*	p=0.005*
COM collision work (J/kg)	Taleo	0.04±0.01	0.08±0.03	0.13±0.03	0.22±0.04
	VSA	0.03±0.02	0.06±0.02	0.10±0.03	0.20±0.04
	% change	-15.6%	-18.7%	-25.2%	-8.8%
	Significance	p=0.09	p=0.03*	p=0.02*	p=0.01*
COM push-off work (J/kg)	Taleo	0.13±0.03	0.15±0.04	0.17±0.04	0.19±0.04
	VSA	0.15±0.03	0.18±0.04	0.21±0.04	0.23±0.06
	% change	+20.2 %	+21.9%	+21.7%	+20.4%
	Significance	p<0.001*	p<0.001*	p=0.002*	p=0.003*

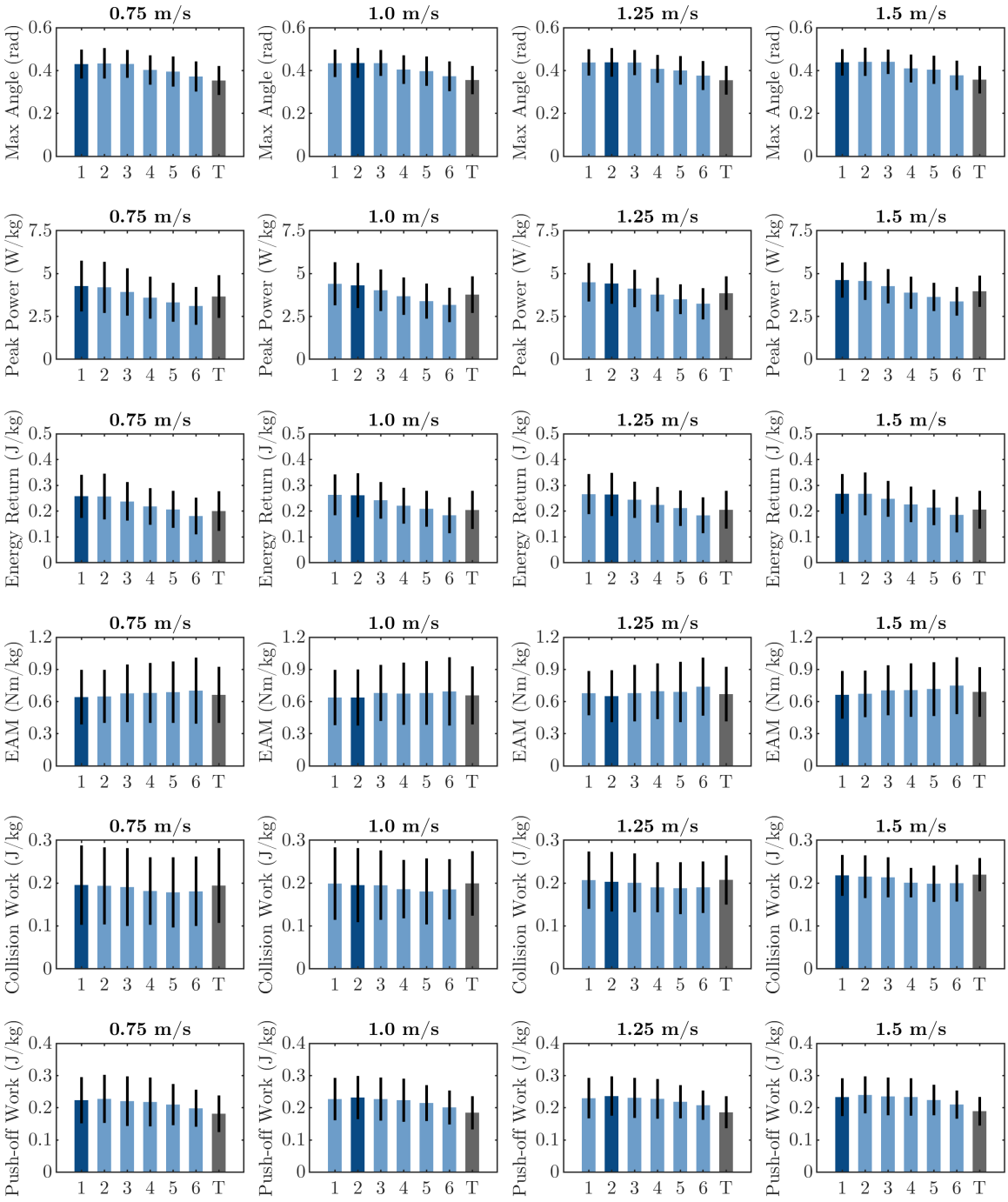

Figure 4-1: **Mean values across subjects.** Mean values for maximum dorsiflexion angle, peak power, energy return, contralateral knee EAM, center of mass collision work, and center of mass push-off work. Data shown for the 6 evaluated VSA stiffness states (blue) and the passive control Taleo (gray). The optimal stiffness across subjects which is defined as minimizing EAM is highlighted (dark blue). Error bars represent ±1 standard deviation.

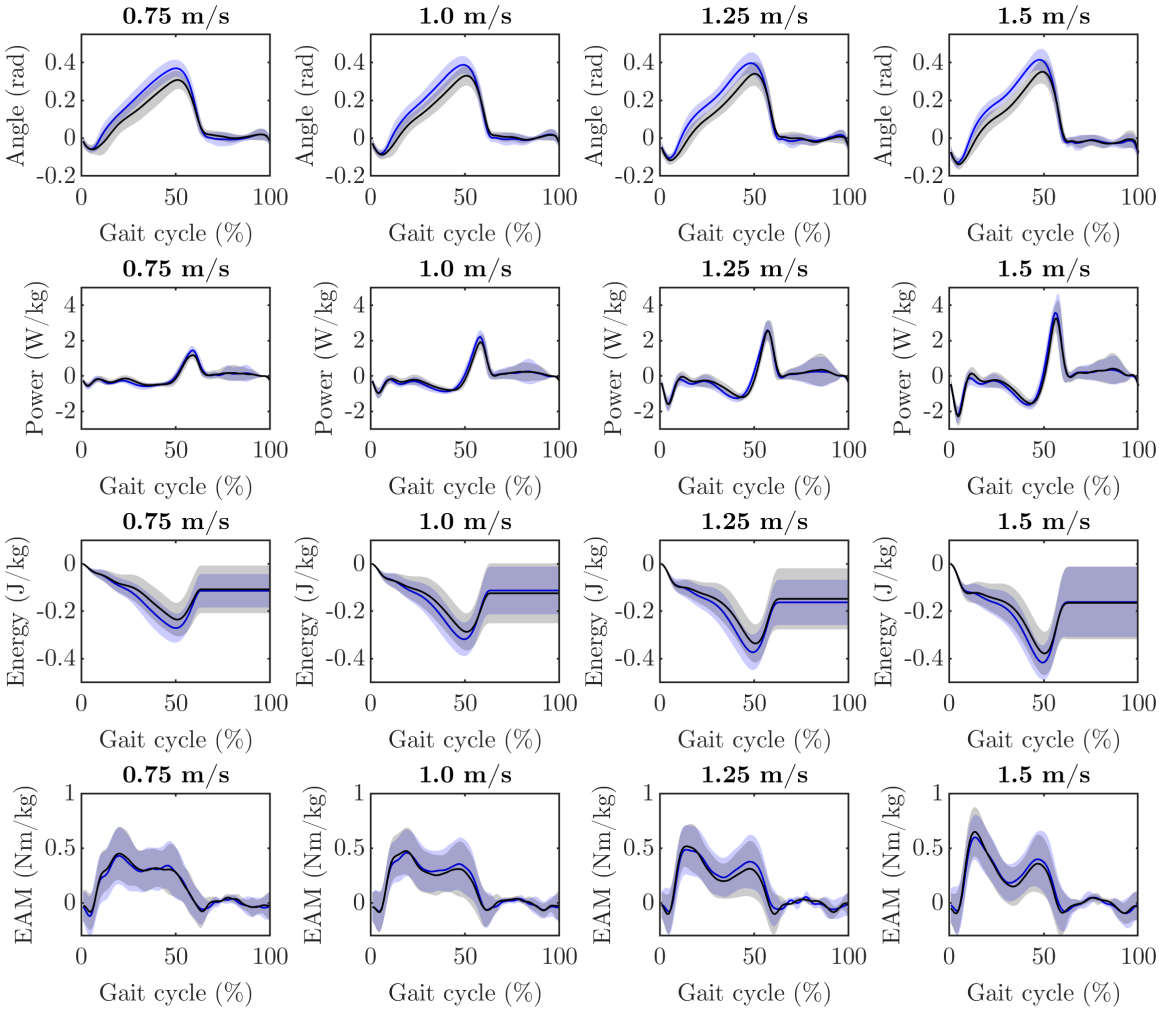

Figure 4-2: **Mean values across gait cycle for all subjects.** Mean joint angle, prosthesis power, contralateral vertical gorund reaction force, and contralateral knee EAM averaged between all subjects for optimal VSA (blue) compared to passive Taleo (black). Mean value is plotted with solid line and ±1 standard deviation is shaded.

Joint angle

There is an increase in maximum joint angle of the prosthesis across speeds for the VSA compared to the passive device. The optimal VSA stiffness at each speed shows an increase in range of motion of 19.3%, 16.8%, 15.5%, and 17.4% at 0.75 m/s, 1.0 m/s, 1.25 m/s, and 1.5 m/s, respectively. The increase in joint angle compared to the passive control is statistically significant (paired t-test, $p<0.05$) at all evaluated walking speeds (0.75 m/s, 1.0 m/s, 1.25 m/s, and 1.5 m/s). Figure 4-3 presents mean peak joint angle for the optimal VSA stiffness compared to the passive ESR device

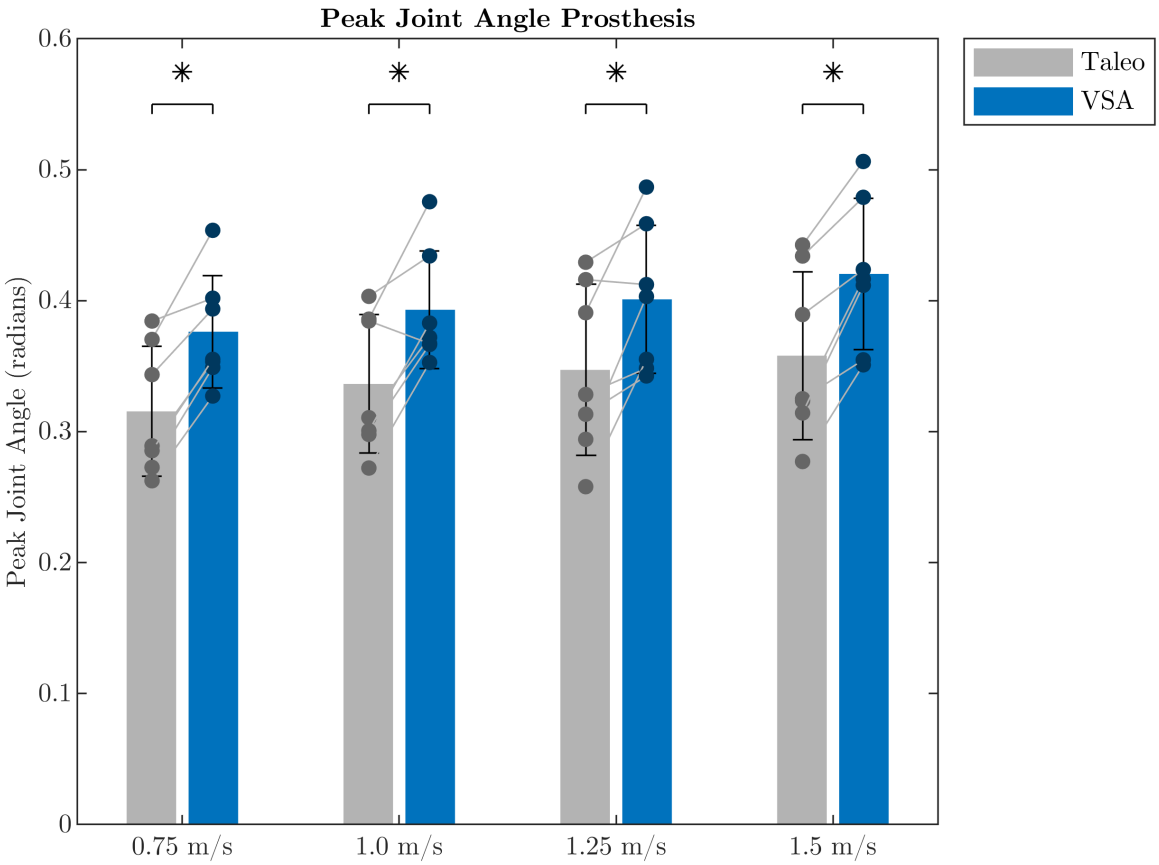

Figure 4-3: **Joint angle.** Peak dorsiflexion angle of the prosthesis during walking for optimal VSA stiffness (blue) compared to Taleo (gray). * indicates statistically significant ($p<0.05$) increase in joint angle.

averaged across the 7 subjects.

Peak ankle power

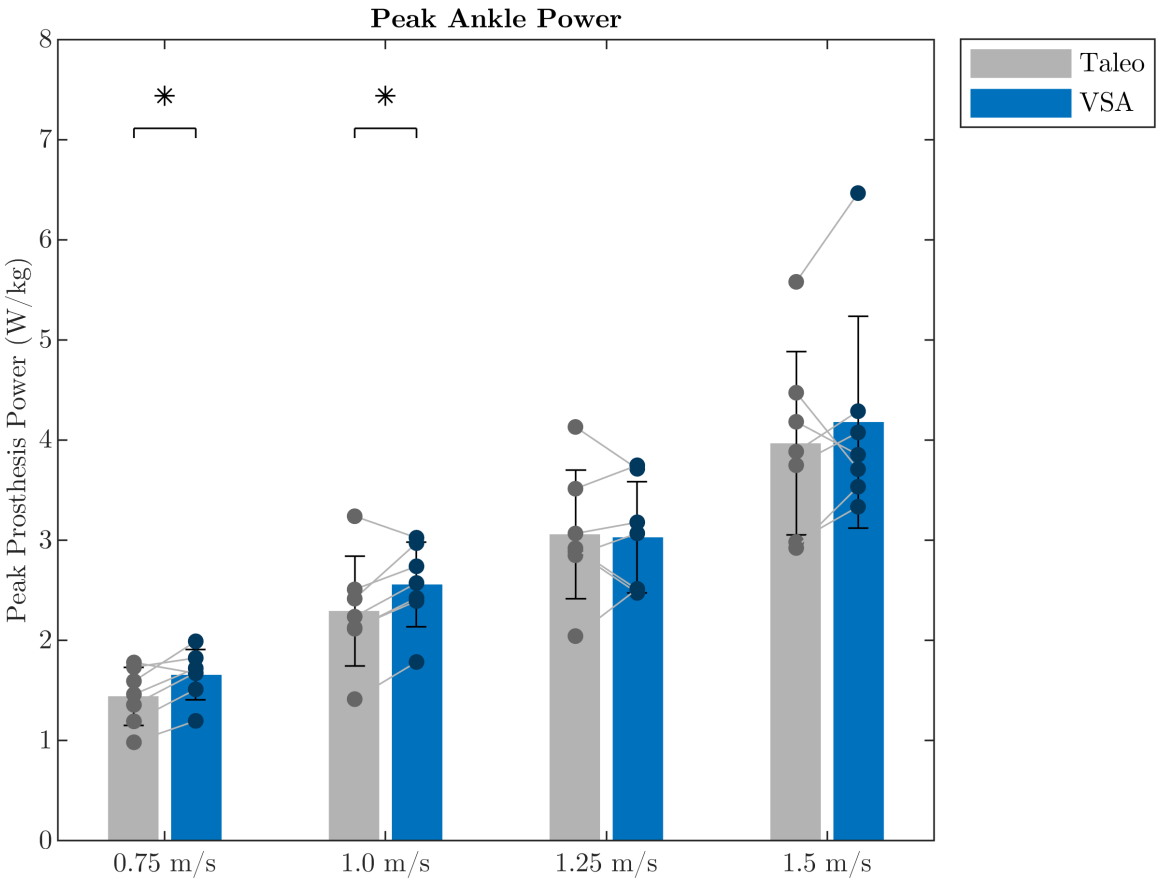

Figure 4-4: **Prosthesis power.** Peak joint power in the prosthetic ankle during walking at the optimal VSA stiffness (blue) compared to the Taleo (gray). * indicates statistically significant ($p<0.05$) increase in joint power.

The VSA optimal stiffness compared to the passive device demonstrates an increase in peak power of 14.8 %, 11.5%, -1.0%, and 5.4% at 0.75 m/s, 1.0 m/s, 1.25 m/s, and 1.5 m/s, respectively. This increase in power is statistically significant (paired t-test, $p<0.05$) at 0.75 m/s and 1.0 m/s. Figure 4-4 presents the mean peak joint power for the optimal VSA stiffness compared to the passive ESR device for the 7 subjects.

Energy return

There is an increase in energy return across speeds for the VSA compared to the passive device. The optimal VSA stiffness at each speed shows an increase in energy

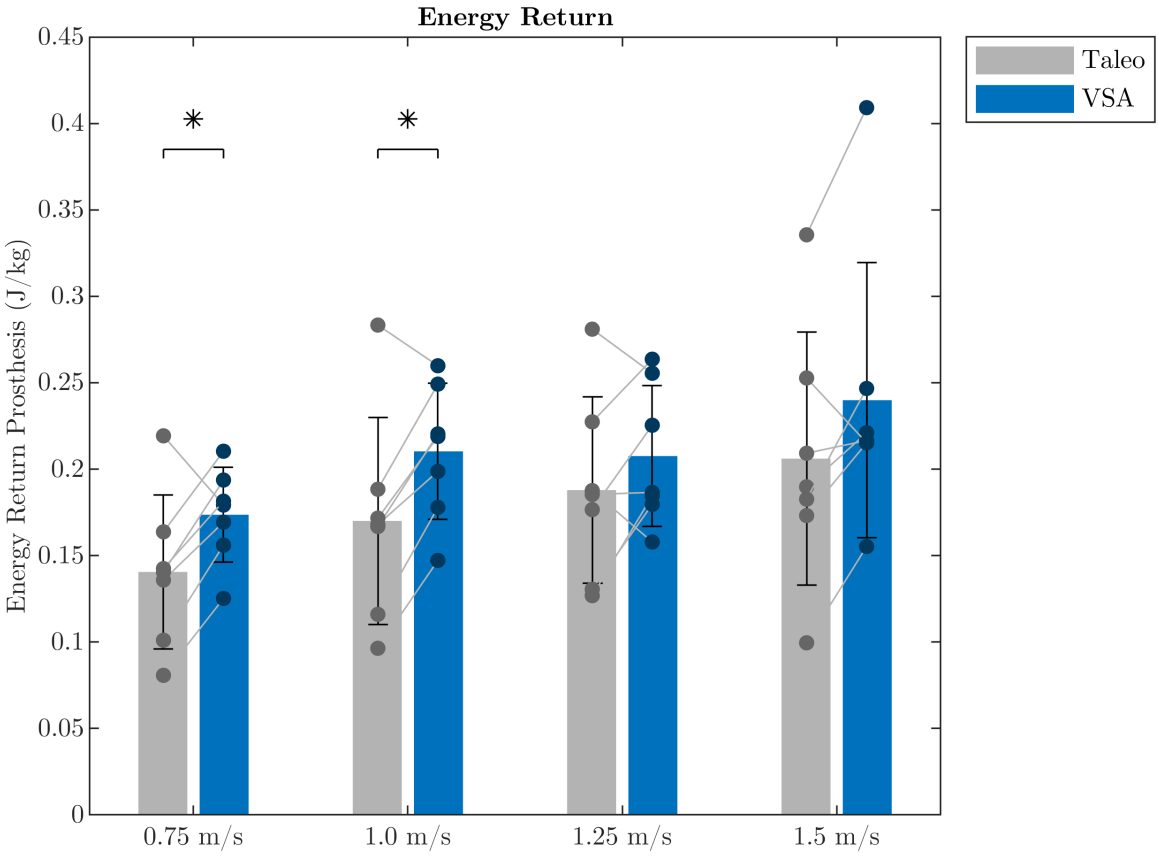

Figure 4-5: **Energy return.** Energy return from the prosthetic ankle during walking at the optimal VSA stiffness (blue) compared to the Taleo (gray). * indicates statistically significant ($p<0.05$) increase in energy return.

return of 23.6%, 23.7%, 10.5%, and 16.4% at 0.75 m/s, 1.0 m/s, 1.25 m/s, and 1.5 m/s, respectively. This increase in energy return is statistically significant (paired t-test, $p<0.05$) at 0.75 m/s and 1.0 m/s. Figure 4-5 presents mean energy return for the optimal VSA stiffness compared to the passive ESR device for the 7 subjects.

Contralateral limb external adduction moment

The results from our pilot study demonstrate a decrease in contralateral limb knee EAM across speeds. The optimal VSA stiffness at each speed shows a decrease in EAM of 6.0%, 5.9%, 4.0%, and 6.7% at 0.75 m/s, 1.0 m/s, 1.25 m/s, and 1.5 m/s, respectively. This decrease is statistically significant (paired t-test, $p<0.05$) at 0.75 m/s, 1.0 m/s, and 1.5 m/s. Figure 4-6 shows the mean value across the 7 subjects of the first peak of contralateral knee EAM of the optimal VSA stiffness compared to

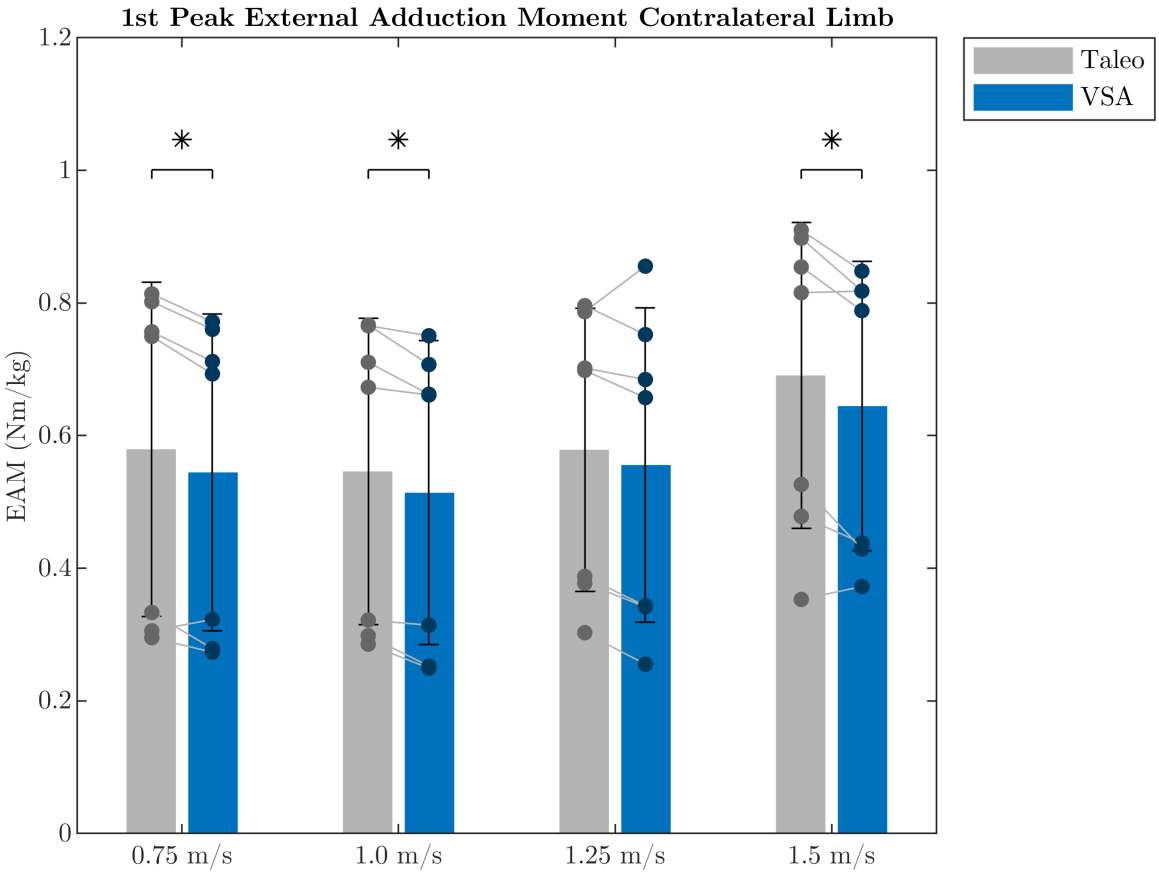

Figure 4-6: **1st Peak EAM contralateral limb.** Peak contralateral knee EAM during walking at the optimal VSA stiffness (blue) compared to the Taleo (gray). * indicates statistically significant ($p<0.05$) decrease in contralateral knee EAM.

the passive device.

Peak vertical ground reaction force contralateral limb

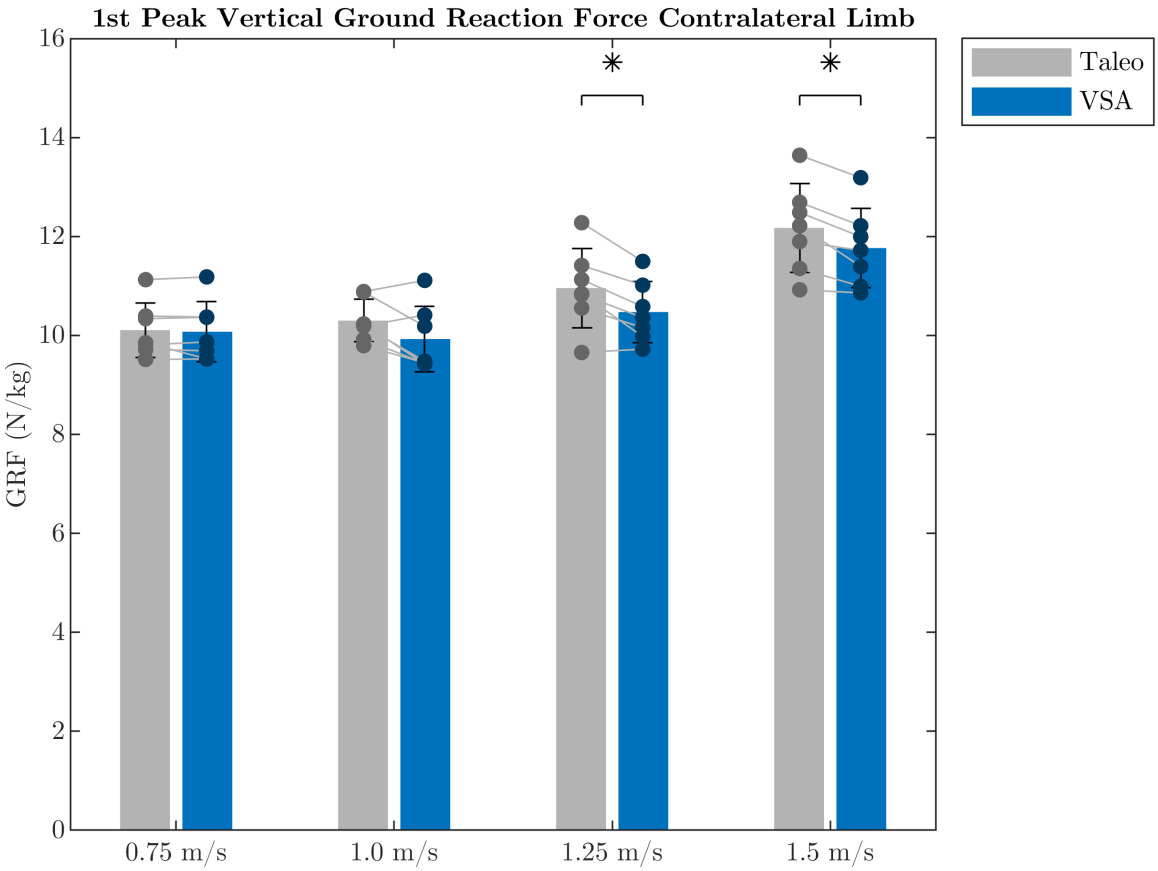

Figure 4-7: **1st peak GRF contralateral limb.** Peak vertical GRF of the contralateral limb during walking at the optimal VSA stiffness (blue) compared to the Taleo (gray). * indicates statistically significant ($p<0.05$) decrease in vertical GRF.

Additionally, there is see a decrease in the vertical ground reaction force of the contralateral limb during step transitions across walking speeds. The average 1st peak of the contralateral ground reaction force across the 7 subjects is decreased by 0.3%, 3.6 %, 4.4 %, 3.3% for 0.75 m/s m/s, 1.0 m/s, 1.25 m/s, and 1.5 m/s, respectively. This decrease is statistically significant (paired t-test, $p<0.05$) at 1.25 m/s and 1.5 m/s. Figure 4-7 shows the mean value across the 7 subjects of the first peak of contralateral leg vertical GRF of the optimal VSA stiffness compared to the passive device.

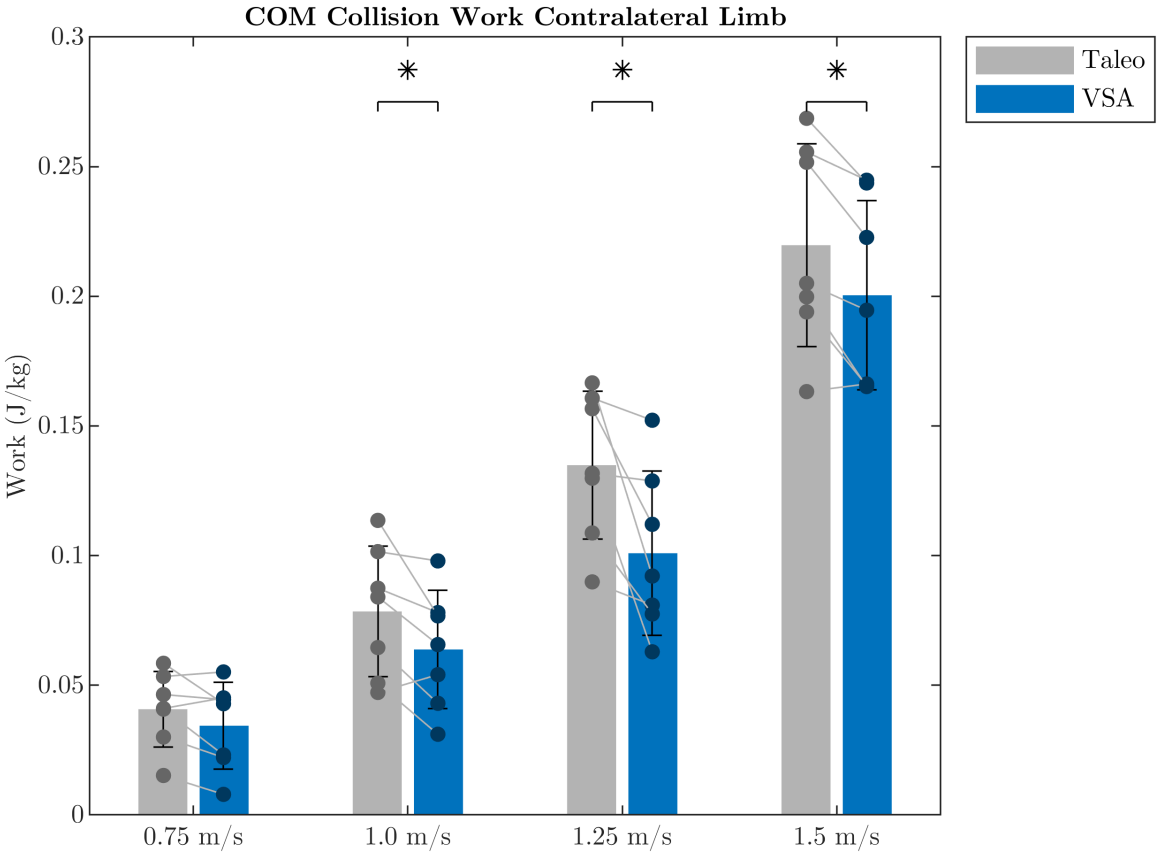

Figure 4-8: **COM collision work.** Center of mass collision work by the contralateral limb during step transition while walking at the optimal VSA stiffness (blue) compared to the Taleo (gray). * indicates statistically significant ($p<0.05$) decrease in COM collision work.

Center of mass collision work

Center of mass collision work, another metric of the impact on the contralateral limb during step transitions, is decreased for all speeds. There is a decrease of 15.6%, 18.7%, 25.2%, and 8.8% at 0.75 m/s m/s, 1.0 m/s, 1.25 m/s, and 1.5 m/s, respectively. This decrease is statistically significant (paired t-test, $p<0.05$) at 1.0 m/s, 1.25 m/s, and 1.5 m/s. Figure 4-8 shows the mean value across the 7 subjects of the center of mass collision work for the optimal VSA stiffness compared to the passive device.

Center of mass push-off work

Center of mass push-off work from the trailing limb (prosthesis side) increases across all speeds with the optimal VSA compared to the Taleo. There is an increase in total

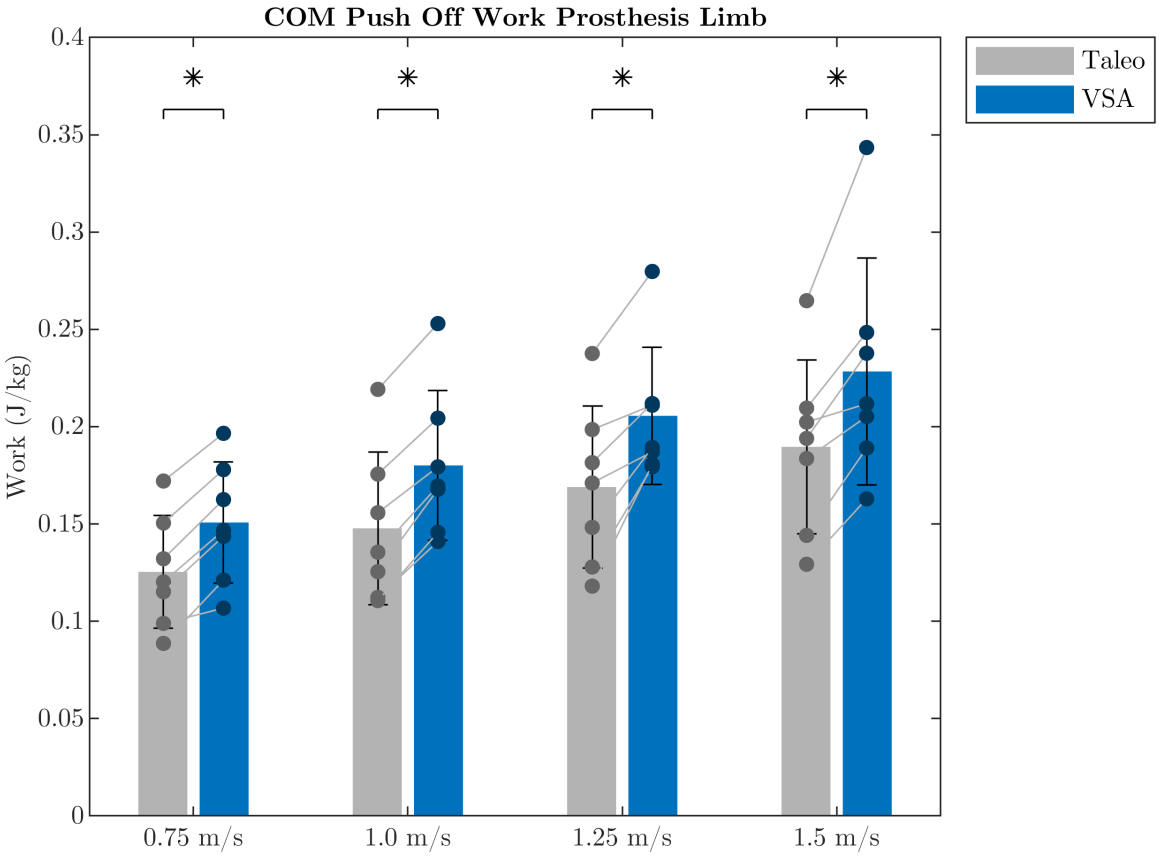

Figure 4-9: **COM push off work.** Push off work on the center of mass by the prosthesis limb during walking with the optimal VSA stiffness (blue) compared to the Taleo (gray). * indicates statistically significant ($p<0.05$) increase in COM push off work.

push-off work of 20.2 %, 21.9%, 21.7%, and 20.4% at 0.75 m/s m/s, 1.0 m/s, 1.25 m/s, and 1.5 m/s, respectively. This change is statistically significant (paired t-test, $p<0.05$) at all speeds (0.75 m/s, 1.0 m/s, 1.25 m/s, and 1.5 m/s). Figure 4-9 shows the mean value between the 7 subjects of the center of mass push-off work for the optimal VSA stiffness compared to the passive device.

4.2.2 User Preference

User preference was also recorded during the study. 4.3

Table 4.3: Stiffness preference.

		S1	S2	S3	S4	S5	S6	S7
0.75 m/s	Optimal	1	4	1	2	1	1	1
	Preference	2	3	5	2	4	4	4
1.0 m/s	Optimal	2	5	1	3	1	1	1
	Preference	2	4	4	4	4	3	3
1.25 m/s	Optimal	5	4	1	5	3	2	3
	Preference	3	5	3	4	5	5	5
1.5 m/s	Optimal	3	1	2	4	6	1	1
	Preference	4	4	2	4	6	5	5

4.2.3 Gait Symmetry

We see an improvement in gait symmetry at the knee across speeds. Figure 4-10, Figure 4-11, and Figure 4-12 show prosthesis side and contralateral limb joint angles across gait cycle while walking with the optimal VSA compared to the Taleo. We see a slight increase in agreement between prosthesis side and contralateral limb knee angles with the VSA compared to the Taleo (Figure 4-11), as determined by the R^2 values, though this difference is not statistically significant. The correlation coefficient values between prosthesis side knee angle and contralateral knee angle for each walking speed are shown in Table 4.4.

Table 4.4: Gait symmetry.

	0.75 m/s	**1.0 m/s**	**1.25 m/s**	**1.5 m/s**
VSA	0.97	0.98	0.97	0.95
Taleo	0.96	0.97	0.95	0.95

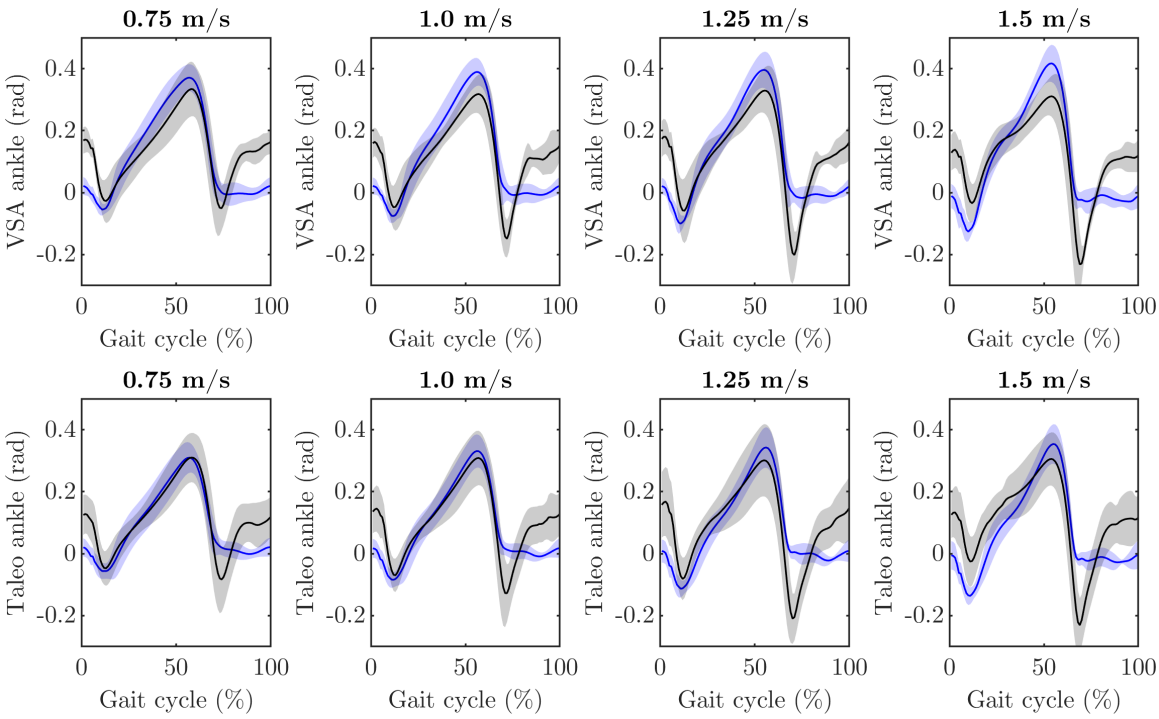

Figure 4-10: **Ankle joint angles prosthesis side compared to contralateral side.** Mean ankle joint angles across subjects of prosthesis side (blue) and contralateral side (gray) while walking with the VSA (top row) compared to the Taleo (bottom row). Shaded regions show ± 1 standard deviation above and below mean.

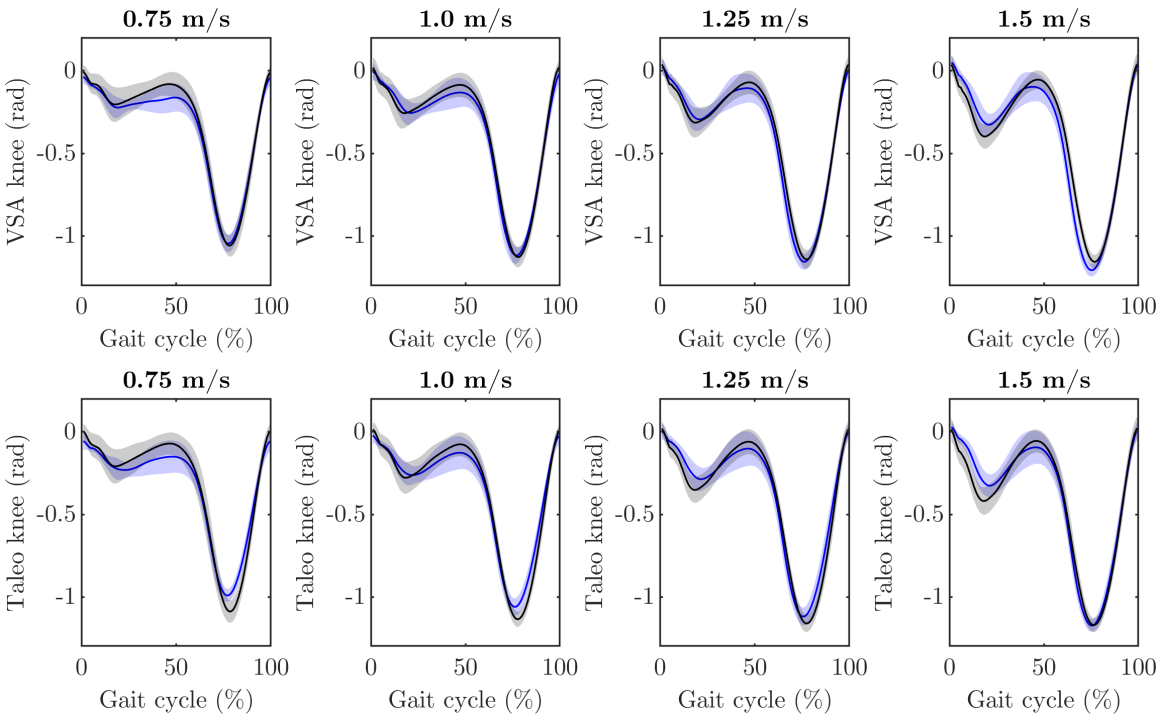

Figure 4-11: **Knee flexion angles prosthesis side compared to contralateral side.** Mean knee flexion angles across subjects of prosthesis side (blue) and contralateral side (gray) while walking with the VSA (top row) compared to the Taleo (bottom row). Shaded regions show ±1 standard deviation above and below mean.

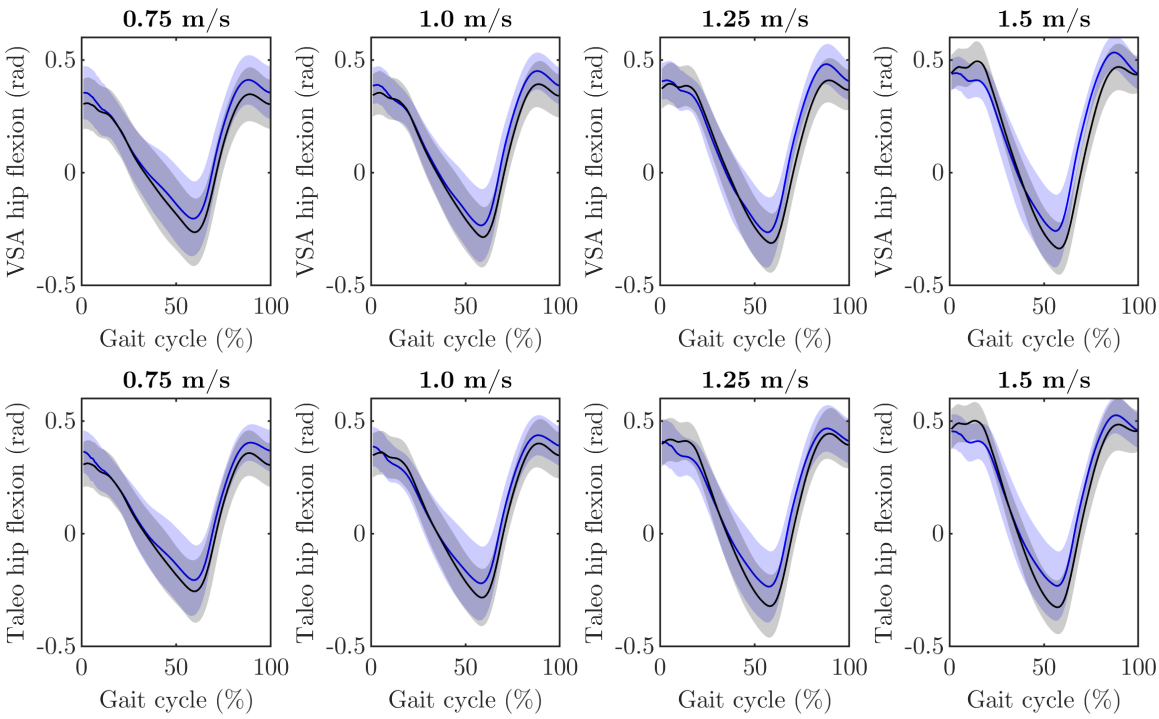

Figure 4-12: **Hip flexion angles prosthesis side compared to contralateral side.** Mean hip flexion angles across subjects of prosthesis side (blue) and contralateral side (gray) while walking with the VSA (top row) compared to the Taleo (bottom row). Shaded regions show ±1 standard deviation above and below mean.

4.2.4 Comparison to Biological Kinematics

I analyze joint angles of the ankle, knee, and hip compared to a reference dataset of biological joint angles while walking across speeds [32]. Figure 4-13, Figure 4-14, and Figure 4-15 show prosthesis side joint angles and contralateral side for the VSA and Taleo. Dashed lines indicate ±1 standard deviation typical joint angles from a reference dataset of healthy people with intact biological limbs [32].

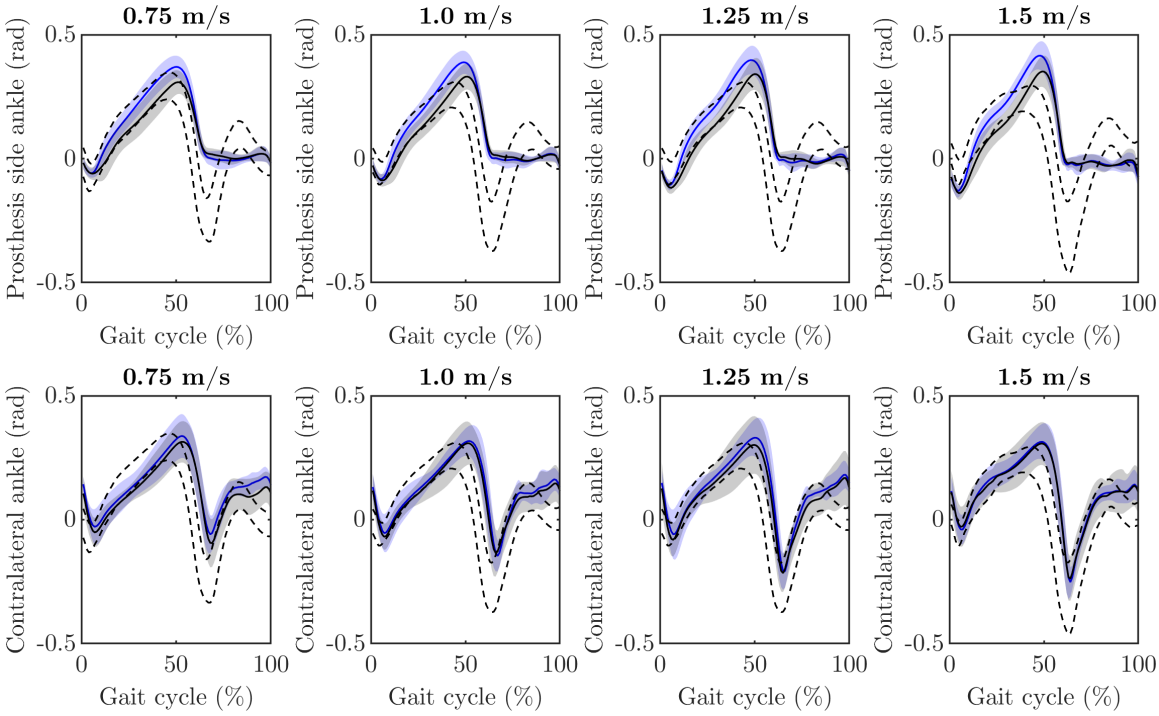

Figure 4-13: **Ankle joint angles compared to reference dataset.** Prosthesis side joint angles (top row) for VSA (blue) and Taleo (gray), dashed lines represent mean ±1 standard deviation of typical joint angles for each walking speed. Reference data from [32].

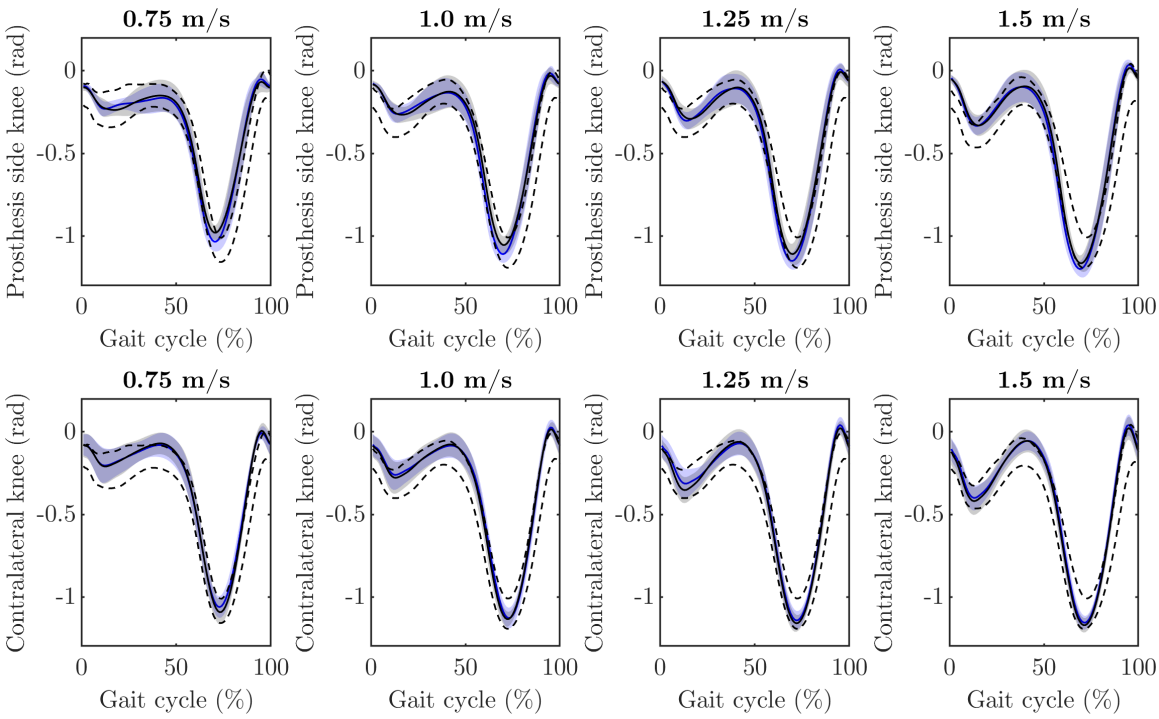

Figure 4-14: **Knee flexion angles compared to reference dataset.** Prosthesis side joint angles (top row) for VSA (blue) and Taleo (gray), dashed lines represent mean ±1 standard deviation of typical joint angles for each walking speed. Reference data from [32].

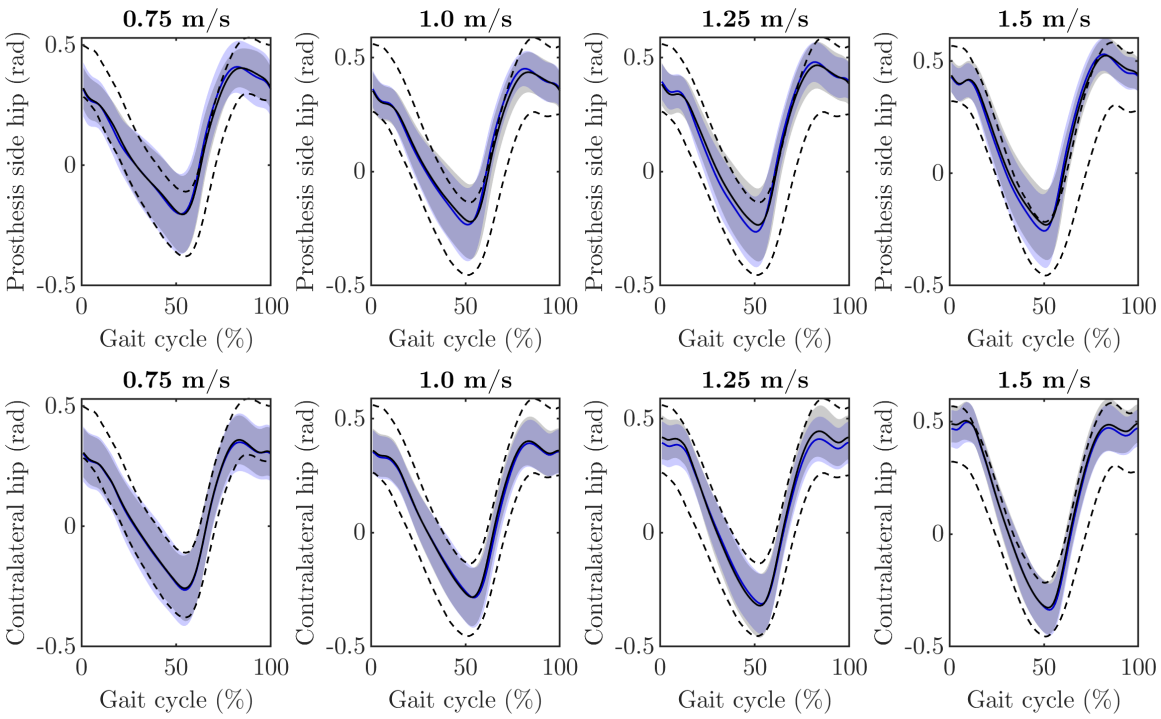

Figure 4-15: **Hip flexion angles compared to reference dataset.** Prosthesis side joint angles (top row) for VSA (blue) and Taleo (gray), dashed lines represent mean ± 1 standard deviation of typical joint angles for each walking speed. Reference data from [32].

4.2.5 Comparison to Powered Prosthesis

I also analyze the external adduction moment and peak vertical ground reaction force with the VSA compared to walking data with powered prosthesis and compared to biological levels reported in the literaure [41]. Table 4.5 presents vertical ground reaction force data while walking at a range of speeds for biological controls, people walking with powered prostheses, and passive devices from [41], as well as the passive and VSA data from the present study. Table 4.6.

Table 4.5: 1st Peak contralateral limb vertical GRF (N/kg).

Speed	**Data from [41]**				**Current study**		
(m/s)	Control	Passive	Powered	%Δ	Passive	VSA	%Δ
0.75	9.79 ±0.27	9.97 ±0.21	9.76 ±0.13	-2.1%	10.11 ±0.55	10.08 ±0.61	-0.3%
1.0	9.86 ±0.37	10.39 ±0.40	9.75 ±0.22	-6.2%	10.30 ±0.43	9.93 ±0.66	-3.6%
1.25	10.62 ±0.39	11.33 ±0.67	10.52 ±0.75	-7.2%	10.96 ±0.80	10.47 ±0.62	-4.4%
1.5	11.58 ±0.75	12.77 ±1.10	11.41 ±1.28	-10.7%	12.17 ±0.90	11.77 ±0.80	-3.3%

Table 4.6: 1st Peak contralateral limb knee EAM (Nm/kg).

Speed	**Data from [41]**				**Current study**		
(m/s)	Control	Passive	Powered	%Δ	Passive	VSA	%Δ
0.75	0.39 ±0.13	0.41 ±0.13	0.39 ±0.08	-5.1%	0.58 ±0.25	0.54 ±0.24	-6.0%
1.0	0.34 ±0.14	0.42 ±0.12	0.42 ±0.09	-0.8%	0.55 ±0.23	0.51 ±0.23	-5.9%
1.25	0.38 ±0.11	0.50 ±0.14	0.47 ±0.10	-5.5%	0.58 ±0.21	0.56 ±0.24	-4.0%
1.5	0.44 ±0.14	0.61 ±0.16	0.49 ±0.06	-20.6%	0.69 ±0.23	0.64 ±0.22	-6.7%

4.3 Individual Subject Results

This section presents the results for each subject. Figures 4-16 - 4-42 plot joint angles of the ankle, knee, and hip, plot dorsiflexion angle, power, vertical GRF, and contralateral EAM across gait cycle, and plot metrics of interest for each stiffness compared to the passive ESR control foot at each speed.

4.3.1 Subject 1

Results from Subject 1 are shown in Figure 4-16, Figure 4-17, and Figure 4-18. Figure 4-16 plots prosthesis side and contralateral side joint angles for the ankle, knee, and hip while walking with the VSA and the Taleo across speeds. Figure 4-17 shows joint angle, prosthesis power, contralateral vertical GRF, and contralateral knee EAM for each evaluated walking speed. Figure 4-18 shows mean values of maximum dorsiflexion angle, peak power, energy return, contralateral knee EAM, center of mass collision work, and center of mass push-off work for each evaluated VSA stiffness and the Taleo for each walking speed.

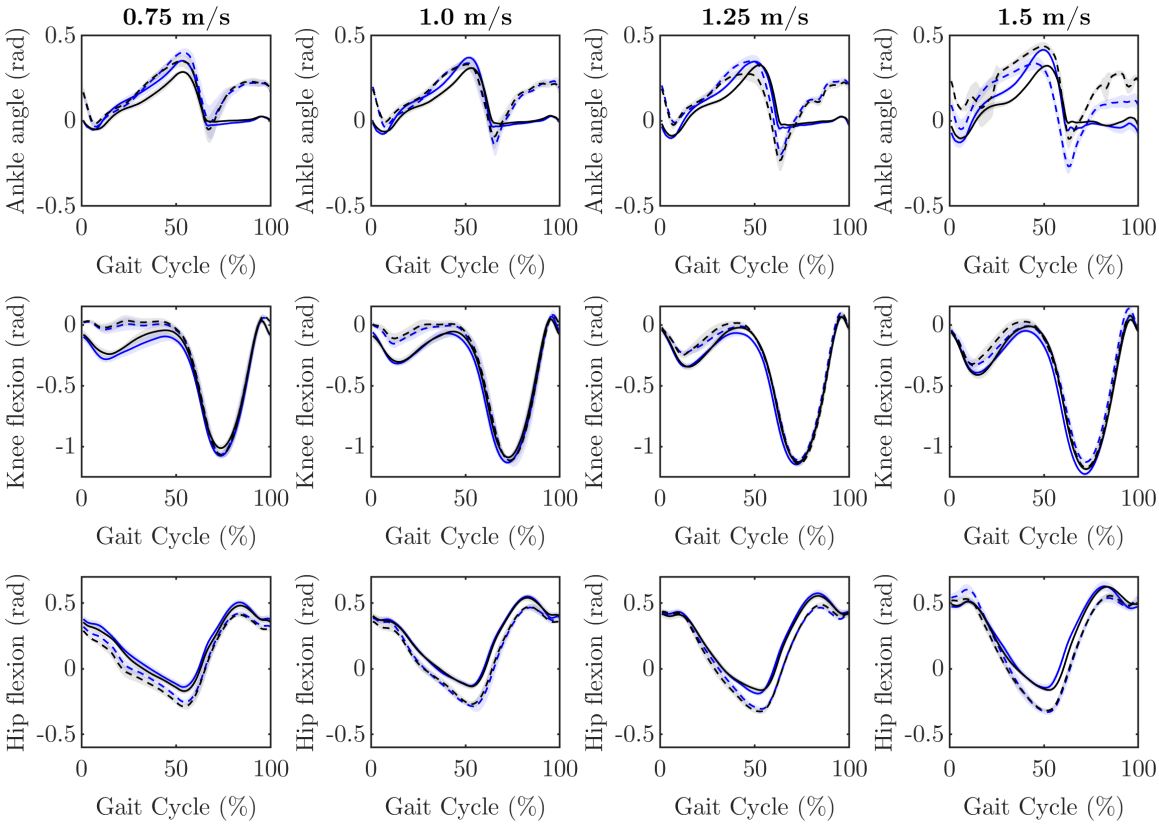

Figure 4-16: **Subject 1 joint angles.** Data is plotted for ankle angle, knee angle, and hip flexion across gait cycle for each speed, for VSA joint angles (blue), VSA contralateral limb (blue dashed), Taleo joint angles (gray), and Taleo contralateral limb (gray dashed).

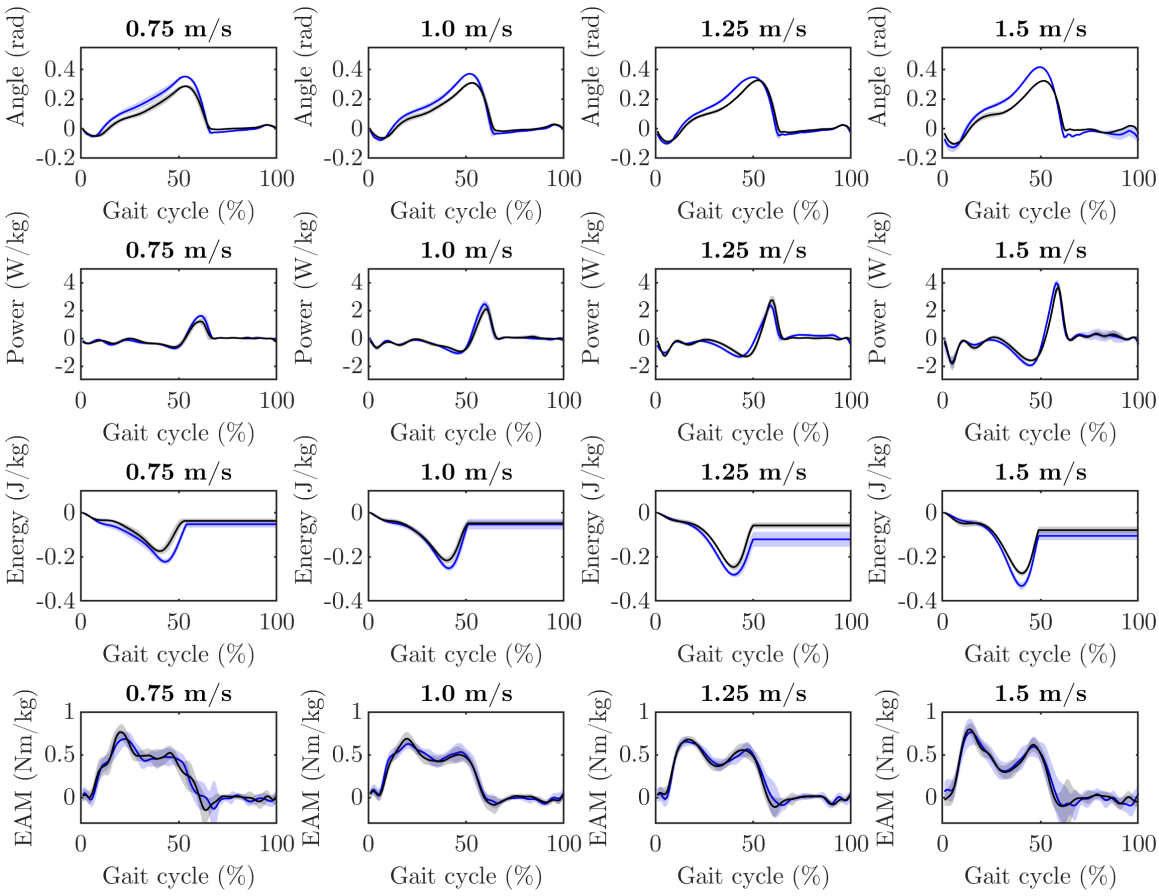

Figure 4-17: **Subject 1 joint angle, power, GRF, and EAM.** Data from optimal VSA (blue) and Taleo (gray) across gait cycle for each walking speed. Plots show dorsiflexion angle, prosthesis power, contralateral vertical GRF, and contralateral knee EAM.

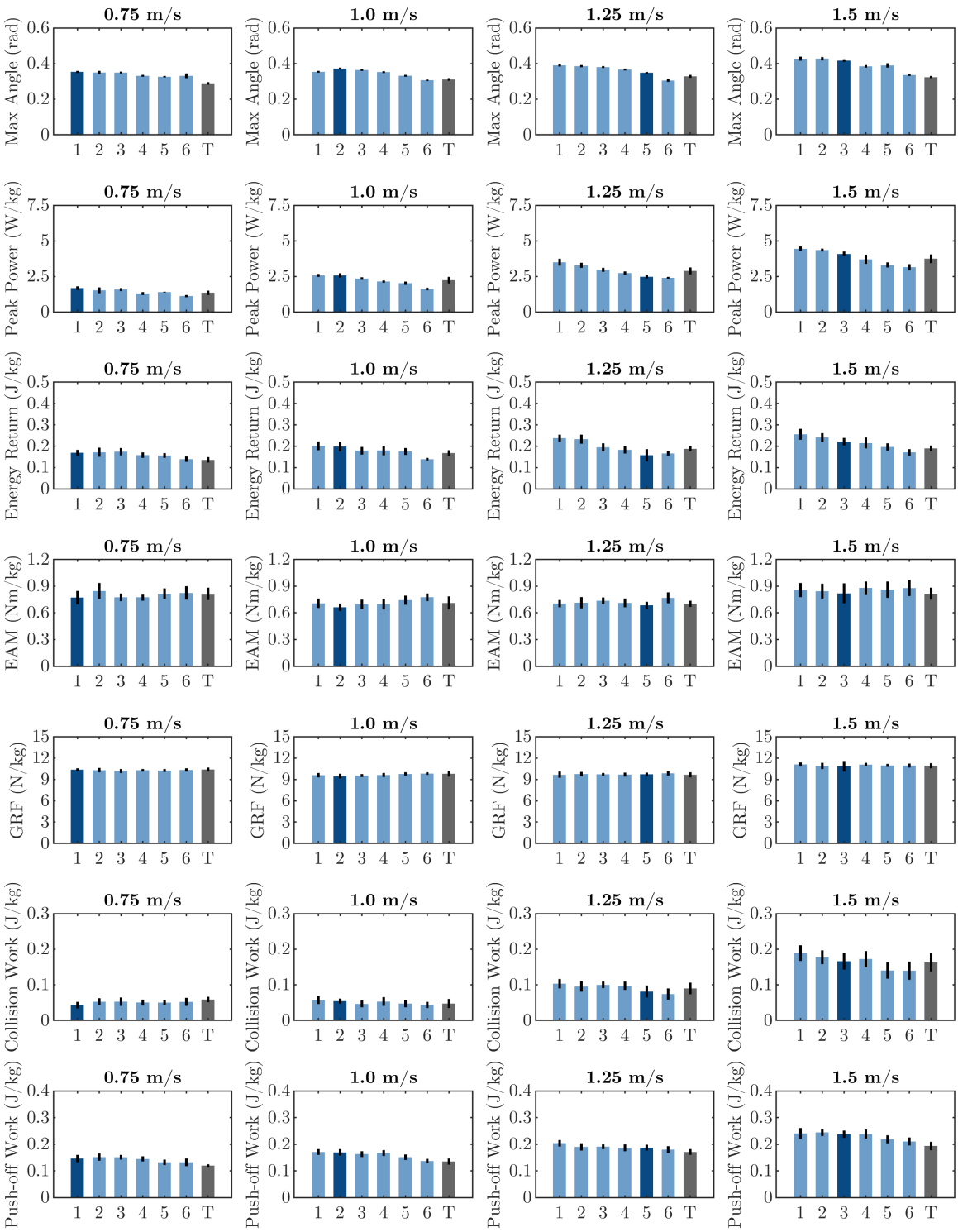

Figure 4-18: **Subject 1 results.** Results across speeds for all evaluated VSA stiffnesses (blue) compared to Taleo (gray): maximum dorsiflexion angle, peak power, energy return, contralateral knee EAM, COM collision work, and COM push-off work. Optimal VSA stiffness is highlighted (dark blue). Error bars represent ±1 standard deviation.

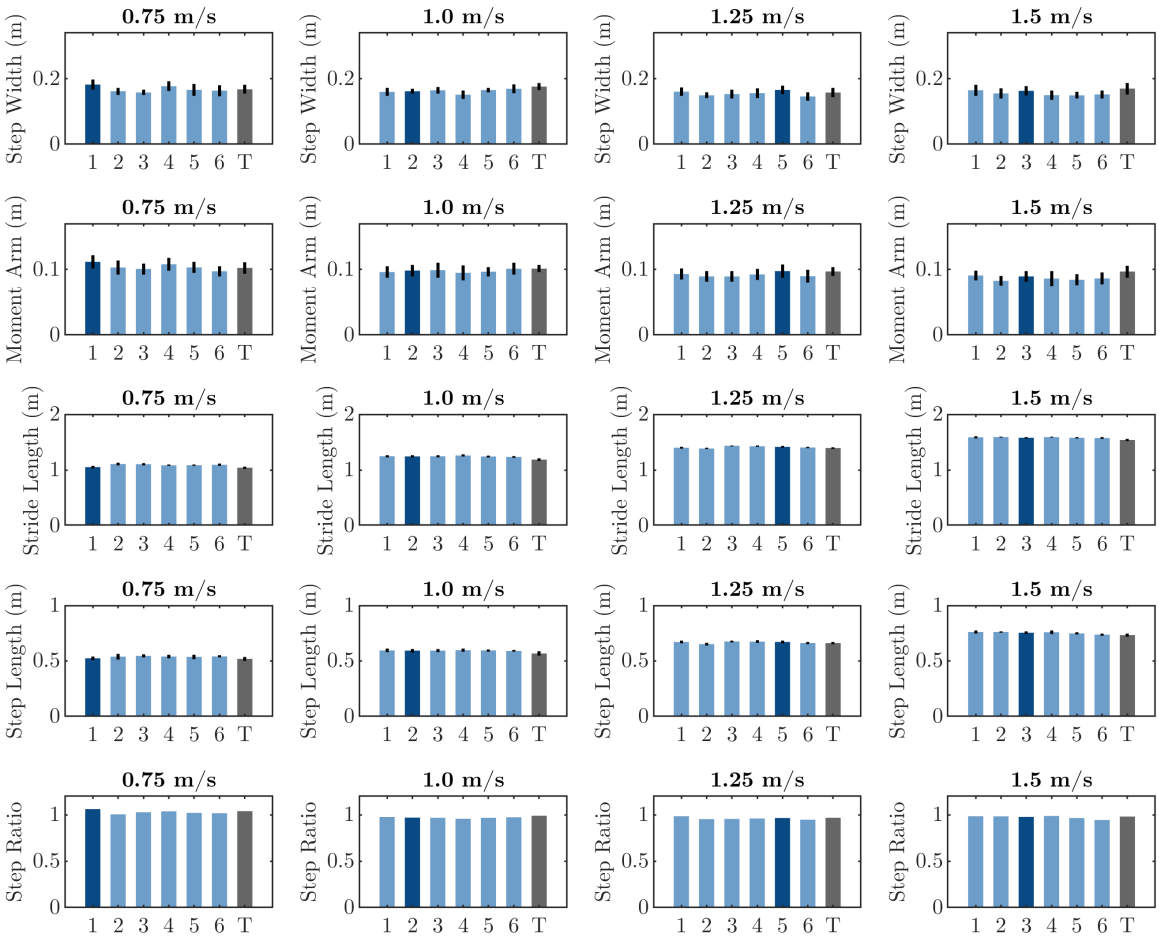

Figure 4-19: **Subject 1 gait parameters.** Gait parameters across speeds for all evaluated VSA stiffnesses (blue) compared to Taleo (gray): step width, knee EAM moment arm, stride length, step length, and step length ratio. Optimal VSA stiffness is highlighted (dark blue). Error bars represent ±1 standard deviation.

4.3.2 Subject 2

Results from Subject 2 are shown in Figure 4-20, Figure 4-21, and Figure 4-22. Figure 4-20 plots prosthesis side and contralateral side joint angles for the ankle, knee, and hip while walking with the VSA and the Taleo across speeds. Figure 4-21 shows joint angle, prosthesis power, contralateral vertical GRF, and contralateral knee EAM for each evaluated walking speed. Figure 4-22 shows mean values of maximum dorsiflexion angle, peak power, energy return, contralateral knee EAM, center of mass collision work, and center of mass push-off work for each evaluated VSA stiffness and the Taleo for each walking speed.

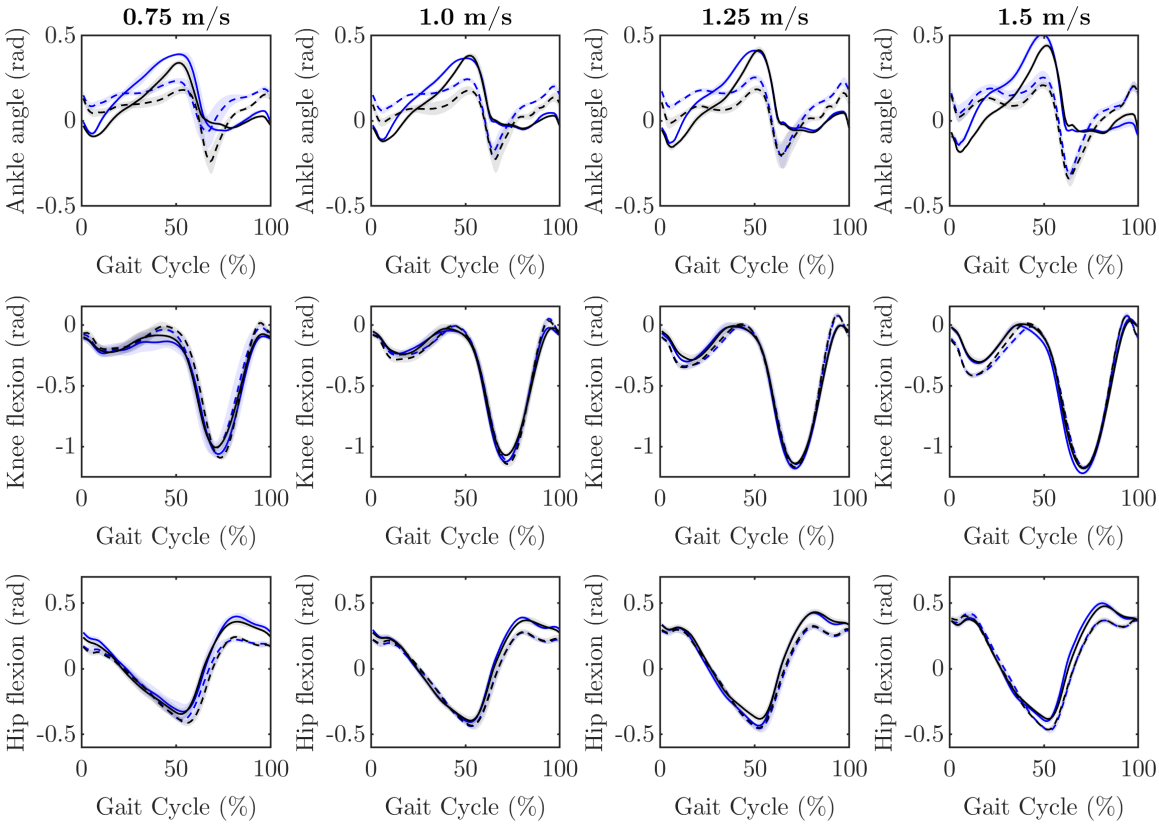

Figure 4-20: **Subject 2 joint angles.** Data is plotted for ankle angle, knee angle, and hip flexion across gait cycle for each speed, for VSA joint angles (blue), VSA contralateral limb (blue dashed), Taleo joint angles (gray), and Taleo contralateral limb (gray dashed).

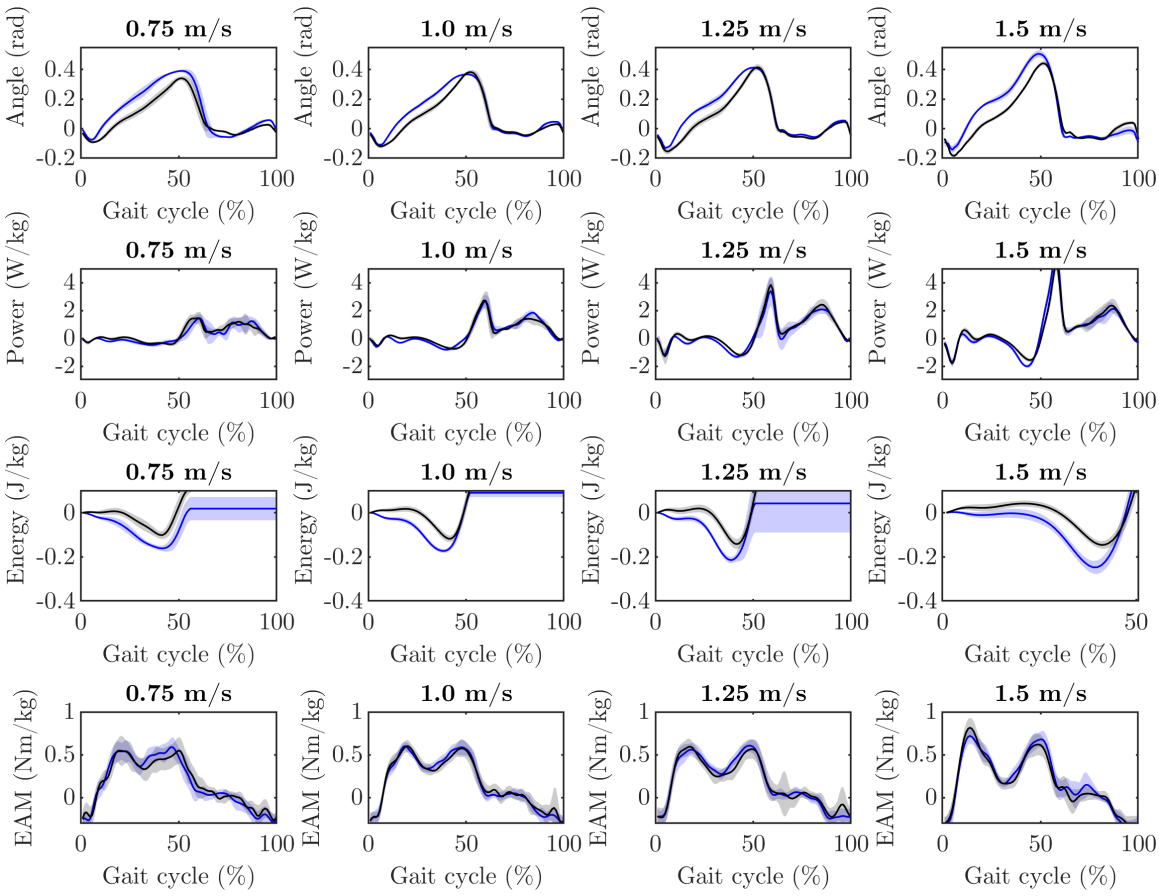

Figure 4-21: **Subject 2 joint angle, power, GRF, and EAM.** Data from optimal VSA (blue) and Taleo (gray) across gait cycle for each walking speed. Plots show dorsiflexion angle, prosthesis power, contralateral vertical GRF, and contralateral knee EAM.

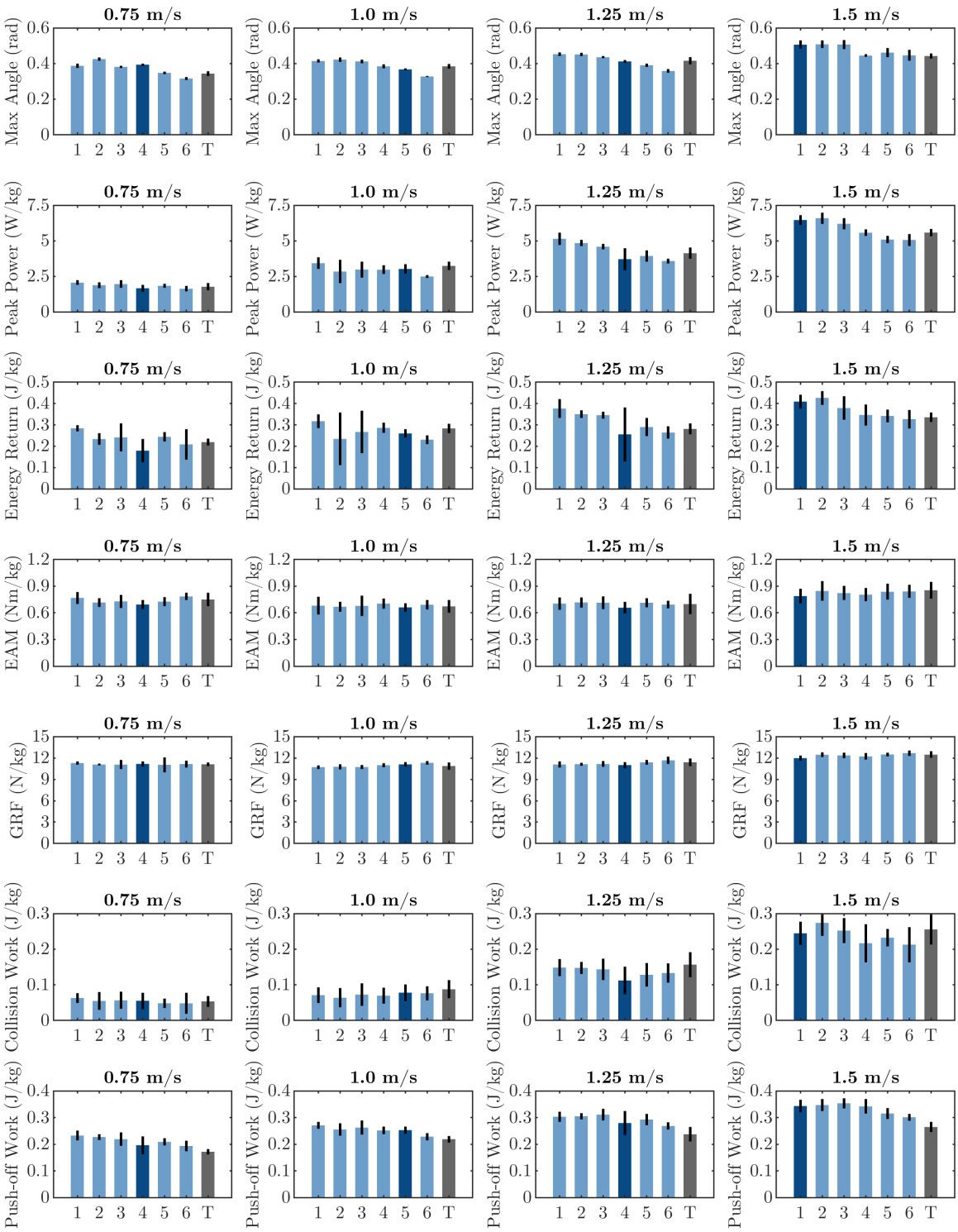

Figure 4-22: **Subject 2 results.** Results across speeds for all evaluated VSA stiffnesses (blue) compared to Taleo (gray): maximum dorsiflexion angle, peak power, energy return, contralateral knee EAM, COM collision work, and COM push-off work. Optimal VSA stiffness is highlighted (dark blue). Error bars represent ±1 standard deviation.

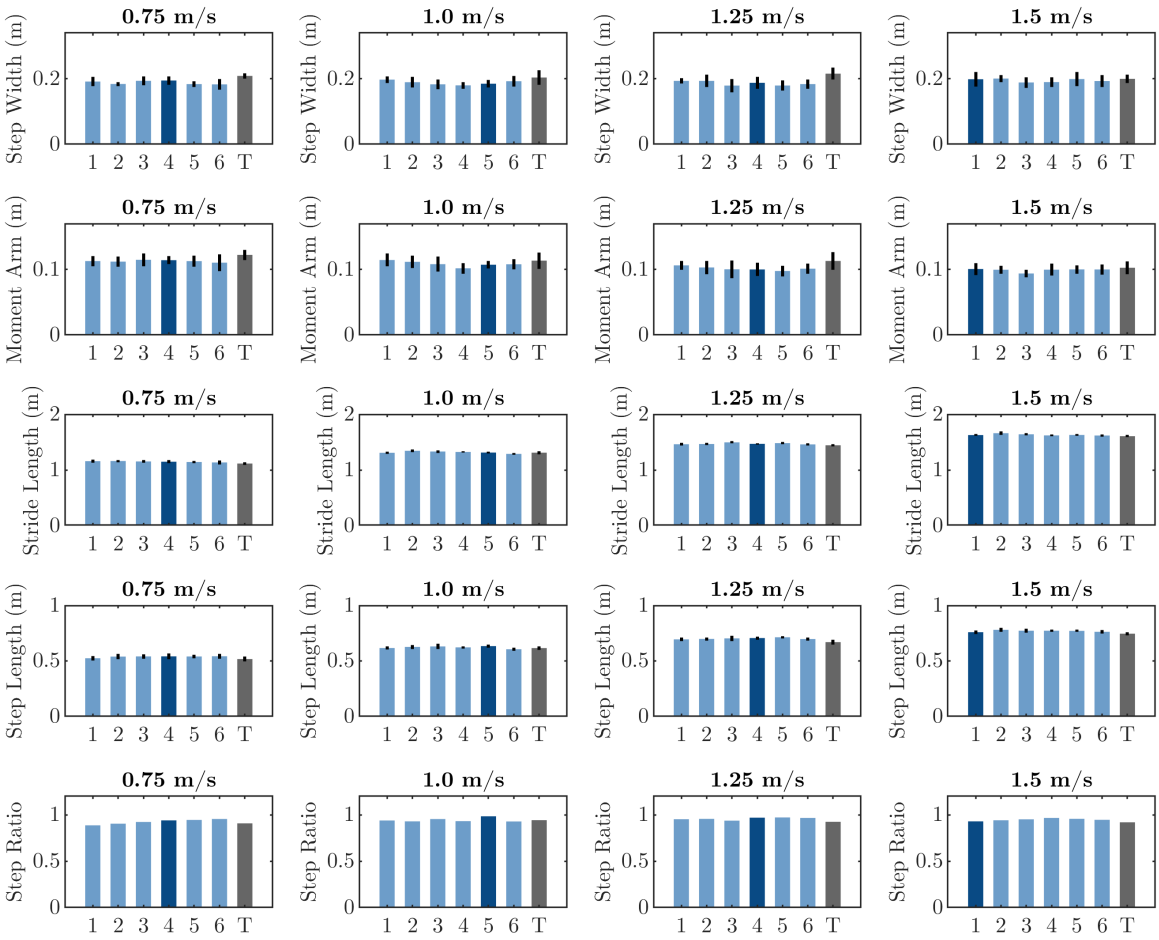

Figure 4-23: **Subject 2 gait parameters.** Gait parameters across speeds for all evaluated VSA stiffnesses (blue) compared to Taleo (gray): step width, knee EAM moment arm, stride length, step length, and step length ratio. Optimal VSA stiffness is highlighted (dark blue). Error bars represent ±1 standard deviation.

4.3.3 Subject 3

Results from Subject 3 are shown in Figure 4-24, Figure 4-25, and Figure 4-26. Figure 4-24 plots prosthesis side and contralateral side joint angles for the ankle, knee, and hip while walking with the VSA and the Taleo across speeds. Figure 4-25 shows joint angle, prosthesis power, contralateral vertical GRF, and contralateral knee EAM for each evaluated walking speed. Figure 4-26 shows mean values of maximum dorsiflexion angle, peak power, energy return, contralateral knee EAM, center of mass collision work, and center of mass push-off work for each evaluated VSA stiffness and the Taleo for each walking speed.

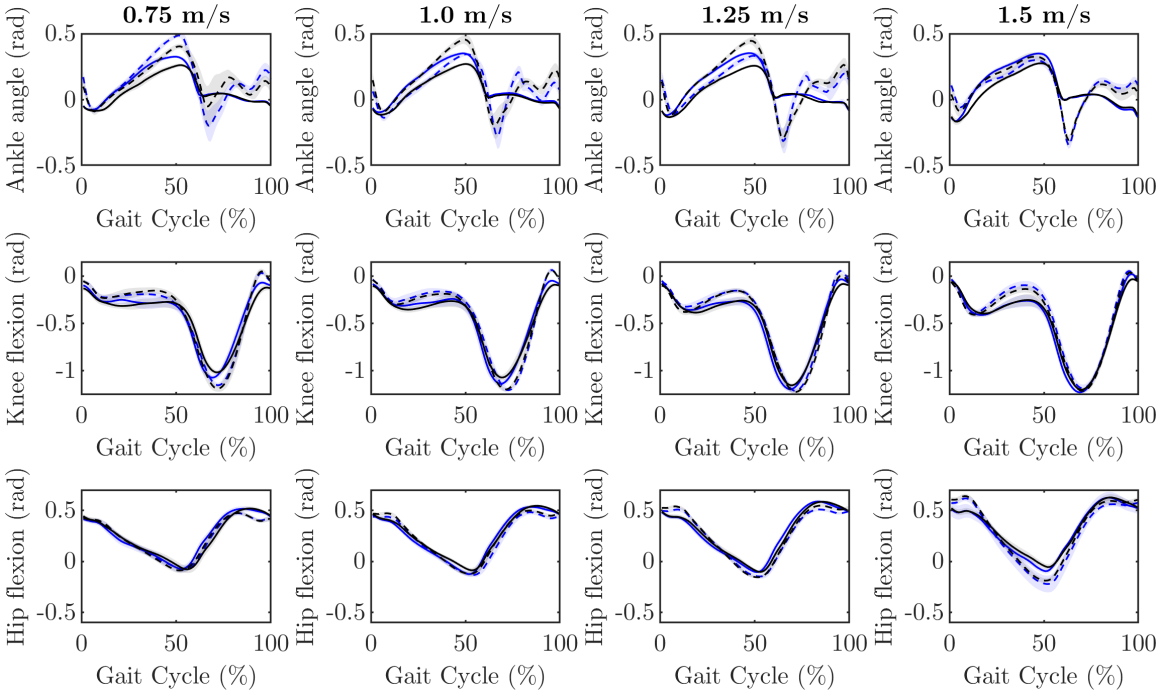

Figure 4-24: **Subject 3 joint angles.** Data is plotted for ankle angle, knee angle, and hip flexion across gait cycle for each speed, for VSA joint angles (blue), VSA contralateral limb (blue dashed), Taleo joint angles (gray), and Taleo contralateral limb (gray dashed).

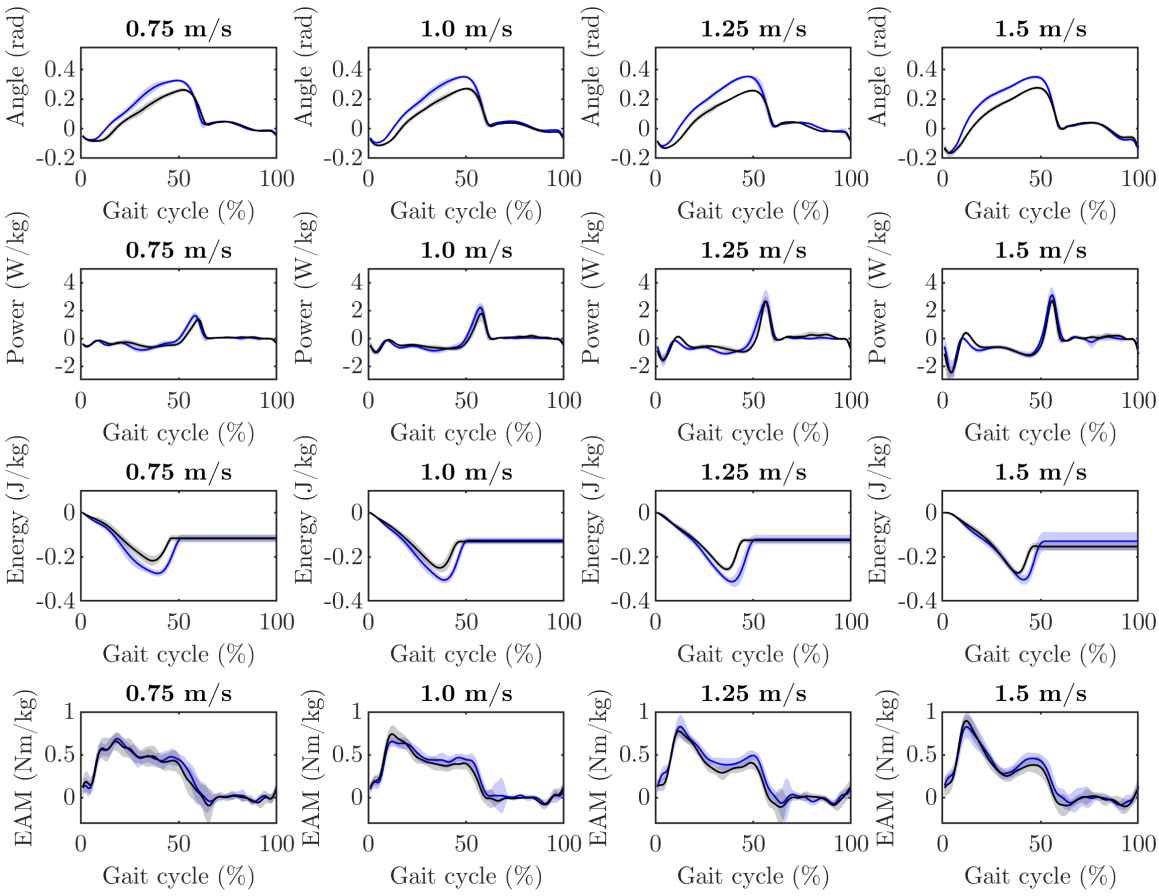

Figure 4-25: **Subject 3 joint angle, power, GRF, and EAM.** Data from optimal VSA (blue) and Taleo (gray) across gait cycle for each walking speed. Plots show dorsiflexion angle, prosthesis power, contralateral vertical GRF, and contralateral knee EAM.

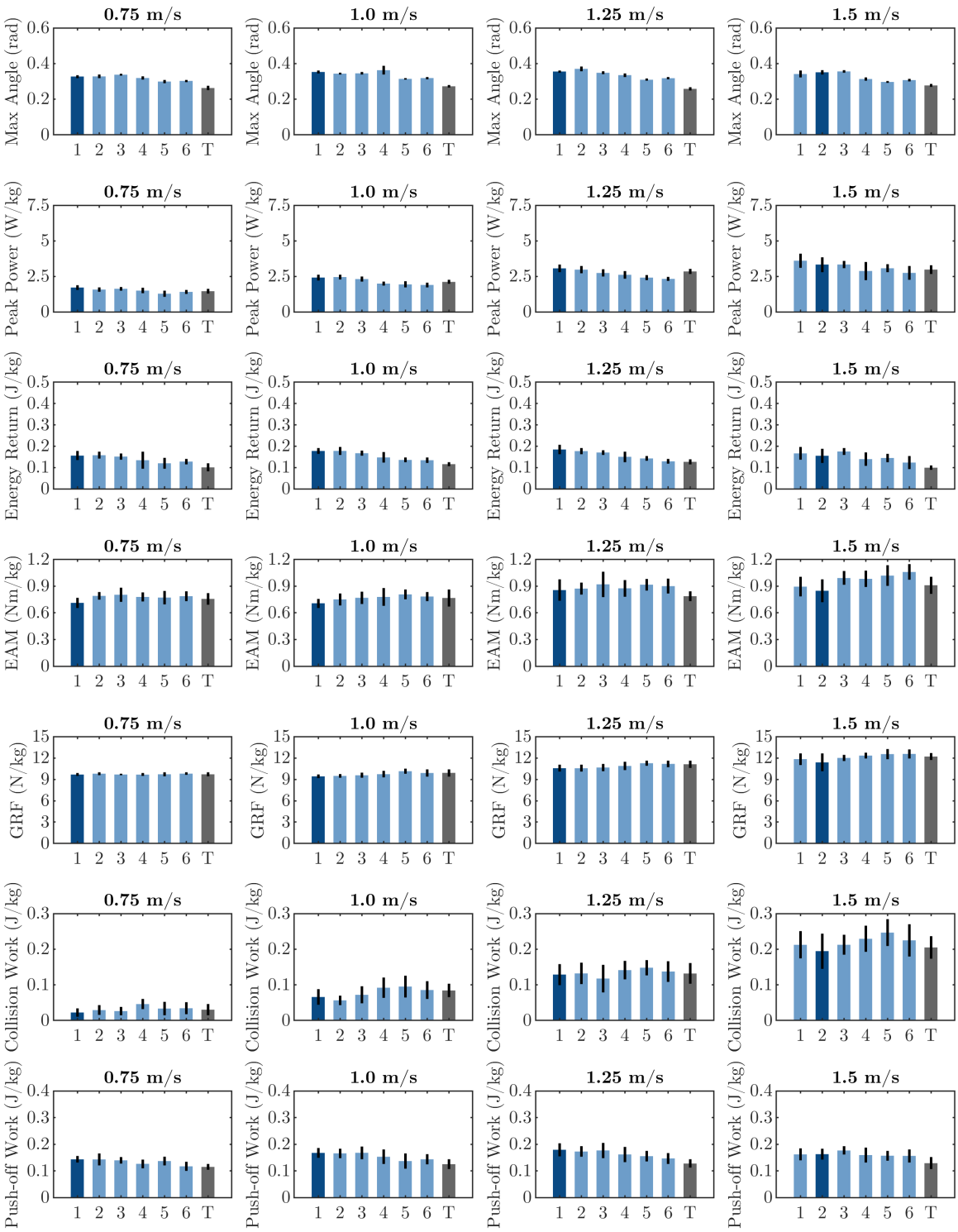

Figure 4-26: **Subject 3 results.** Results across speeds for all evaluated VSA stiffnesses (blue) compared to Taleo (gray): maximum dorsiflexion angle, peak power, energy return, contralateral knee EAM, COM collision work, and COM push-off work. Optimal VSA stiffness is highlighted (dark blue). Error bars represent ±1 standard deviation.

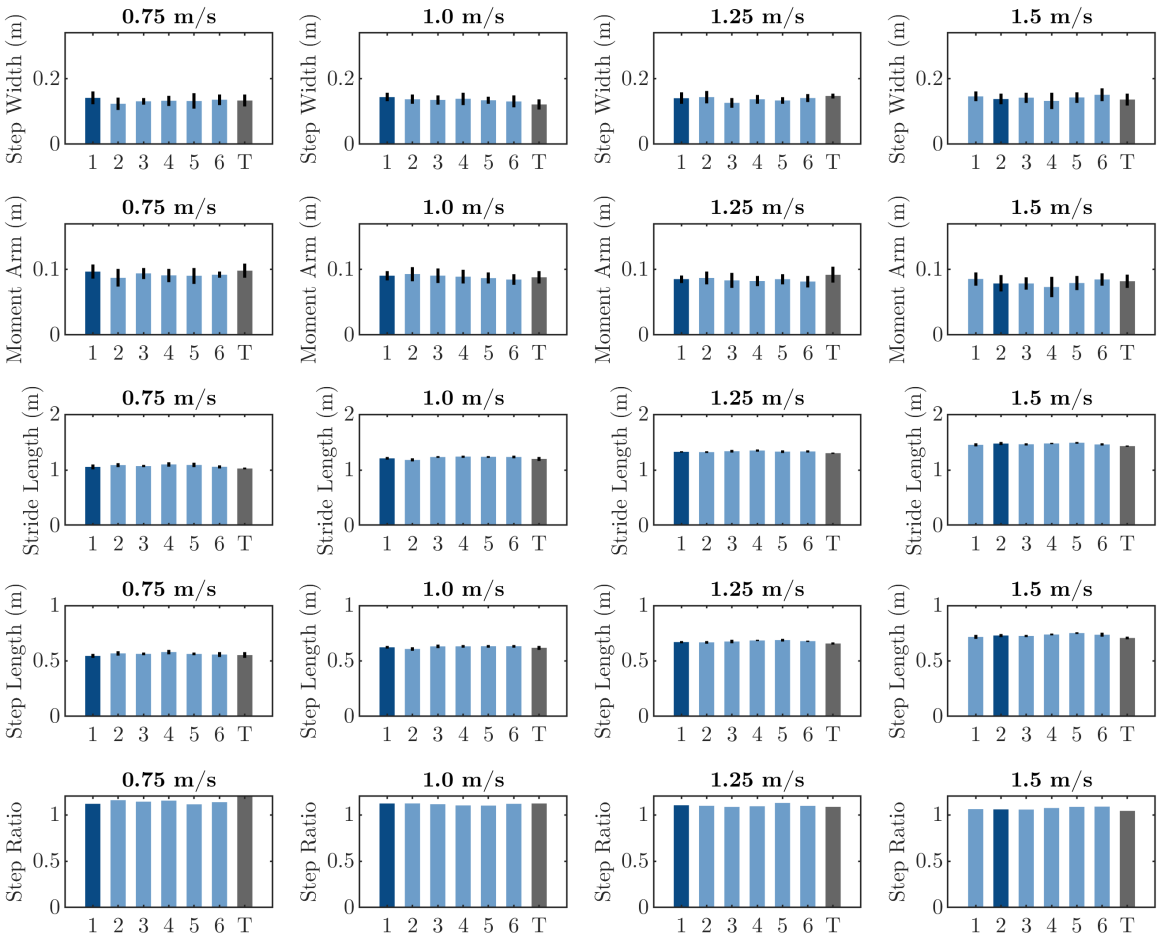

Figure 4-27: **Subject 3 gait parameters.** Gait parameters across speeds for all evaluated VSA stiffnesses (blue) compared to Taleo (gray): step width, knee EAM moment arm, stride length, step length, and step length ratio. Optimal VSA stiffness is highlighted (dark blue). Error bars represent ±1 standard deviation.

4.3.4 Subject 4

Results from Subject 4 are shown in Figure 4-28, Figure 4-29, and Figure 4-30. Figure 4-28 plots prosthesis side and contralateral side joint angles for the ankle, knee, and hip while walking with the VSA and the Taleo across speeds. Figure 4-29 shows joint angle, prosthesis power, contralateral vertical GRF, and contralateral knee EAM for each evaluated walking speed. Figure 4-30 shows mean values of maximum dorsiflexion angle, peak power, energy return, contralateral knee EAM, center of mass collision work, and center of mass push-off work for each evaluated VSA stiffness and the Taleo for each walking speed.

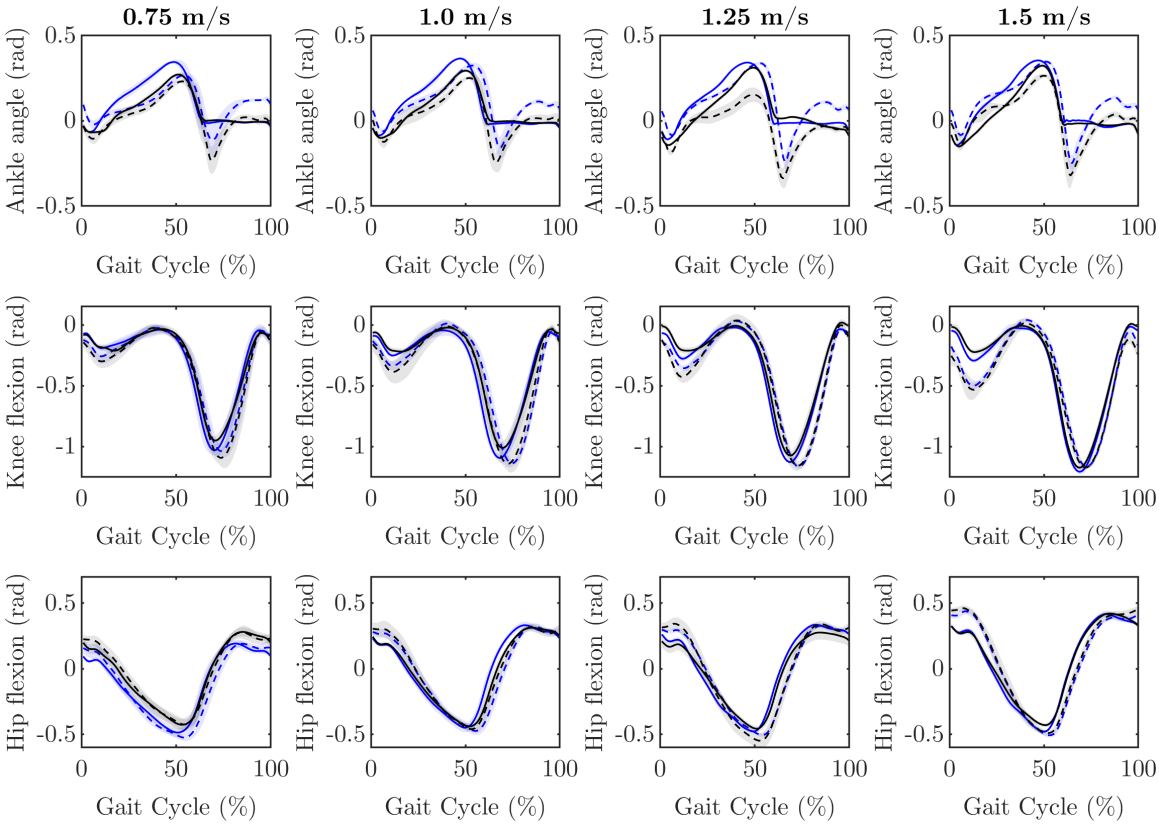

Figure 4-28: **Subject 4 joint angles.** Data is plotted for ankle angle, knee angle, and hip flexion across gait cycle for each speed, for VSA joint angles (blue), VSA contralateral limb (blue dashed), Taleo joint angles (gray), and Taleo contralateral limb (gray dashed).

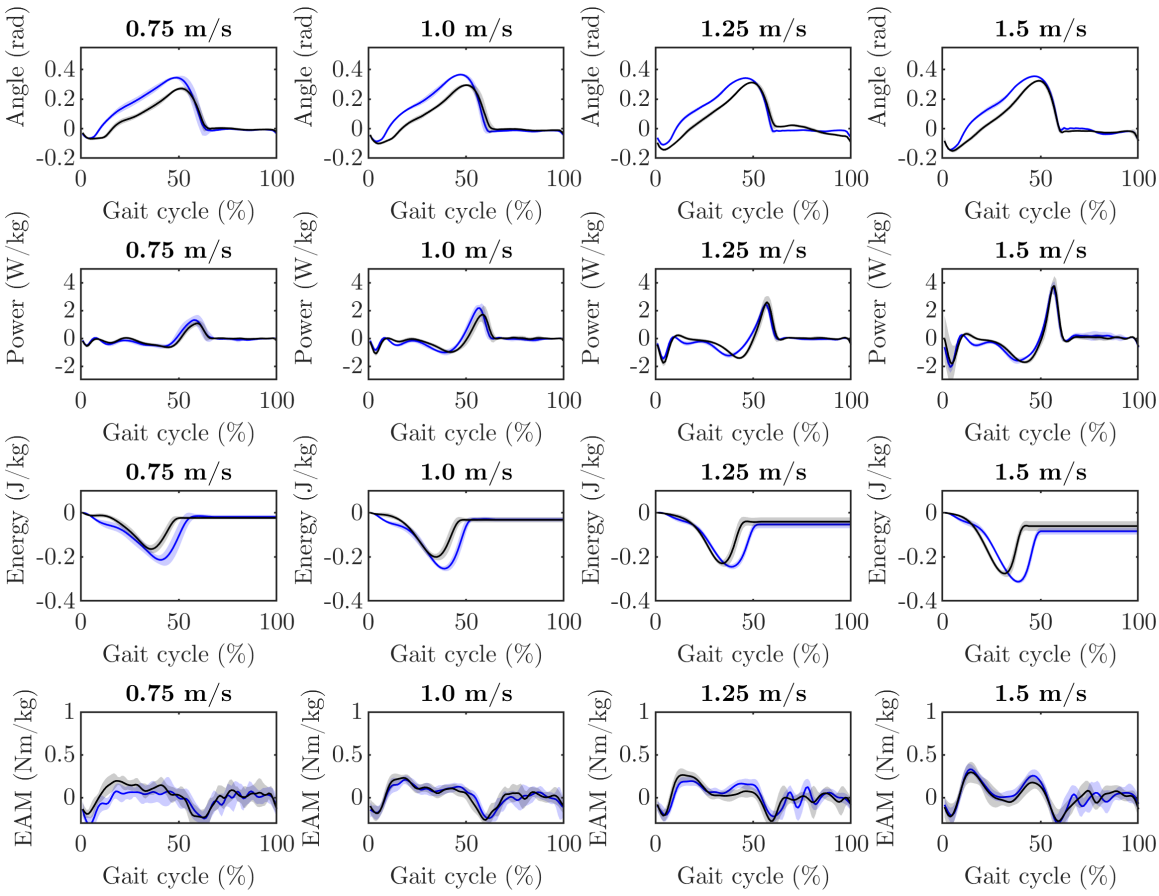

Figure 4-29: **Subject 4 joint angle, power, GRF, and EAM.** Data from optimal VSA (blue) and Taleo (gray) across gait cycle for each walking speed. Plots show dorsiflexion angle, prosthesis power, contralateral vertical GRF, and contralateral knee EAM.

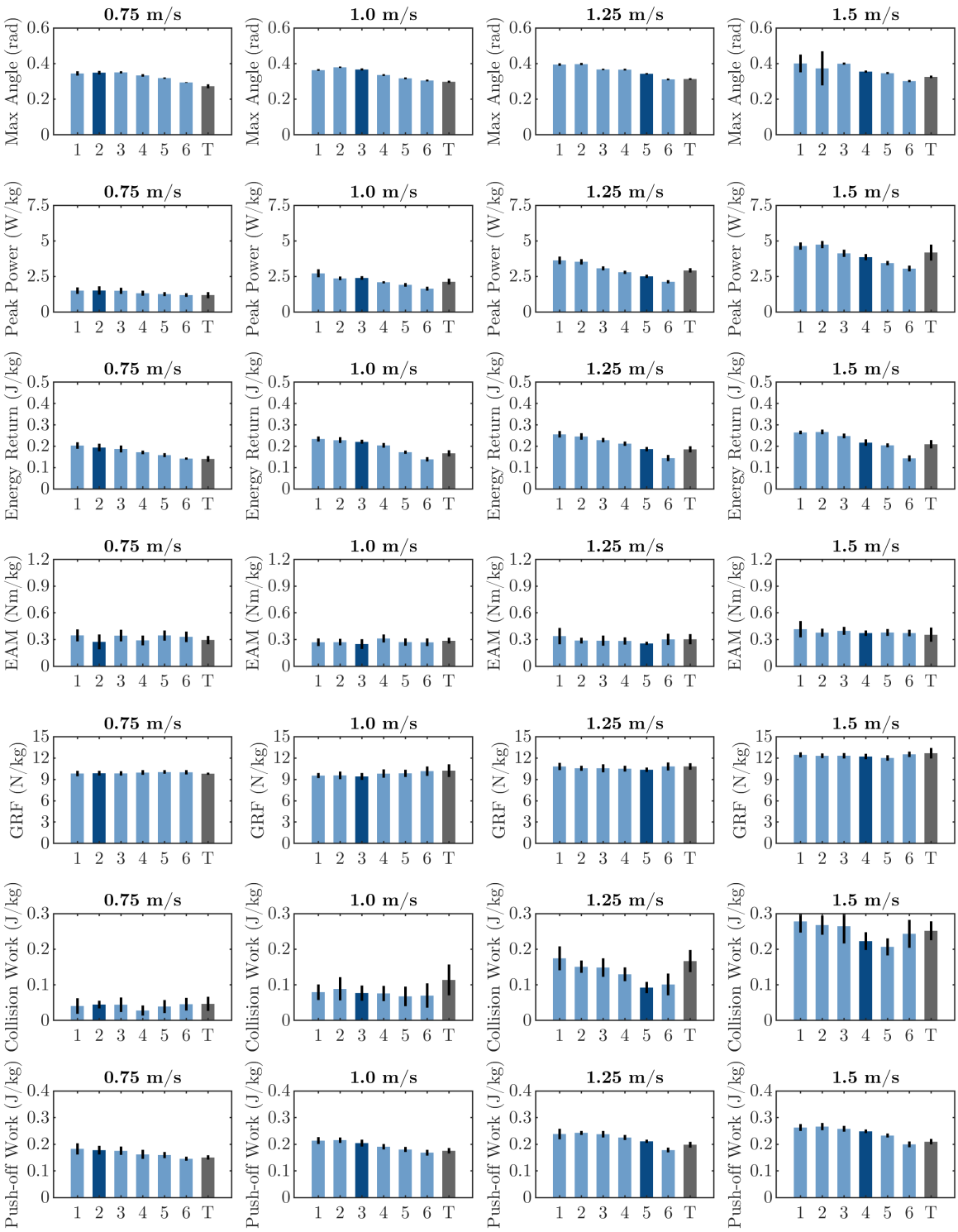

Figure 4-30: **Subject 4 results.** Results across speeds for all evaluated VSA stiffnesses (blue) compared to Taleo (gray): maximum dorsiflexion angle, peak power, energy return, contralateral knee EAM, COM collision work, and COM push-off work. Optimal VSA stiffness is highlighted (dark blue). Error bars represent ±1 standard deviation.

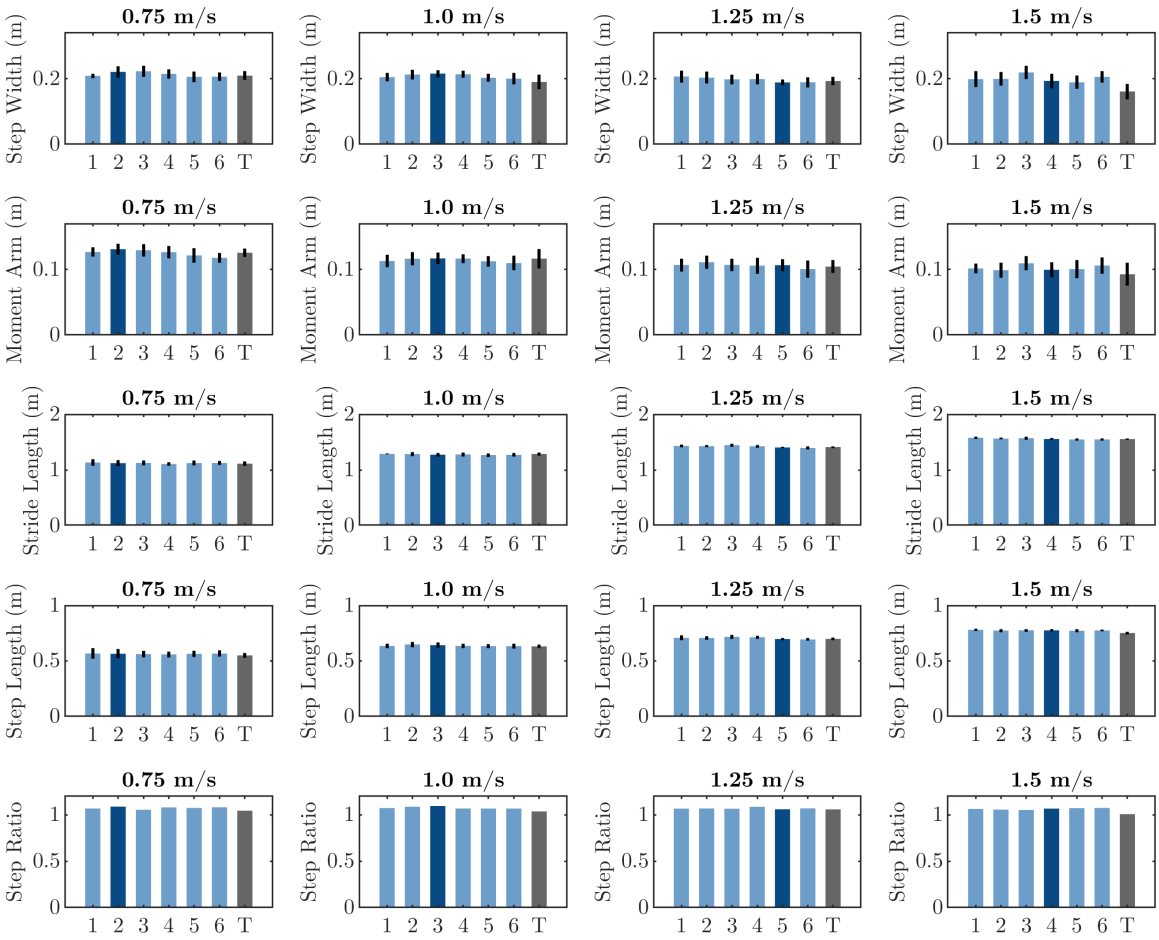

Figure 4-31: **Subject 4 gait parameters.** Gait parameters across speeds for all evaluated VSA stiffnesses (blue) compared to Taleo (gray): step width, knee EAM moment arm, stride length, step length, and step length ratio. Optimal VSA stiffness is highlighted (dark blue). Error bars represent ±1 standard deviation.

4.3.5 Subject 5

Results from Subject 5 are shown in Figure 4-32, Figure 4-33, and Figure 4-34. Figure 4-32 plots prosthesis side and contralateral side joint angles for the ankle, knee, and hip while walking with the VSA and the Taleo across speeds. Figure 4-33 shows joint angle, prosthesis power, contralateral vertical GRF, and contralateral knee EAM for each evaluated walking speed. Figure 4-34 shows mean values of maximum dorsiflexion angle, peak power, energy return, contralateral knee EAM, center of mass collision work, and center of mass push-off work for each evaluated VSA stiffness and the Taleo for each walking speed.

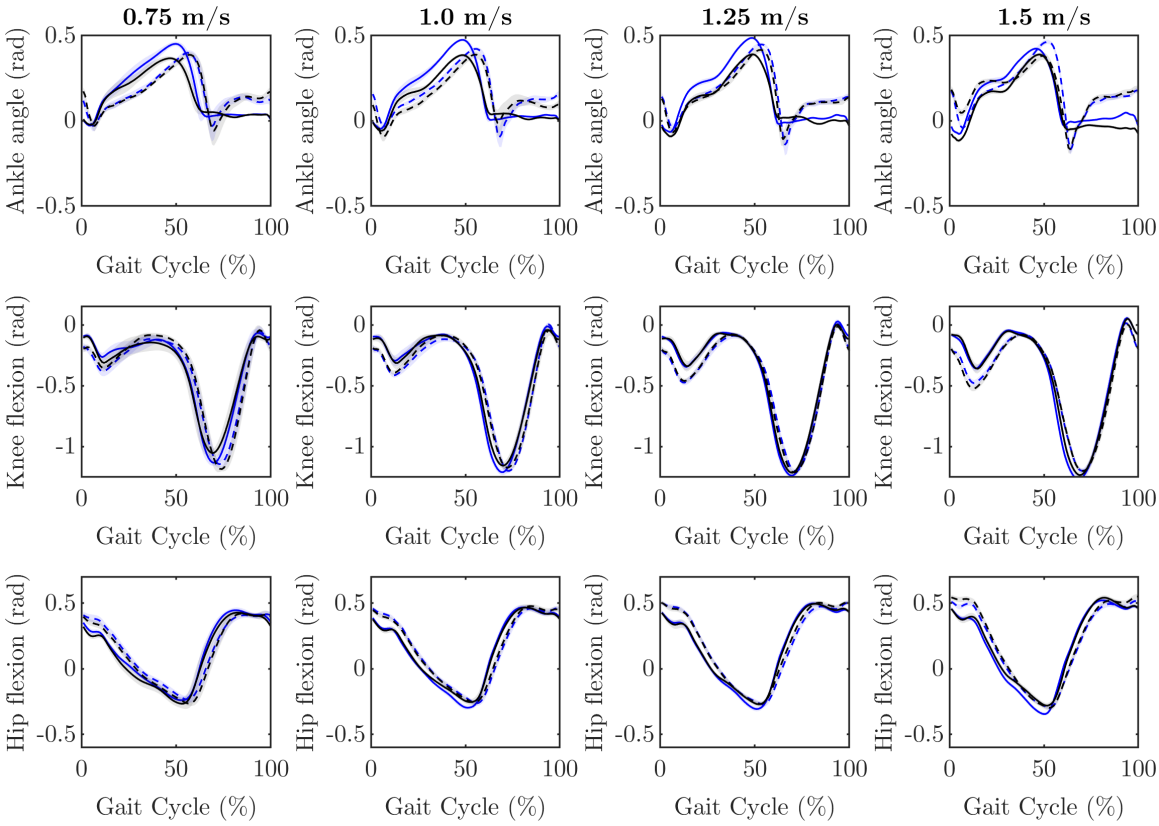

Figure 4-32: **Subject 5 joint angles.** Data is plotted for ankle angle, knee angle, and hip flexion across gait cycle for each speed, for VSA joint angles (blue), VSA contralateral limb (blue dashed), Taleo joint angles (gray), and Taleo contralateral limb (gray dashed).

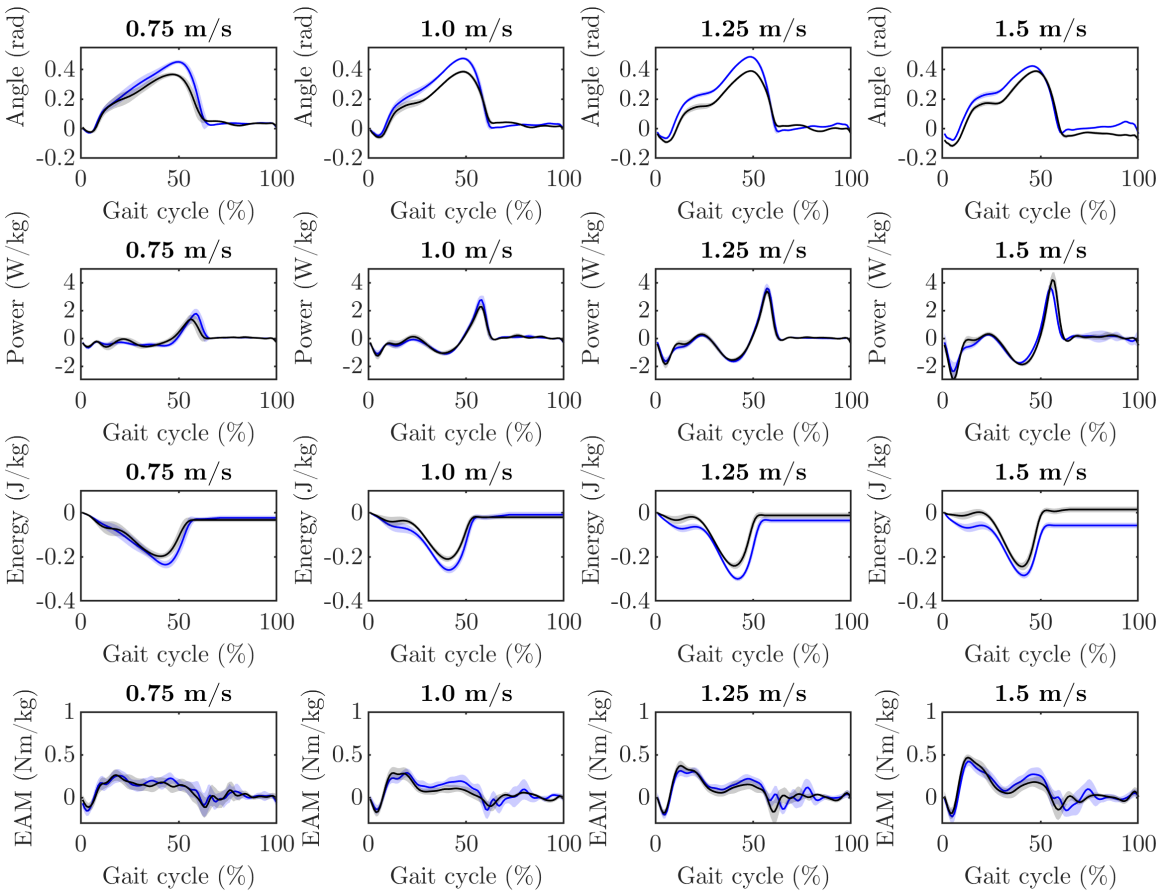

Figure 4-33: **Subject 5 joint angle, power, GRF, and EAM.** Data from optimal VSA (blue) and Taleo (gray) across gait cycle for each walking speed. Plots show dorsiflexion angle, prosthesis power, contralateral vertical GRF, and contralateral knee EAM.

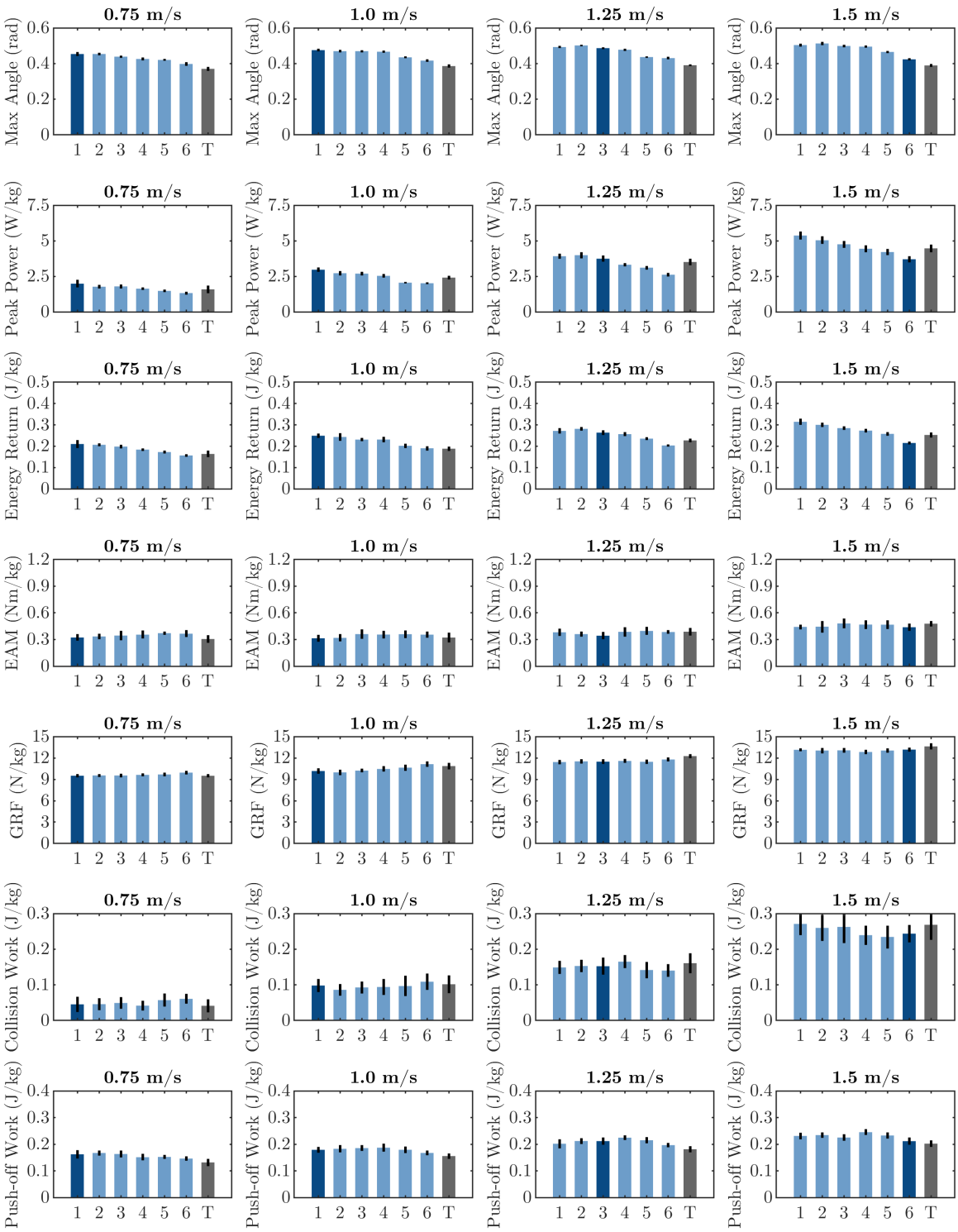

Figure 4-34: **Subject 5 results.** Results across speeds for all evaluated VSA stiffnesses (blue) compared to Taleo (gray): maximum dorsiflexion angle, peak power, energy return, contralateral knee EAM, COM collision work, and COM push-off work. Optimal VSA stiffness is highlighted (dark blue). Error bars represent ±1 standard deviation.

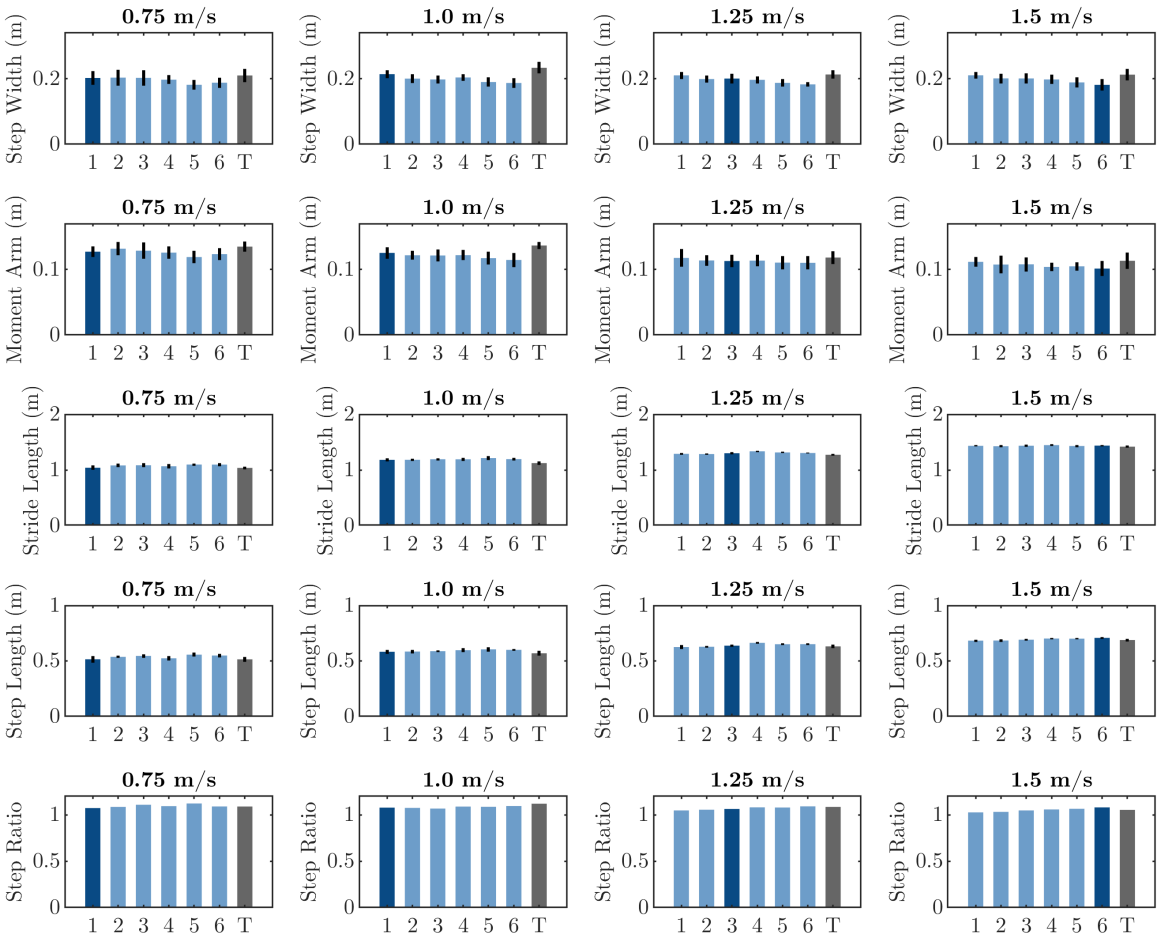

Figure 4-35: **Subject 5 gait parameters.** Gait parameters across speeds for all evaluated VSA stiffnesses (blue) compared to Taleo (gray): step width, knee EAM moment arm, stride length, step length, and step length ratio. Optimal VSA stiffness is highlighted (dark blue). Error bars represent ±1 standard deviation.

4.3.6 Subject 6

Results from Subject 6 are shown in Figure 4-36, Figure 4-37, and Figure 4-38. Figure 4-36 plots prosthesis side and contralateral side joint angles for the ankle, knee, and hip while walking with the VSA and the Taleo across speeds. Figure 4-37 shows joint angle, prosthesis power, contralateral vertical GRF, and contralateral knee EAM for each evaluated walking speed. Figure 4-38 shows mean values of maximum dorsiflexion angle, peak power, energy return, contralateral knee EAM, center of mass collision work, and center of mass push-off work for each evaluated VSA stiffness and the Taleo for each walking speed.

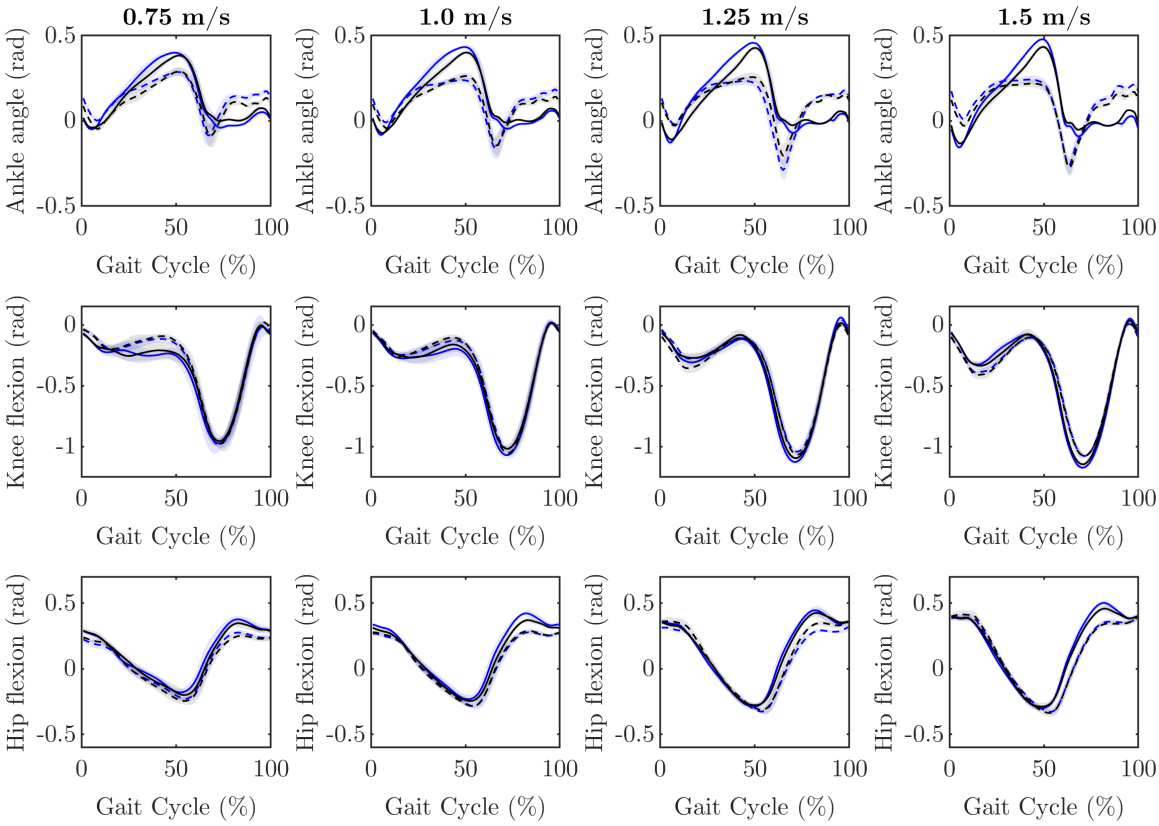

Figure 4-36: **Subject 6 joint angles.** Data is plotted for ankle angle, knee angle, and hip flexion across gait cycle for each speed, for VSA joint angles (blue), VSA contralateral limb (blue dashed), Taleo joint angles (gray), and Taleo contralateral limb (gray dashed).

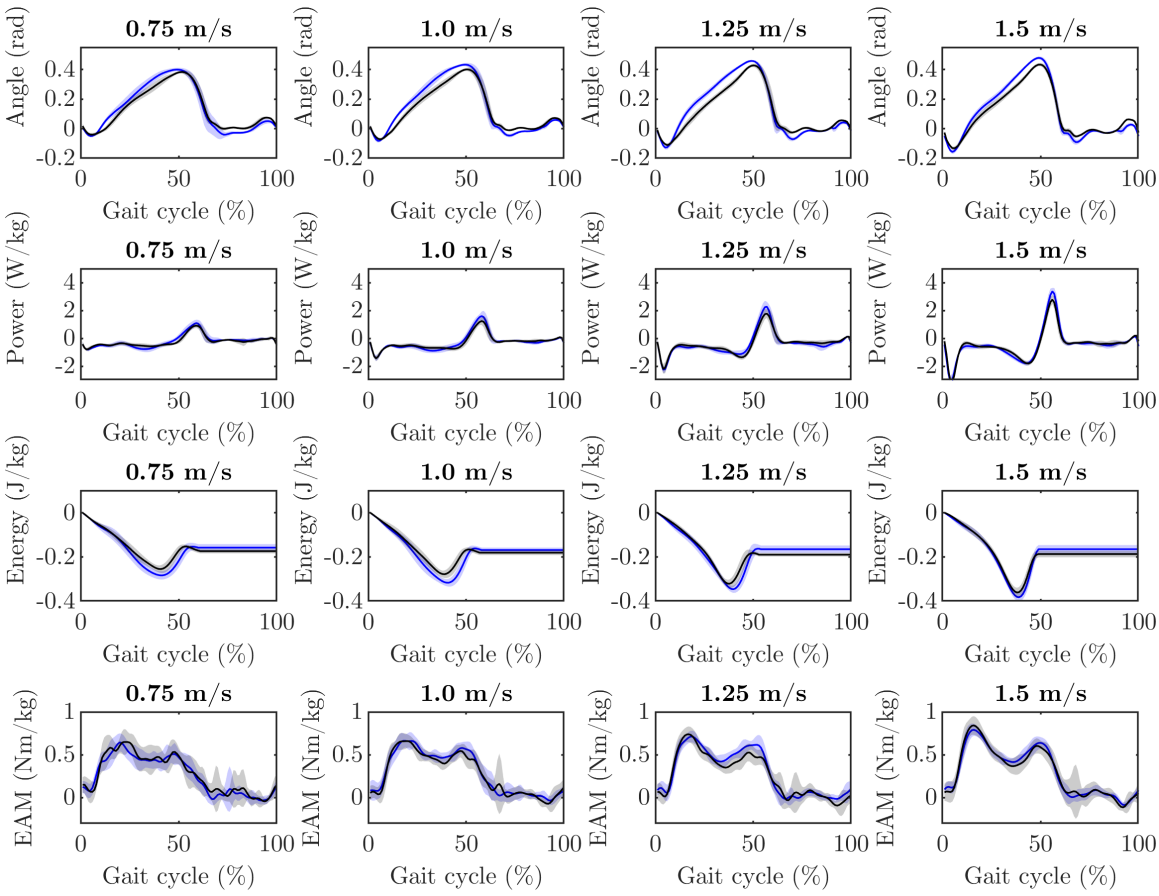

Figure 4-37: **Subject 6 joint angle, power, GRF, and EAM.** Data from optimal VSA (blue) and Taleo (gray) across gait cycle for each walking speed. Plots show dorsiflexion angle, prosthesis power, contralateral vertical GRF, and contralateral knee EAM.

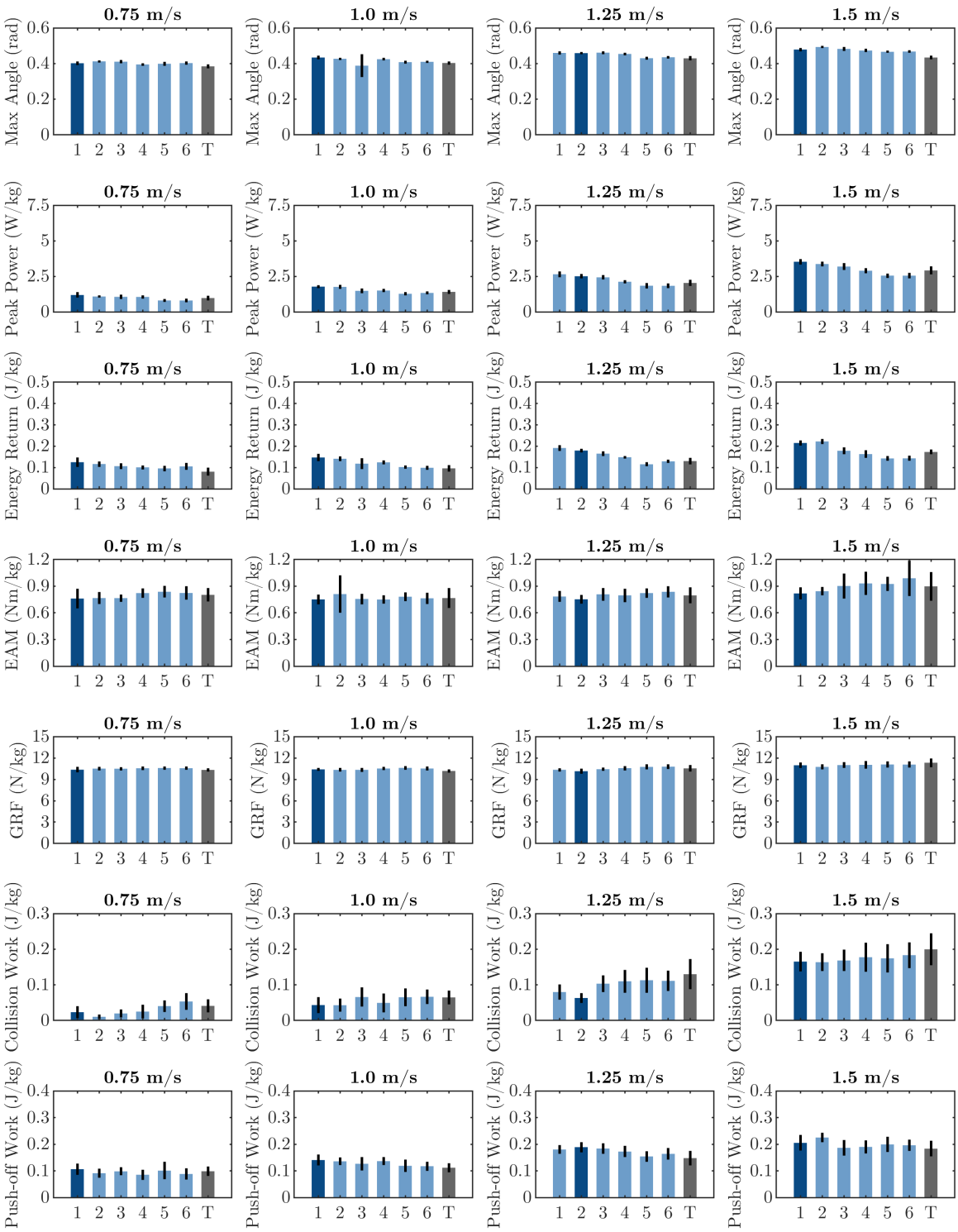

Figure 4-38: **Subject 6 results.** Results across speeds for all evaluated VSA stiffnesses (blue) compared to Taleo (gray): maximum dorsiflexion angle, peak power, energy return, contralateral knee EAM, COM collision work, and COM push-off work. Optimal VSA stiffness is highlighted (dark blue). Error bars represent ±1 standard deviation.

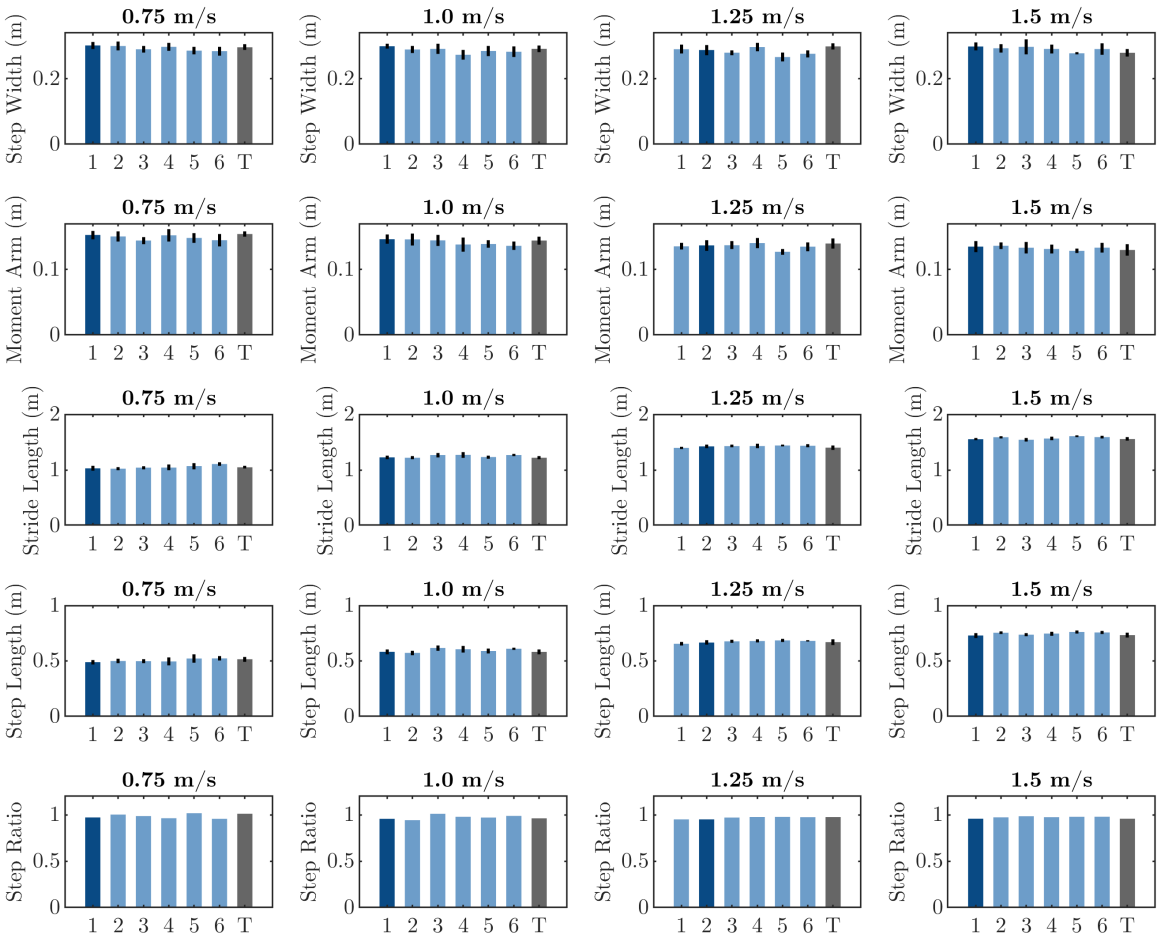

Figure 4-39: **Subject 6 gait parameters.** Gait parameters across speeds for all evaluated VSA stiffnesses (blue) compared to Taleo (gray): step width, knee EAM moment arm, stride length, step length, and step length ratio. Optimal VSA stiffness is highlighted (dark blue). Error bars represent ±1 standard deviation.

4.3.7 Subject 7

Results from Subject 7 are shown in Figure 4-40, Figure 4-41, and Figure 4-42. Figure 4-40 plots prosthesis side and contralateral side joint angles for the ankle, knee, and hip while walking with the VSA and the Taleo across speeds. Figure 4-41 shows joint angle, prosthesis power, contralateral vertical GRF, and contralateral knee EAM for each evaluated walking speed. Figure 4-42 shows mean values of maximum dorsiflexion angle, peak power, energy return, contralateral knee EAM, center of mass collision work, and center of mass push-off work for each evaluated VSA stiffness and the Taleo for each walking speed.

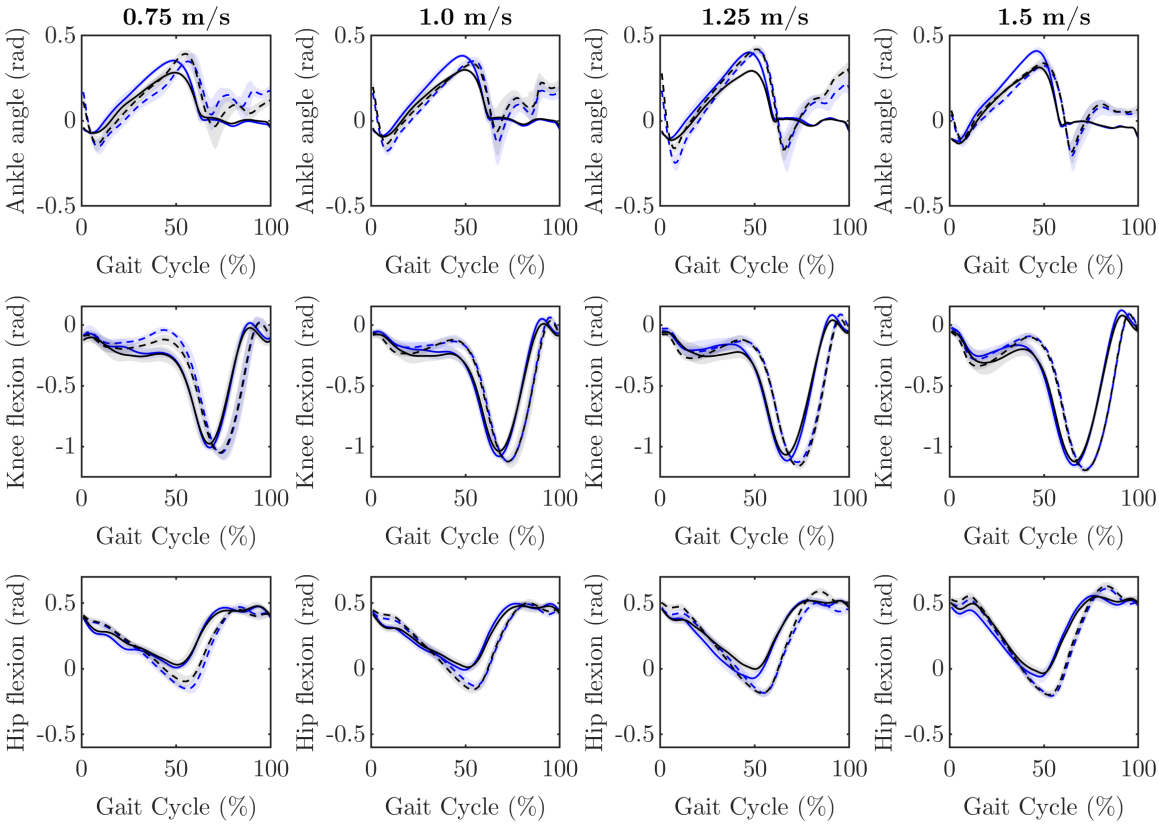

Figure 4-40: **Subject 7 joint angles.** Data is plotted for ankle angle, knee angle, and hip flexion across gait cycle for each speed, for VSA joint angles (blue), VSA contralateral limb (blue dashed), Taleo joint angles (gray), and Taleo contralateral limb (gray dashed).

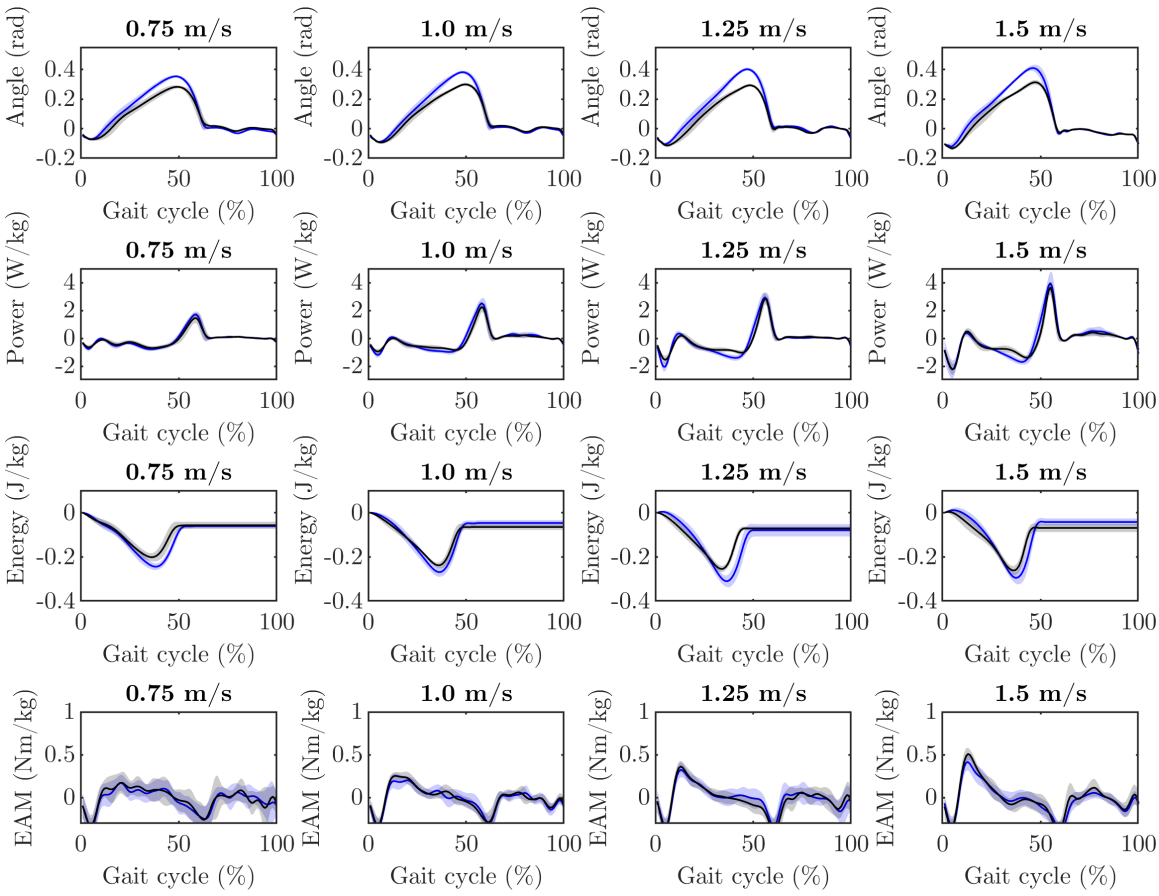

Figure 4-41: **Subject 7 joint angle, power, GRF, and EAM.** Data from optimal VSA (blue) and Taleo (gray) across gait cycle for each walking speed. Plots show dorsiflexion angle, prosthesis power, contralateral vertical GRF, and contralateral knee EAM.

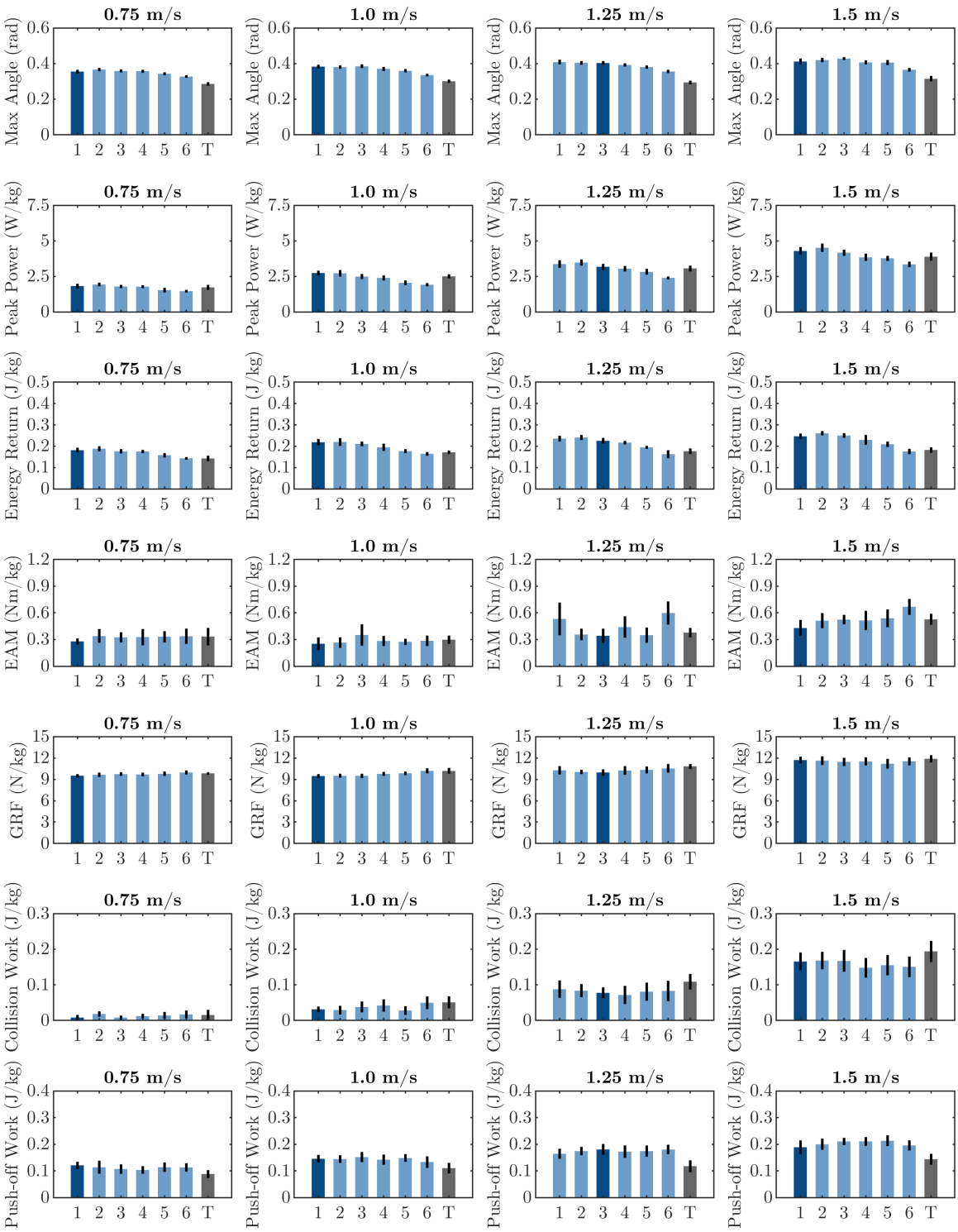

Figure 4-42: **Subject 7 results.** Results across speeds for all evaluated VSA stiffnesses (blue) compared to Taleo (gray): maximum dorsiflexion angle, peak power, energy return, contralateral knee EAM, COM collision work, and COM push-off work. Optimal VSA stiffness is highlighted (dark blue). Error bars represent ±1 standard deviation.

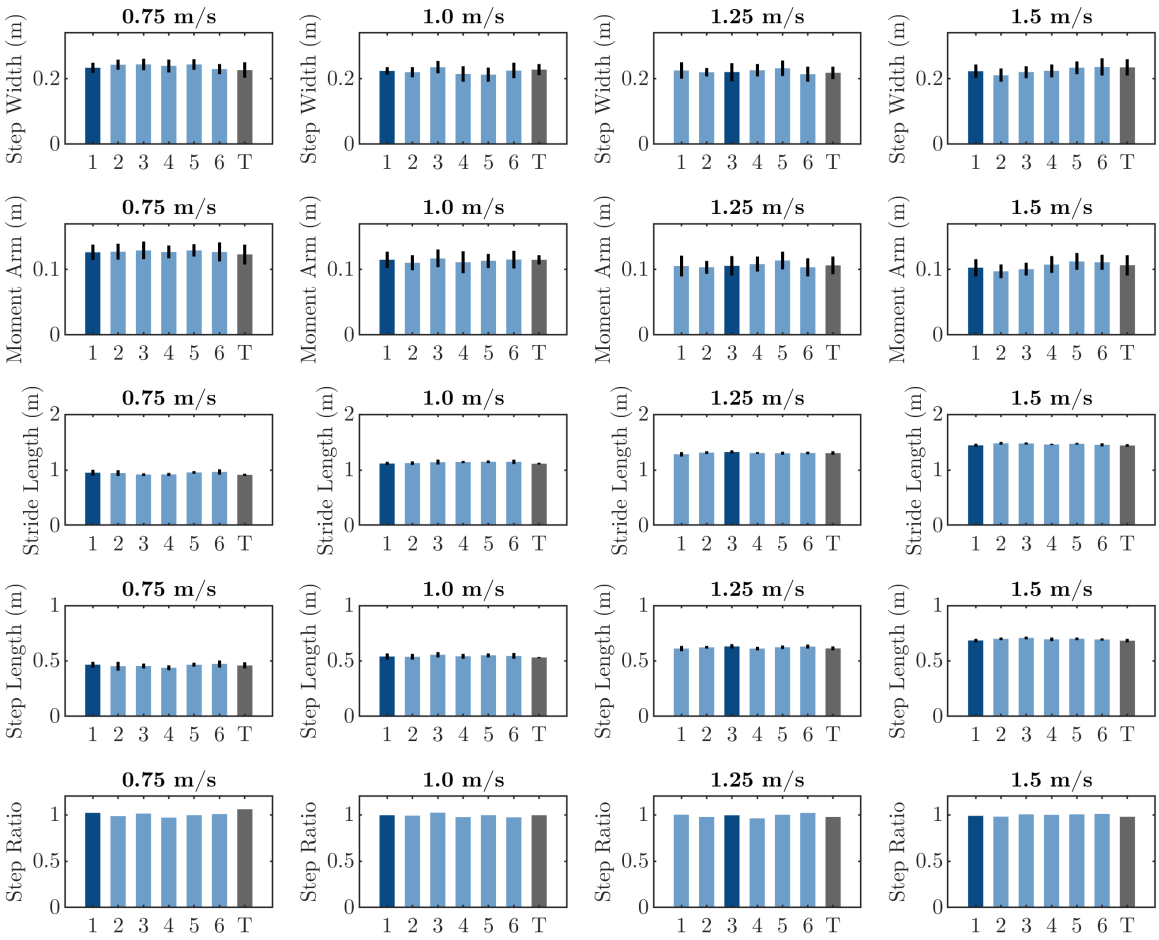

Figure 4-43: **Subject 7 gait parameters.** Gait parameters across speeds for all evaluated VSA stiffnesses (blue) compared to Taleo (gray): step width, knee EAM moment arm, stride length, step length, and step length ratio. Optimal VSA stiffness is highlighted (dark blue). Error bars represent ±1 standard deviation.

4.4 Optimal Prosthesis Stiffness

4.4.1 Dimensionless Numbers

Froude number We use the Froude number to compare relative walking speeds between subjects of different heights and leg lengths. The Froude number is a dimensionless number which represents the ratio of centripetal force to gravitational force in an inverted pendulum model of walking [69]. The Froude number scales proportionally with walking speed and inversely with leg length. The walk to run transition typically occurs at a Froude number of 0.5 [69]. The Froude number is calculated as in Equation 4.5, where v is walking velocity ($\frac{m}{s}$), g is the acceleration due to gravity ($\frac{m}{s^2}$), and l_{leg} is leg length (m) from the ground to the greater trochanter of the femoral head.

$$Fr = \frac{v^2}{gl_{leg}} \tag{4.5}$$

Stiffness ratio This thesis presents a new dimensionless number called the stiffness ratio which represents the ratio of prosthetic ankle stiffness to leg length and body weight. Equation 4.6 defines the stiffness ratio Kr, where k_θ is the rotational stiffness of the prosthetic ankle ($\frac{Nm}{rad}$), l_{leg} is leg length (m) from the ground to the greater trochanter of the femoral head, g is the acceleration due to gravity ($\frac{m}{s^2}$), and m_{body} is body mass (kg). A stiffness factor of 1 indicates a prosthesis stiffness that is equal to the product of leg length and body weight.

$$Kr = \frac{k_\theta}{l_{leg} g m_{body}} \tag{4.6}$$

4.4.2 Optimal Prosthesis Stiffness

Figure 4-44 demonstrates the relationship between walking speed (as represented by the dimensionless Froude number) to optimal prosthetic ankle stiffness (as represented by dimensionless stiffness factor).

$$Kr_{optimal} = 0.306Fr + 0.467 \tag{4.7}$$

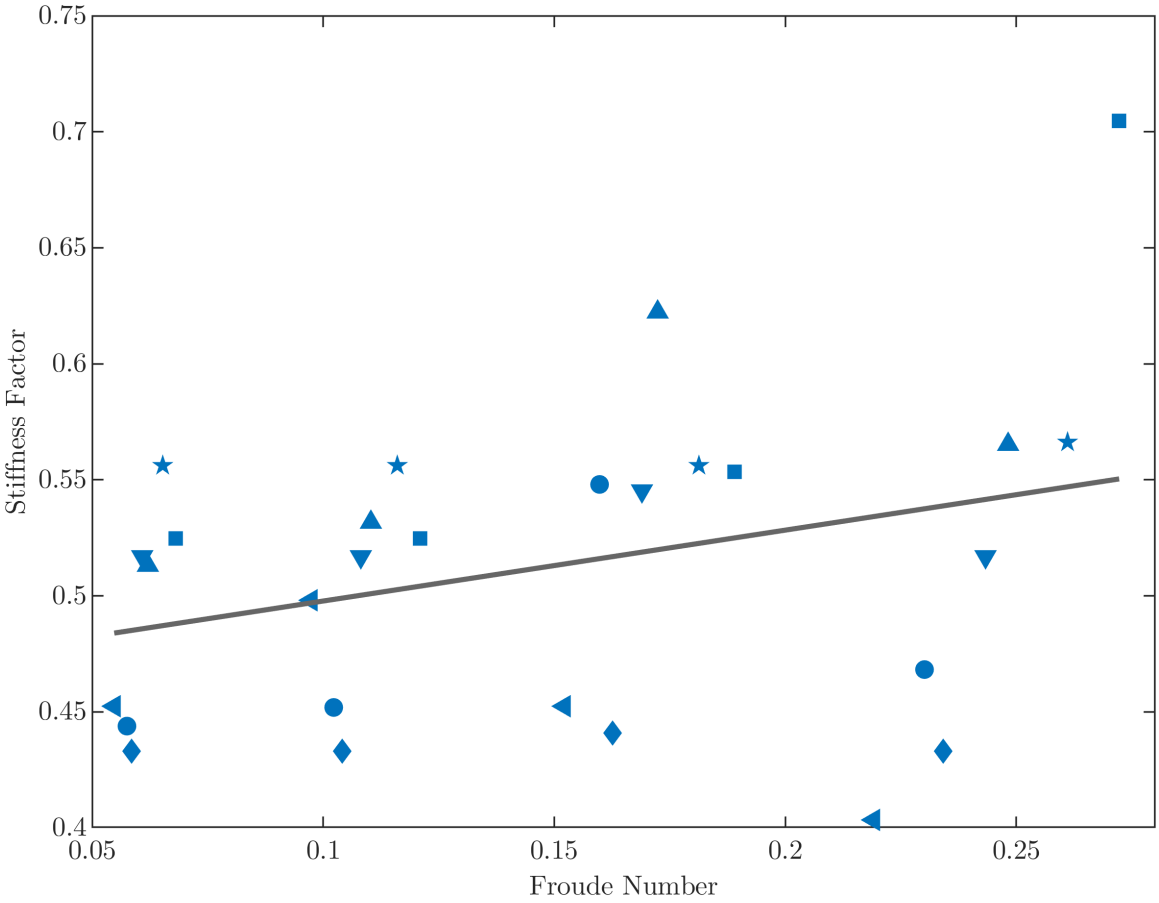

Figure 4-44: **Optimal Stiffness.** Linear model approximates the optimal prosthesis stiffness as represented by the dimensionless stiffness ratio for a given dimensionless walking speed.

$$k_{\theta_{optimal}} = l_{leg} g m_{body} \left(0.306 Fr + 0.467\right) \tag{4.8}$$

Equations 4.7 and 4.8 approximately describes the optimal stiffness as defined by the lowest knee EAM, the correlation coefficient of this linear model is $R = 0.33$. Additional work is needed to develop a more robust model of optimallity.

4.5 Discussion

This study demonstrates the performance of the variable stiffness ankle during level ground walking at various speeds and provides preliminary evidence of potential advantages of the quasi-passive variable stiffness ankle-foot prosthesis. The presented

results demonstrate an increased prosthesis range of motion, increase in peak ankle power, increase in stored and returned energy, and a decrease in external adduction moment of the contralateral limb while walking with the variable stiffness prosthesis compared to the passive device, across evaluated walking speeds. The optimal prosthesis stiffness, which we define by the condition which minimizes the first peak of EAM, generally increases with increasing walking speed. This trend agrees with the behavior of the biological ankle-foot complex, which demonstrates an increase in quasi-stiffness as walking speed increases. By optimizing prosthesis stiffness based on walking speed, energy storage and subsequent energy return is increased, leading to increased peak power in a quasi-passive device. This is an exciting result that demonstrates the importance of maximizing energy storage in passive or quasi-passive devices in order to decrease unwanted contralateral limb loading. This result could have important implications for how prostheses are designed, and demonstrates the importance of adaptable prosthesis stiffness.

4.6 Future Work

4.6.1 Clinical Impacts

Long-term clinical studies are necessary in order to determine the impact of the achieved reduction in contralateral limb loading on long-term health outcomes. Prior research on changing prosthesis stiffness has demonstrated that prosthesis users can detect a change on prosthesis stiffness of $7.7 \pm 1.3\%$ with an accuracy of 75% [64]. Further research is needed on the relationship between user preference, perception, and optimality.

4.6.2 Diversity of Study Participants

The current study presents results from study participants who range in body mass from 74.8-86.5 kg, range in height from 1.70 - 1.91 m, range in age from 46 - 58 years, and all participants were male (Table 4.1). Future studies should explore if

the results demonstrated in the present study apply to participant groups of varied weight, height, age, and sex.

4.6.3 Optimal Stiffness

Further studies are needed to determine a predictive model for optimal prosthesis across walking speeds. The presented data shows a decrease in optimal prosthesis stiffness at fast walking speeds (as defined by minimization of knee EAM) for several subjects, additional testing is needed to explore this phenomena.

Chapter 5

Conclusion

This chapter presents the novel contributions of this thesis, concluding remarks, and a description of potential future directions.

5.1 Thesis Contributions

The work presented in this thesis (1) determines a method for increasing energy storage and peak power in a quasi-passive system; (2) develops a novel quasi-passive variable stiffness ankle-foot prosthesis; and (3) demonstrates biomechanical benefits of the presented device compared to standard prostheses. Details of these contributions are summarized below:

- Developed novel mechanism for adjusting the stiffness of leaf springs [5].
- Designed and evaluated variable stiffness ankle-foot prosthesis to match biological levels of ankle quasi-stiffness during walking [6].
- Designed and conducted clinical study with n(7) study participants with unilateral trans-tibial amputation to evaluate the effects of adjusting device stiffness on biomechanics of walking.
- Demonstrated a statistically significant increase in energy storage, increase in

peak power, and decrease in contralateral limb loading and knee external adduction moment across walking speeds in clinical study.

5.2 Conclusions

This thesis presents the first of its architecture variable stiffness ankle-foot prosthesis utilizing a novel locking parallel leaf spring mechanism for stiffness control. This prosthesis design has a lower device mass compared to existing powered and quasi-passive devices, and increases biomimetic functionality beyond standard passive prostheses. This thesis presents clinical results demonstrating the benefits of such a device on the biomechanics and energetics of people with transtibial amputation while walking. This prosthesis has the potential to expand access to high performance prosthesis technology by creating a device that is low mass, low power, and lower cost compared to fully powered devices. This device has the potential to improve health outcomes in people with transtibial amputation by normalizing biomechanics and increasing energy storage and return, and decreasing contralateral limb loading and unwanted knee EAM.

5.3 Future Work

This research motivates additional studies to further explore the effect of a quasi-passive variable stiffness device on the biomechanics and energetics of variable speed walking. Additionally, this device has the potential to enable explorations of the impact of prosthesis stiffness on biomechanics in a variety of scenarios such as across varied terrain, various ground surfaces, and running. Potential design improvements include further minimizing device mass, expanding the device design to be customizable to any body mass, exploring the optimal stiffness range for a given body mass and height, and improving robustness of the device.

Appendix A

Appendix A

A.1 Engineering Drawings

REVISIONS				
ZONE	REV.	DESCRIPTION	DATE	APPROVED

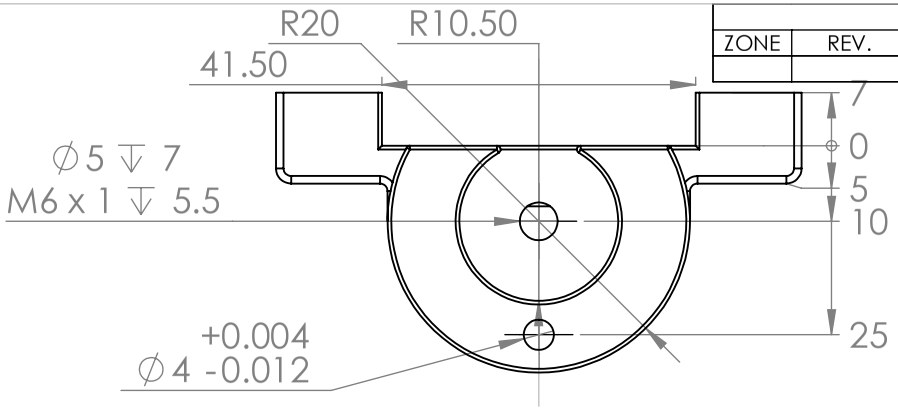

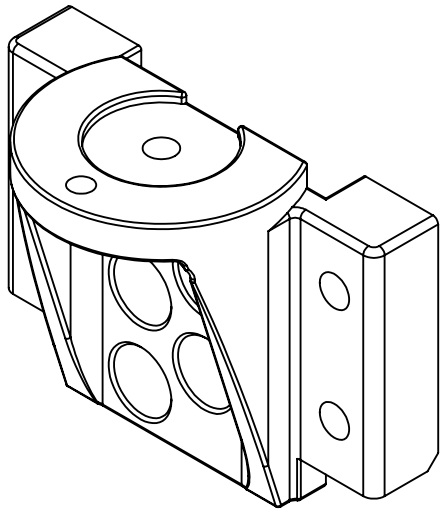

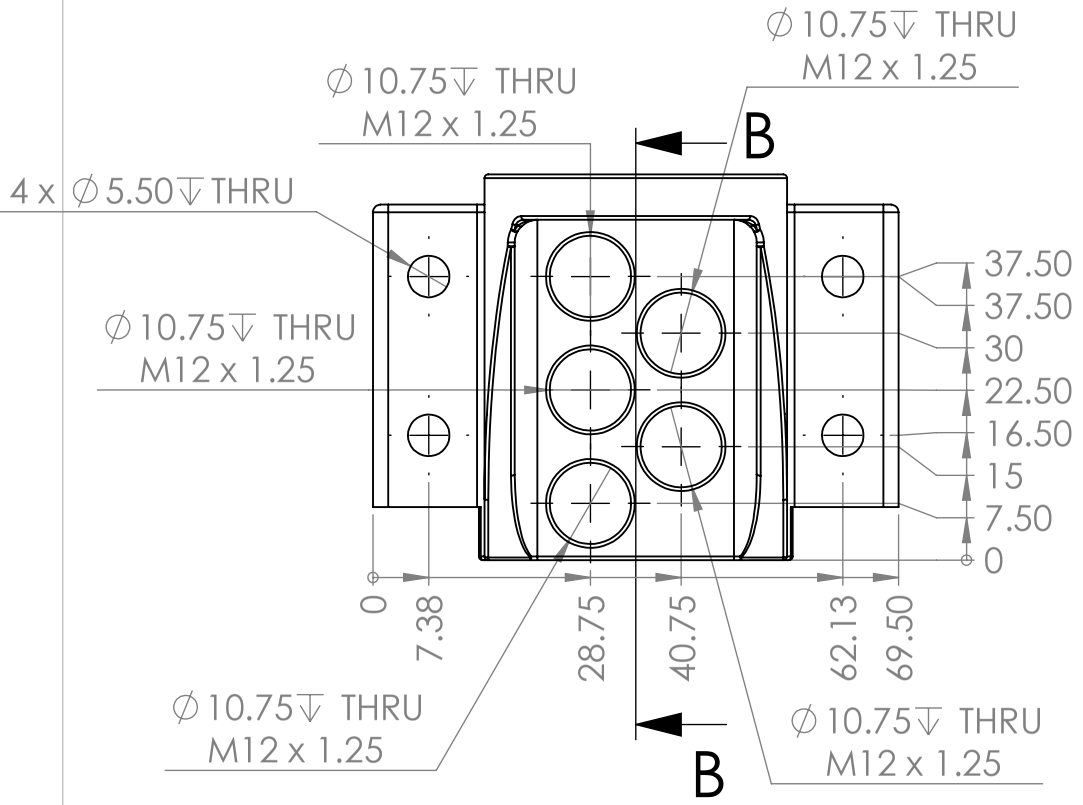

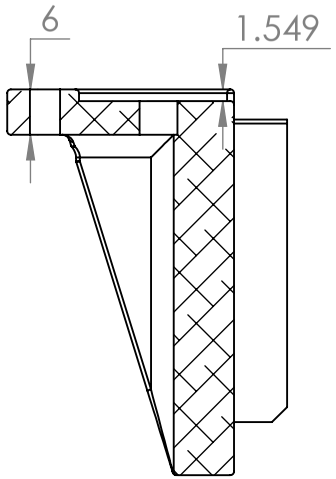

SECTION B-B

PROPRIETARY AND CONFIDENTIAL

THE INFORMATION CONTAINED IN THIS DRAWING IS THE SOLE PROPERTY OF MIT MEDIA LAB BIOMECHATRONICS. ANY REPRODUCTION IN PART OR AS A WHOLE WITHOUT THE WRITTEN PERMISSION OF MIT MEDIA LAB BIOMECHATRONICS IS PROHIBITED.

All dimensions are in *mm* and apply to finished (after plating) parts unless noted otherwise.

Break all sharp corners 0.25 max

Metric	[Inch]
.0 ± .2	.0 ± .01
.00 ± .1	.00 ± .005
.000 ± .02	.000 ± .001
	.0000 +.0005/-0.0

biomechatronics

Massachussetts Institute of Technology
Media Lab Biomechatronics
75 Amherst St. Room E14-374N
Cambridge, MA 02142
+1 (617)680-0048
emrogers@mit.edu

This Drawing is the property of MIT Media Lab Biomechatronics, and can not be reproduced without the expressed written consent of MIT Media Lab Biomechatronics.

11/2/2021

Scale 1:1

Sheet 1 of 1

VSA04_01_010_housingfront

Rev - A-01

Material: 7075-T6 (SN)

Finish: TUMBLE, ANODIZE CLEAR

SOLIDWORKS Educational Product. For Instructional Use Only.

REVISIONS				
ZONE	REV.	DESCRIPTION	DATE	APPROVED

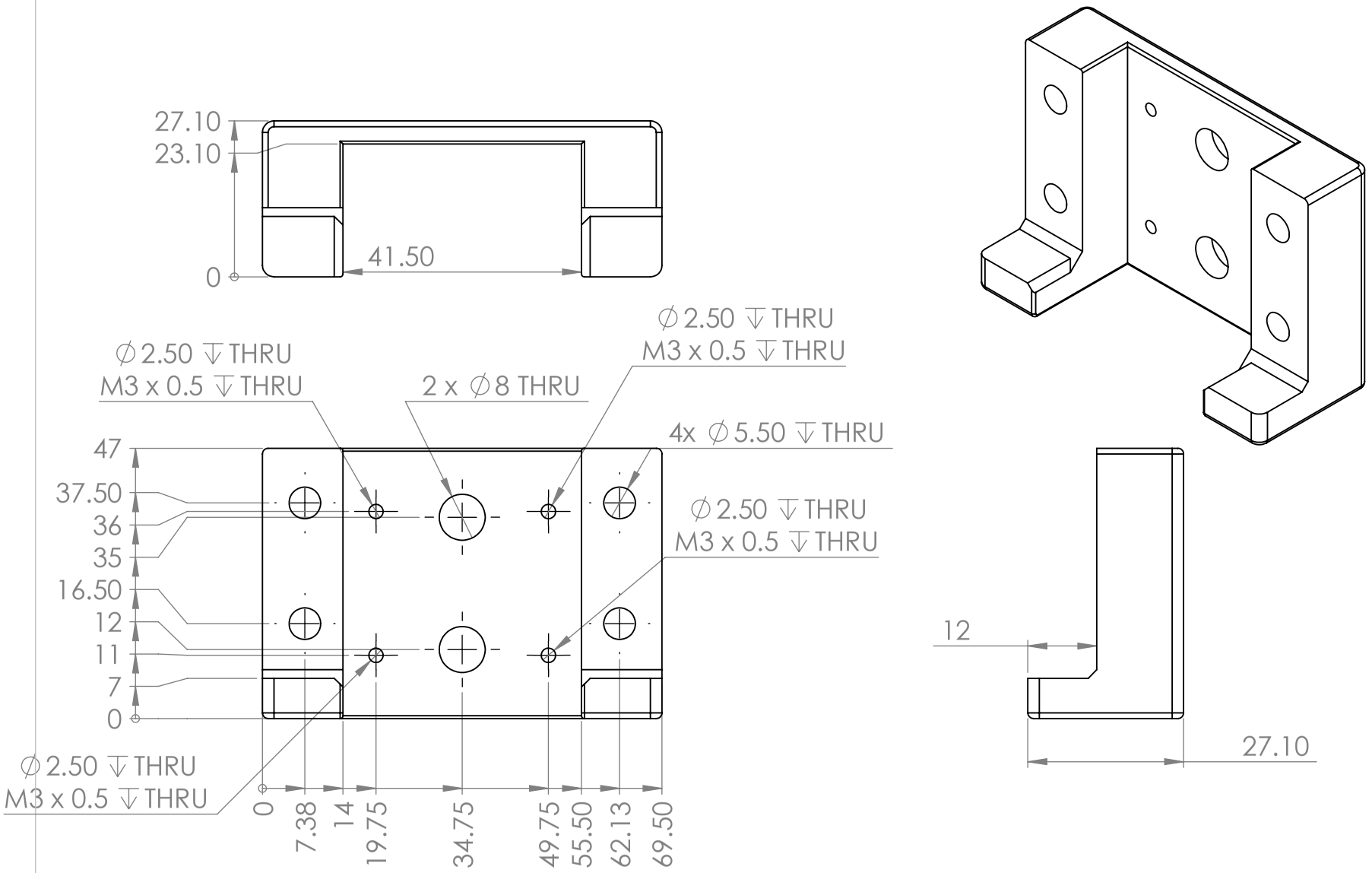

PROPRIETARY AND CONFIDENTIAL

THE INFORMATION CONTAINED IN THIS DRAWING IS THE SOLE PROPERTY OF MIT MEDIA LAB BIOMECHATRONICS. ANY REPRODUCTION IN PART OR AS A WHOLE WITHOUT THE WRITTEN PERMISSION OF MIT MEDIA LAB BIOMECHATRONICS IS PROHIBITED.

All dimensions are in *mm* and apply to finished (after plating) parts unless noted otherwise.

Break all sharp corners 0.25 max

Metric	[Inch]
.0 ± .2	.0 ± .01
.00 ± .1	.00 ± .005
.000 ± .02	.000 ± .001
	.0000 +.0005/-0.0

biomechatronics

Massachussetts Institute of Technology
Media Lab Biomechatronics
75 Amherst St. Room E14-374N
Cambridge, MA 02142
+1 (617)680-0048
emrogers@mit.edu

This Drawing is the property of MIT Media Lab Biomechatronics, and can not be reproduced without the expressed written consent of MIT Media Lab Biomechatronics.

11/3/2021

Scale 1:1

Sheet 1 of 1

VSA04_01_001_housingback_13ply

Rev - A-01

Material: 7075-T6 (SN)

Finish: TUMBLE, ANODIZE CLEAR

SOLIDWORKS Educational Product. For Instructional Use Only.

REVISIONS				
ZONE	REV.	DESCRIPTION	DATE	APPROVED

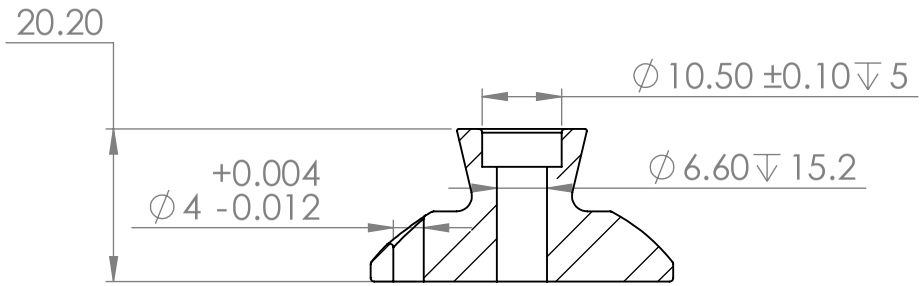

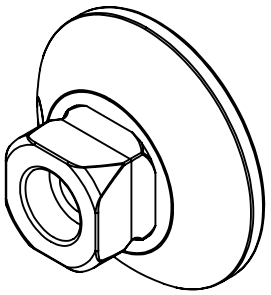

SECTION A-A

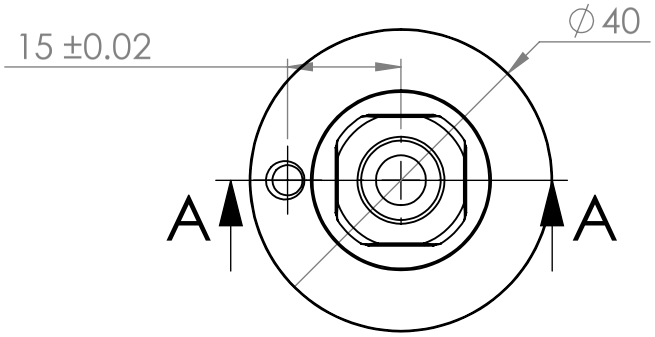

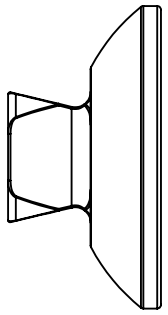

PROPRIETARY AND CONFIDENTIAL

THE INFORMATION CONTAINED IN THIS DRAWING IS THE SOLE PROPERTY OF MIT MEDIA LAB BIOMECHATRONICS. ANY REPRODUCTION IN PART OR AS A WHOLE WITHOUT THE WRITTEN PERMISSION OF MIT MEDIA LAB BIOMECHATRONICS IS PROHIBITED.

All dimensions are in *mm* and apply to finished (after plating) parts unless noted otherwise.

Break all sharp corners 0.25 max

Metric	[Inch]
.0 ± .2	.0 ± .01
.00 ± .1	.00 ± .005
.000 ± .02	.000 ± .001
	.0000 +.0005/-0.0

biomechatronics

Massachussetts Institute of Technology
Media Lab Biomechatronics
75 Amherst St. Room E14-374N
Cambridge, MA 02142
+1 (617)680-0048
emrogers@mit.edu

This Drawing is the property of MIT Media Lab Biomechatronics, and can not be reproduced without the expressed written consent of MIT Media Lab Biomechatronics.

10/29/2021

Scale 1:1

Sheet 1 of 1

VSA04_01_002_pyramid

Rev - A-01

Material: Ti-6Al-4V

Finish:

SOLIDWORKS Educational Product. For Instructional Use Only.

REVISIONS				
ZONE	REV.	DESCRIPTION	DATE	APPROVED

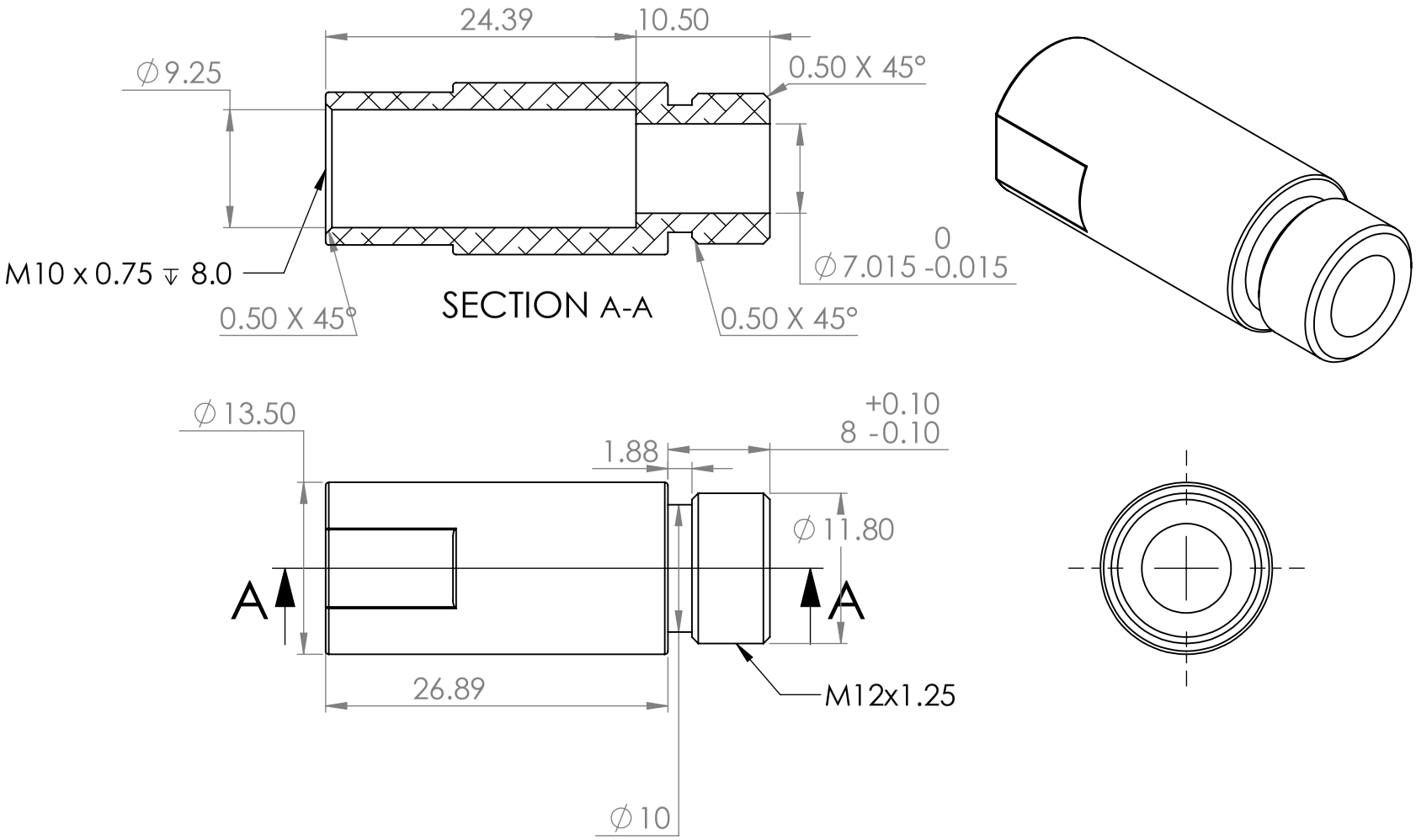

PROPRIETARY AND CONFIDENTIAL

THE INFORMATION CONTAINED IN THIS DRAWING IS THE SOLE PROPERTY OF MIT MEDIA LAB BIOMECHATRONICS. ANY REPRODUCTION IN PART OR AS A WHOLE WITHOUT THE WRITTEN PERMISSION OF MIT MEDIA LAB BIOMECHATRONICS IS PROHIBITED.

All dimensions are in *mm* and apply to finished (after plating) parts unless noted otherwise.

Break all sharp corners 0.25 max

Metric	[Inch]
.0 ± .2	.0 ± .01
.00 ± .1	.00 ± .005
.000 ± .02	.000 ± .001
	.0000 +.0005 / -0.0

biomechatronics

Massachussetts Institute of Technology
Media Lab Biomechatronics
75 Amherst St. Room E14-374N
Cambridge, MA 02142
+1 (617)680-0048
emrogers@mit.edu

This Drawing is the property of MIT Media Lab Biomechatronics, and can not be reproduced without the expressed written consent of MIT Media Lab Biomechatronics.

10/28/2021

Scale 2:1

Sheet 1 of 1

VSA04_01_003_actuatorhousing

Rev - A-01

Material: 7075-T6 (SN)

Finish: TUMBLE, ANODIZE CLEAR

SOLIDWORKS Educational Product. For Instructional Use Only.

REVISIONS				
ZONE	REV.	DESCRIPTION	DATE	APPROVED

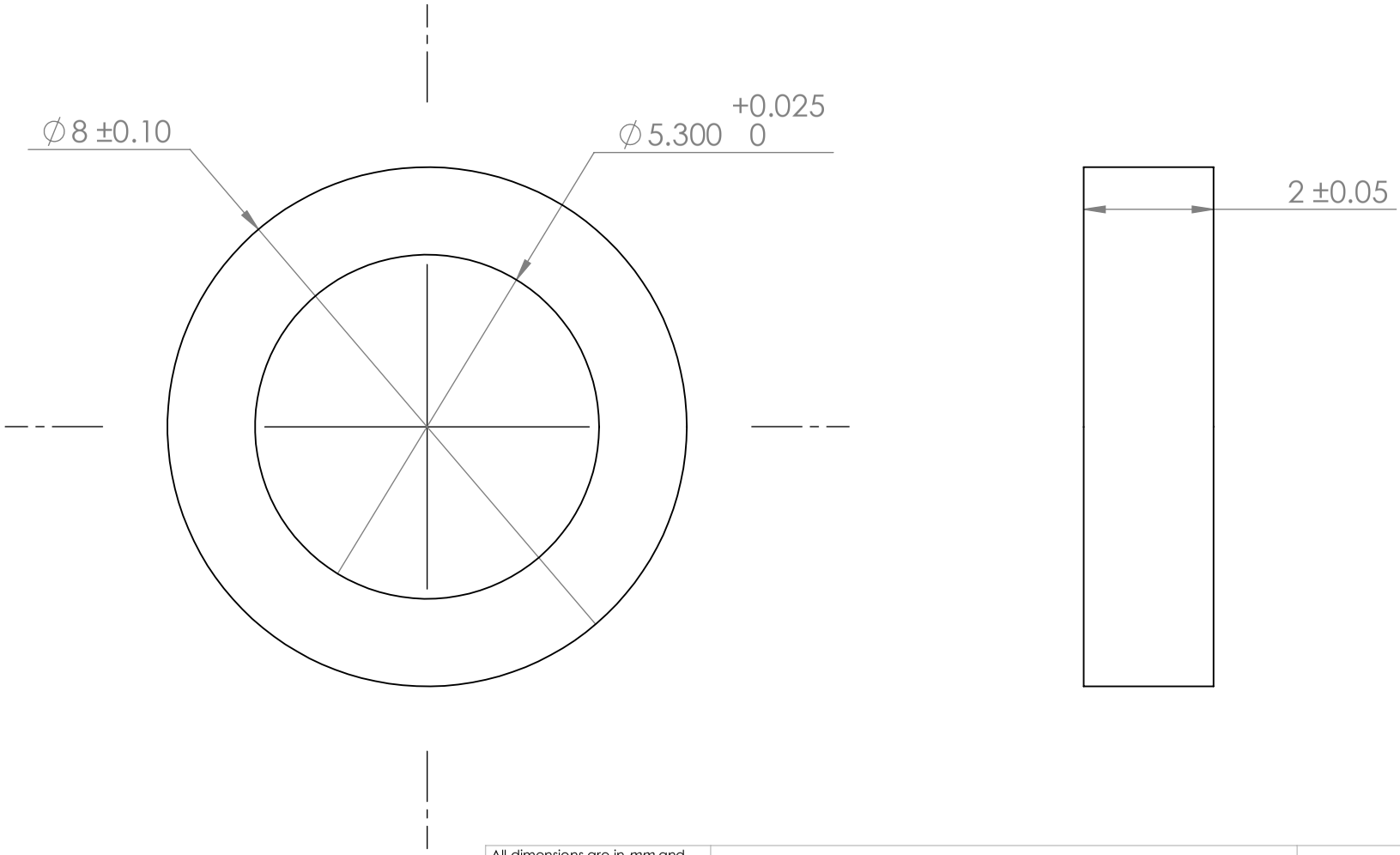

PROPRIETARY AND CONFIDENTIAL

THE INFORMATION CONTAINED IN THIS DRAWING IS THE SOLE PROPERTY OF MIT MEDIA LAB BIOMECHATRONICS. ANY REPRODUCTION IN PART OR AS A WHOLE WITHOUT THE WRITTEN PERMISSION OF MIT MEDIA LAB BIOMECHATRONICS IS PROHIBITED.

All dimensions are in *mm* and apply to finished (after plating) parts unless noted otherwise.

Break all sharp corners 0.25 max

Metric	[Inch]
.0 ± .2	.0 ± .01
.00 ± .1	.00 ± .005
.000 ± .02	.000 ± .001
	.0000 +.0005/-0.0

biomechatronics

Massachussetts Institute of Technology
Media Lab Biomechatronics
75 Amherst St. Room E14-374N
Cambridge, MA 02142
+1 (617)680-0048
emrogers@mit.edu

This Drawing is the property of MIT Media Lab Biomechatronics, and can not be reproduced without the expressed written consent of MIT Media Lab Biomechatronics.

11/2/2021

Scale 10:1

Sheet 1 of 1

VSA04_01_011_insertB

Rev - A-01

Material: 4140 PH Alloy Steel

SOLIDWORKS Educational Product. For Instructional Use Only.

REVISIONS				
ZONE	REV.	DESCRIPTION	DATE	APPROVED

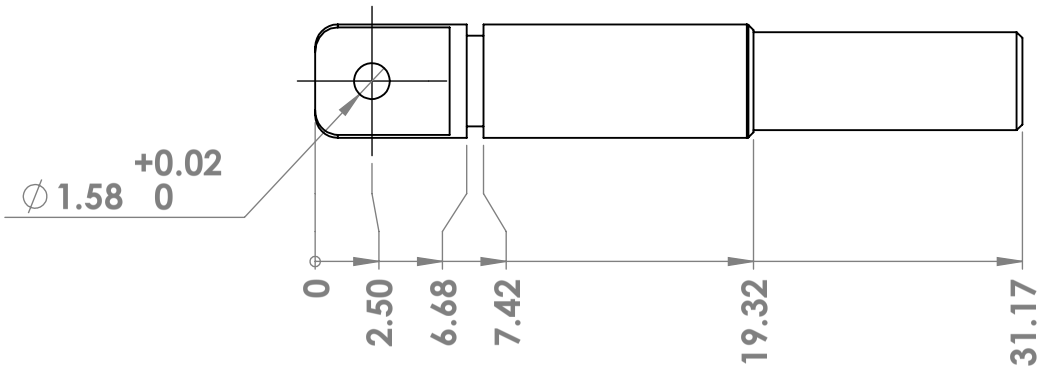

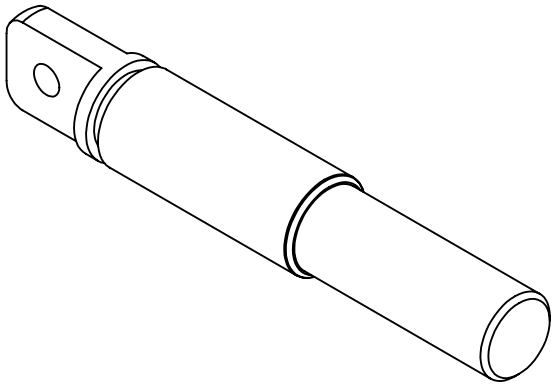

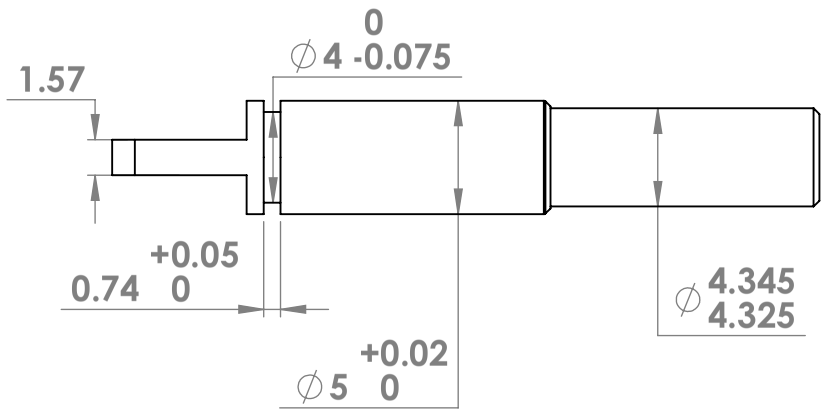

PROPRIETARY AND CONFIDENTIAL
THE INFORMATION CONTAINED IN THIS DRAWING IS THE SOLE PROPERTY OF MIT MEDIA LAB BIOMECHATRONICS. ANY REPRODUCTION IN PART OR AS A WHOLE WITHOUT THE WRITTEN PERMISSION OF MIT MEDIA LAB BIOMECHATRONICS IS PROHIBITED.

All dimensions are in *mm* and apply to finished (after plating) parts unless noted otherwise.

Break all sharp corners 0.25 max

Metric	[Inch]
.0 ± .2	.0 ± .01
.00 ± .1	.00 ± .005
.000 ± .02	.000 ± .001
	.0000 +.0005 / -0.0

biomechatronics

Massachussetts Institute of Technology
Media Lab Biomechatronics
75 Amherst St. Room E14-374N
Cambridge, MA 02142
+1 (617)680-0048
emrogers@mit.edu

This Drawing is the property of MIT Media Lab Biomechatronics, and can not be reproduced without the expressed written consent of MIT Media Lab Biomechatronics.

1/9/2023

Scale 2:1

Sheet 1 of 1

VSA04_01_016_shaft1

Rev - A-01

Material: 4140 Alloy Steel

SOLIDWORKS Educational Product. For Instructional Use Only.

REVISIONS				
ZONE	REV.	DESCRIPTION	DATE	APPROVED

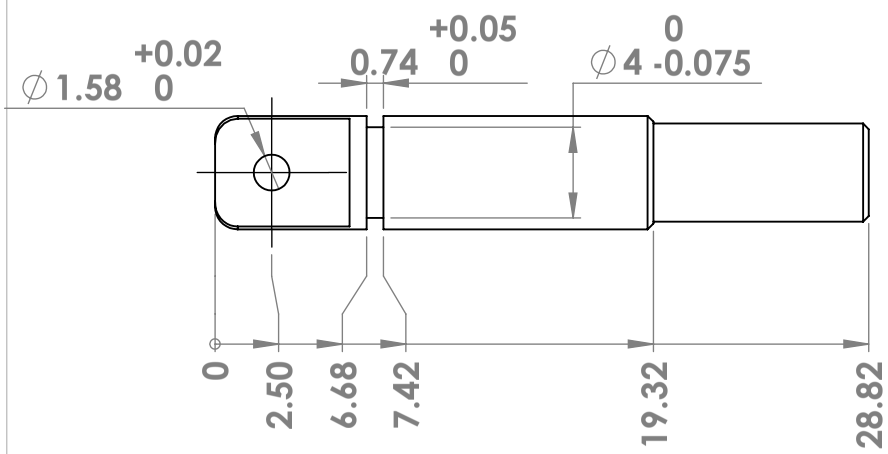

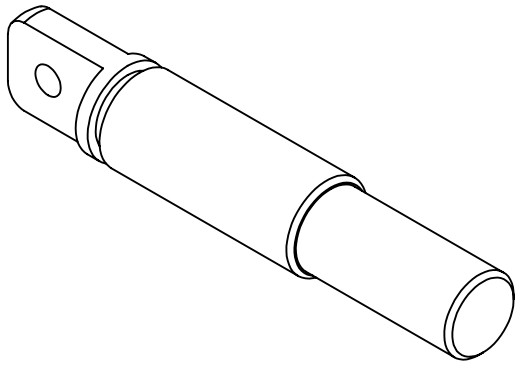

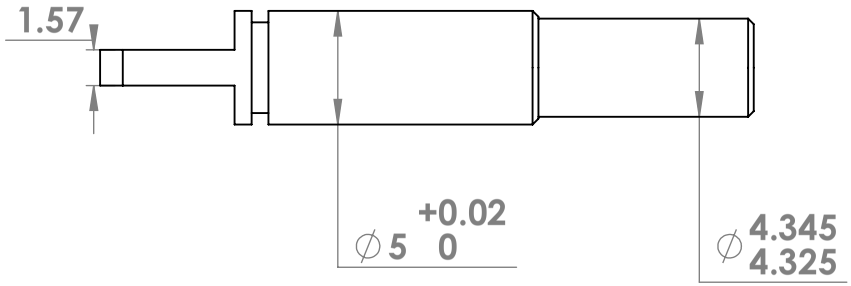

PROPRIETARY AND CONFIDENTIAL
THE INFORMATION CONTAINED IN THIS DRAWING IS THE SOLE PROPERTY OF MIT MEDIA LAB BIOMECHATRONICS. ANY REPRODUCTION IN PART OR AS A WHOLE WITHOUT THE WRITTEN PERMISSION OF MIT MEDIA LAB BIOMECHATRONICS IS PROHIBITED.

All dimensions are in *mm* and apply to finished (after plating) parts unless noted otherwise.

Break all sharp corners 0.25 max

Metric	[Inch]
.0 ± .2	.0 ± .01
.00 ± .1	.00 ± .005
.000 ± .02	.000 ± .001
	.0000 +.0005/-0.0

biomechatronics

Massachussetts Institute of Technology
Media Lab Biomechatronics
75 Amherst St. Room E14-374N
Cambridge, MA 02142
+1 (617)680-0048
emrogers@mit.edu

This Drawing is the property of MIT Media Lab Biomechatronics, and can not be reproduced without the expressed written consent of MIT Media Lab Biomechatronics.

1/9/2023

Scale 2:1

Sheet 1 of 1

VSA04_01_017_shaft2

Rev - A-01

Material: 4140 Alloy Steel

SOLIDWORKS Educational Product. For Instructional Use Only.

REVISIONS				
ZONE	REV.	DESCRIPTION	DATE	APPROVED

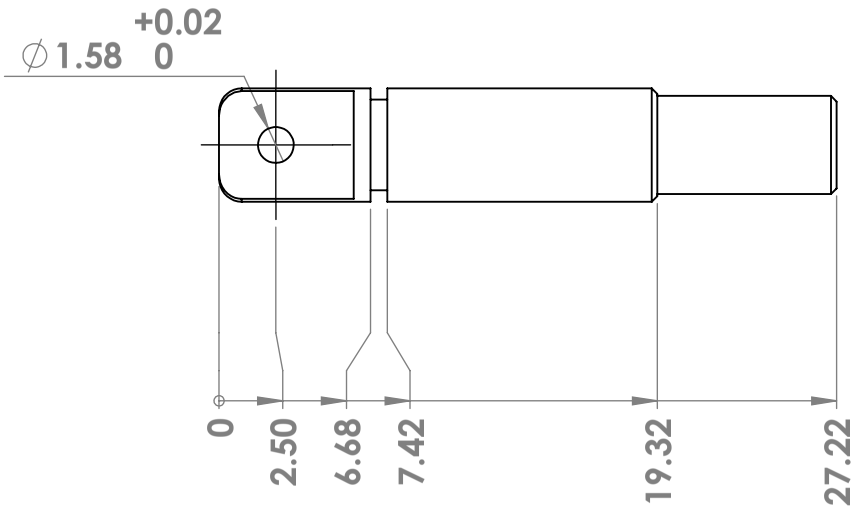

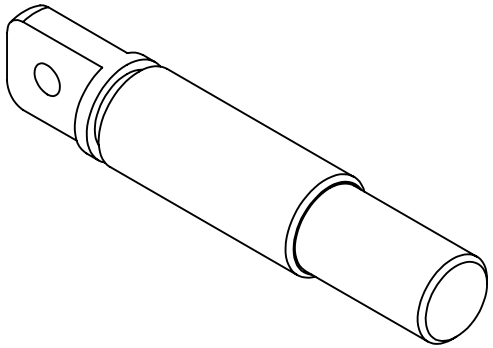

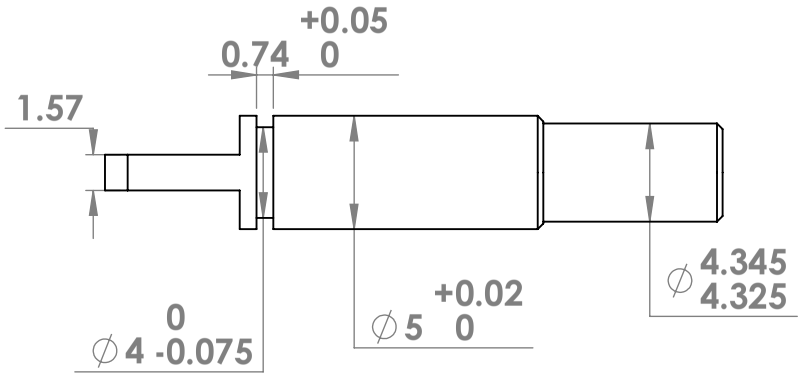

PROPRIETARY AND CONFIDENTIAL
THE INFORMATION CONTAINED IN THIS DRAWING IS THE SOLE PROPERTY OF MIT MEDIA LAB BIOMECHATRONICS. ANY REPRODUCTION IN PART OR AS A WHOLE WITHOUT THE WRITTEN PERMISSION OF MIT MEDIA LAB BIOMECHATRONICS IS PROHIBITED.

All dimensions are in *mm* and apply to finished (after plating) parts unless noted otherwise.

Break all sharp corners 0.25 max

Metric	[Inch]
.0 ± .2	.0 ± .01
.00 ± .1	.00 ± .005
.000 ± .02	.000 ± .001
	.0000 +.0005/-0.0

biomechatronics

Massachussetts Institute of Technology
Media Lab Biomechatronics
75 Amherst St. Room E14-374N
Cambridge, MA 02142
+1 (617)680-0048
emrogers@mit.edu

This Drawing is the property of MIT Media Lab Biomechatronics, and can not be reproduced without the expressed written consent of MIT Media Lab Biomechatronics.

1/9/2023

Scale 2:1

Sheet 1 of 1

VSA04_01_018_shaft3

Rev - A-01

Material: 4140 Alloy Steel

SOLIDWORKS Educational Product. For Instructional Use Only.

REVISIONS				
ZONE	REV.	DESCRIPTION	DATE	APPROVED

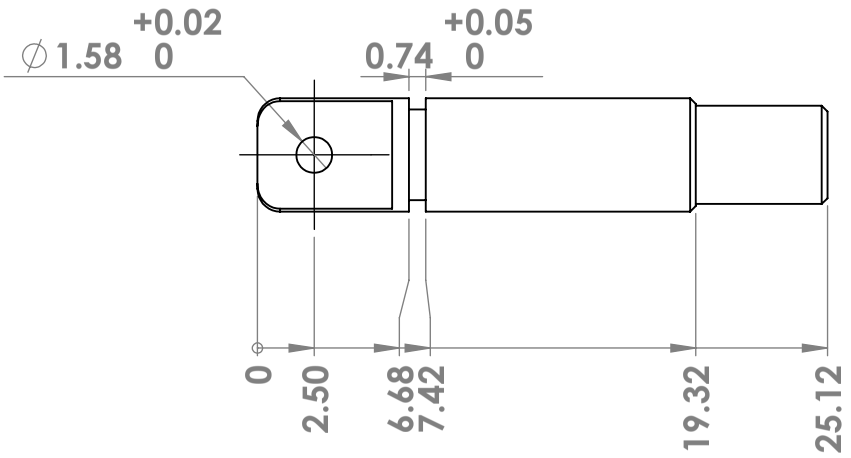

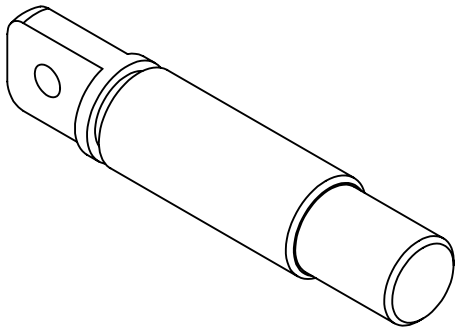

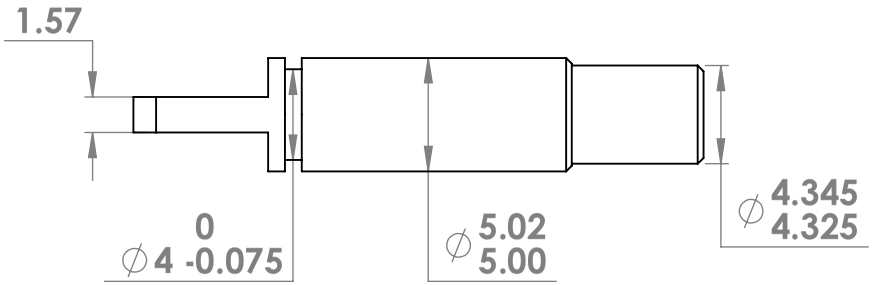

PROPRIETARY AND CONFIDENTIAL
THE INFORMATION CONTAINED IN THIS DRAWING IS THE SOLE PROPERTY OF MIT MEDIA LAB BIOMECHATRONICS. ANY REPRODUCTION IN PART OR AS A WHOLE WITHOUT THE WRITTEN PERMISSION OF MIT MEDIA LAB BIOMECHATRONICS IS PROHIBITED.

All dimensions are in *mm* and apply to finished (after plating) parts unless noted otherwise.

Break all sharp corners 0.25 max

Metric	[Inch]
.0 ± .2	.0 ± .01
.00 ± .1	.00 ± .005
.000 ± .02	.000 ± .001
	.0000 +.0005/-0.0

biomechatronics

Massachussetts Institute of Technology
Media Lab Biomechatronics
75 Amherst St. Room E14-374N
Cambridge, MA 02142
+1 (617)680-0048
emrogers@mit.edu

This Drawing is the property of MIT Media Lab Biomechatronics, and can not be reproduced without the expressed written consent of MIT Media Lab Biomechatronics.

1/9/2023

Scale 5:1

Sheet 1 of 1

VSA04_01_019_shaft4

Rev - A-01

Material: 4140 Alloy Steel

SOLIDWORKS Educational Product. For Instructional Use Only.

REVISIONS				
ZONE	REV.	DESCRIPTION	DATE	APPROVED

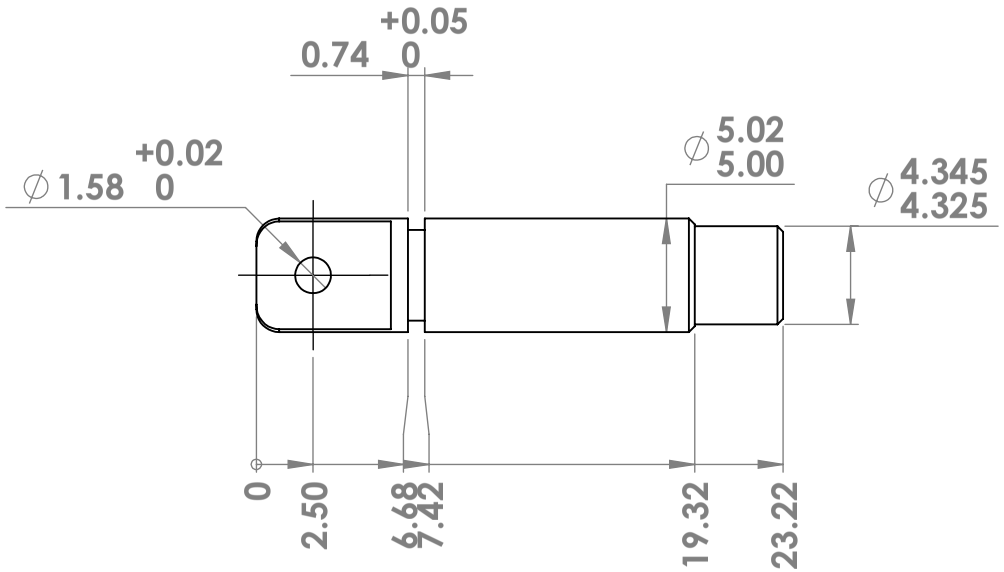

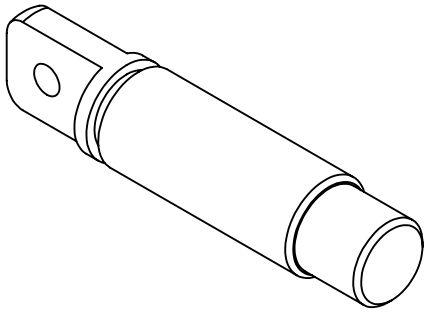

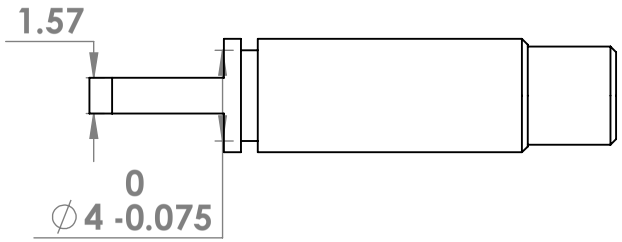

PROPRIETARY AND CONFIDENTIAL
THE INFORMATION CONTAINED IN THIS DRAWING IS THE SOLE PROPERTY OF MIT MEDIA LAB BIOMECHATRONICS. ANY REPRODUCTION IN PART OR AS A WHOLE WITHOUT THE WRITTEN PERMISSION OF MIT MEDIA LAB BIOMECHATRONICS IS PROHIBITED.

All dimensions are in *mm* and apply to finished (after plating) parts unless noted otherwise.

Break all sharp corners 0.25 max

Metric	[Inch]
.0 ± .2	.0 ± .01
.00 ± .1	.00 ± .005
.000 ± .02	.000 ± .001
	.0000 +.0005/-0.0

biomechatronics

Massachussetts Institute of Technology
Media Lab Biomechatronics
75 Amherst St. Room E14-374N
Cambridge, MA 02142
+1 (617)680-0048
emrogers@mit.edu

This Drawing is the property of MIT Media Lab Biomechatronics, and can not be reproduced without the expressed written consent of MIT Media Lab Biomechatronics.

1/9/2023

Scale 5:1

Sheet 1 of 1

VSA04_01_020_shaft5

Rev - A-01

Material: 4140 Alloy Steel

SOLIDWORKS Educational Product. For Instructional Use Only.

REVISIONS				
ZONE	REV.	DESCRIPTION	DATE	APPROVED

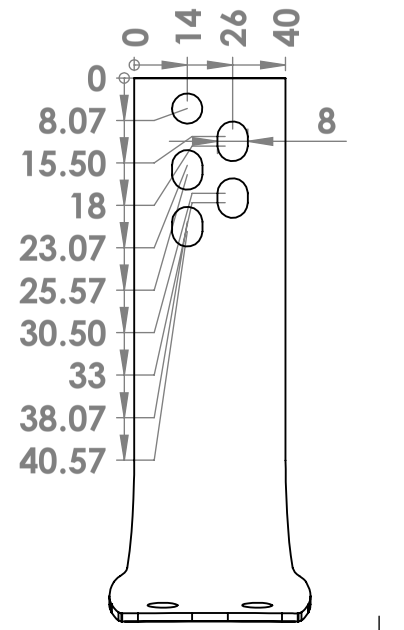

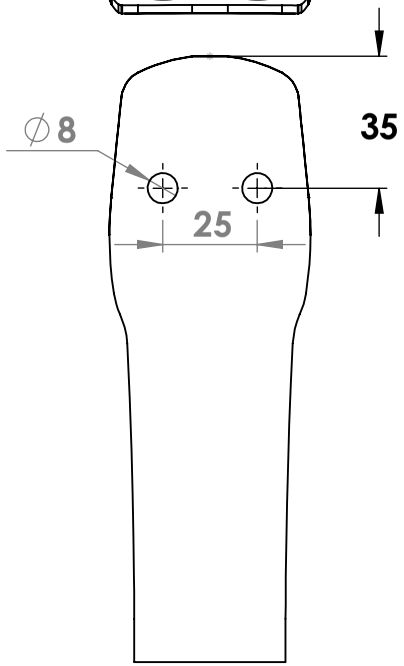

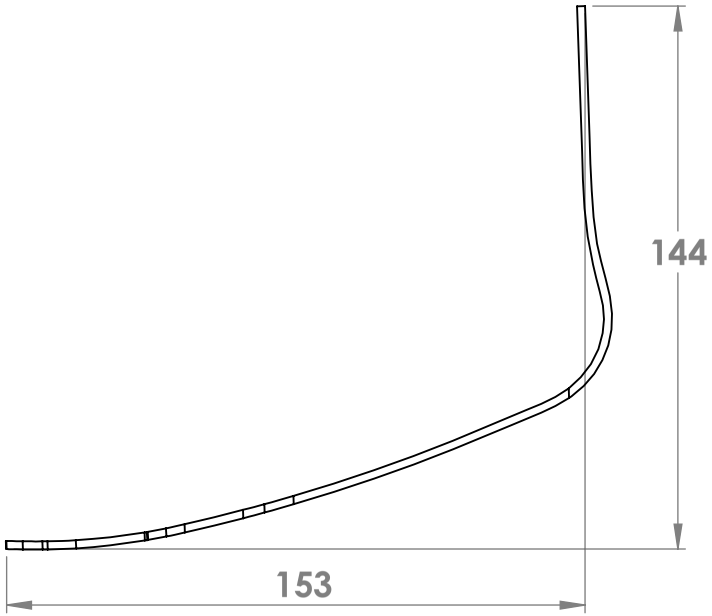

PROPRIETARY AND CONFIDENTIAL
THE INFORMATION CONTAINED IN THIS DRAWING IS THE SOLE PROPERTY OF MIT MEDIA LAB BIOMECHATRONICS. ANY REPRODUCTION IN PART OR AS A WHOLE WITHOUT THE WRITTEN PERMISSION OF MIT MEDIA LAB BIOMECHATRONICS IS PROHIBITED.

All dimensions are in *mm* and apply to finished (after plating) parts unless noted otherwise.

Break all sharp corners 0.25 max

Metric	[Inch]
.0 ± .2	.0 ± .01
.00 ± .1	.00 ± .005
.000 ± .02	.000 ± .001
	.0000 +.0005/-0.0

biomechatronics

Massachussetts Institute of Technology
Media Lab Biomechatronics
75 Amherst St. Room E14-374N
Cambridge, MA 02142
+1 (617)680-0048
emrogers@mit.edu

This Drawing is the property of MIT Media Lab Biomechatronics, and can not be reproduced without the expressed written consent of MIT Media Lab Biomechatronics.

1/9/2023

Scale 1:2

Sheet 1 of 1

VSA04_01_021_spring1

Rev - A-01

Material: UD Carbon Fiber Composite

SOLIDWORKS Educational Product. For Instructional Use Only.

REVISIONS				
ZONE	REV.	DESCRIPTION	DATE	APPROVED

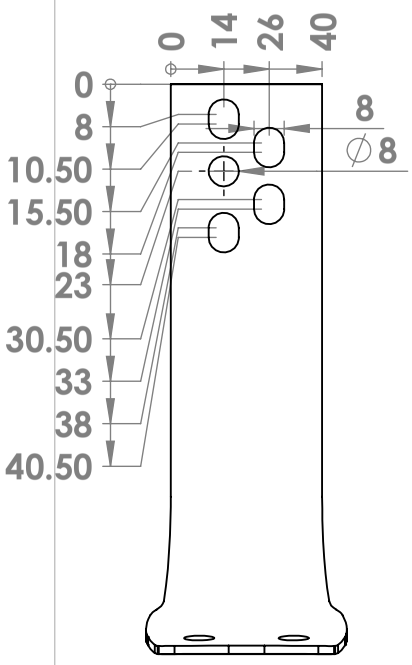

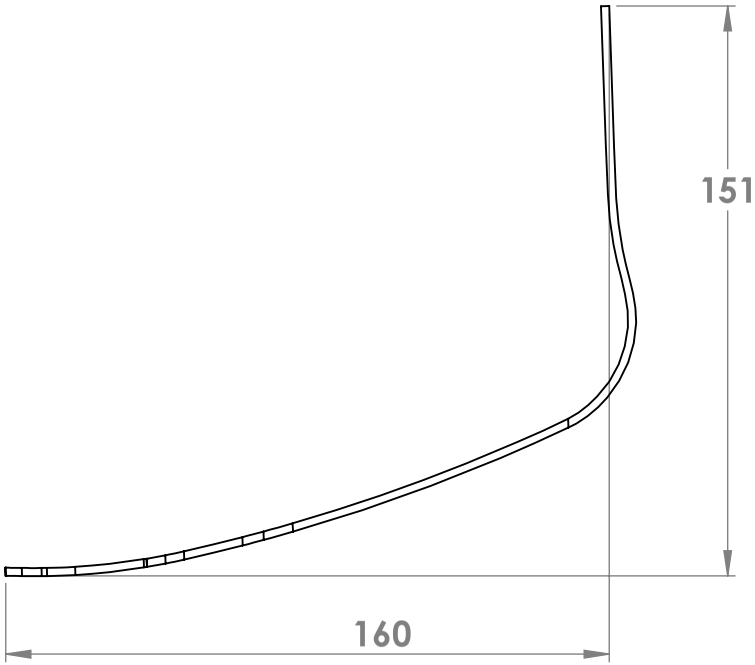

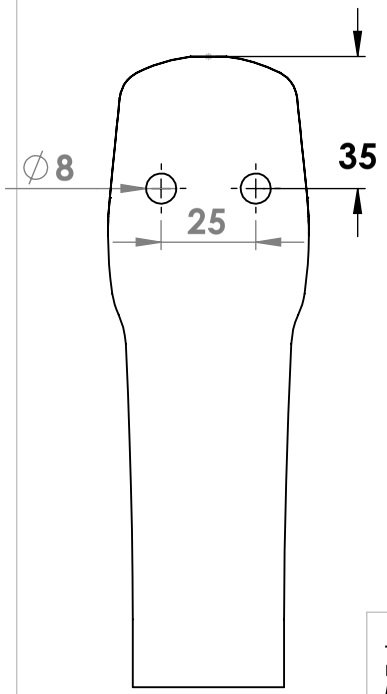

PROPRIETARY AND CONFIDENTIAL
THE INFORMATION CONTAINED IN THIS DRAWING IS THE SOLE PROPERTY OF MIT MEDIA LAB BIOMECHATRONICS. ANY REPRODUCTION IN PART OR AS A WHOLE WITHOUT THE WRITTEN PERMISSION OF MIT MEDIA LAB BIOMECHATRONICS IS PROHIBITED.

All dimensions are in *mm* and apply to finished (after plating) parts unless noted otherwise.

Break all sharp corners 0.25 max

Metric	[Inch]
.0 ± .2	.0 ± .01
.00 ± .1	.00 ± .005
.000 ± .02	.000 ± .001
	.0000 +.0005/−0.0

biomechatronics

Massachussetts Institute of Technology
Media Lab Biomechatronics
75 Amherst St. Room E14-374N
Cambridge, MA 02142
+1 (617)680-0048
emrogers@mit.edu

This Drawing is the property of MIT Media Lab Biomechatronics, and can not be reproduced without the expressed written consent of MIT Media Lab Biomechatronics.

1/9/2023

Scale 1:2

Sheet 1 of 1

VSA04_01_022_spring2

Rev - A-01

Material: UD Carbon Fiber Composite

Finish:

SOLIDWORKS Educational Product. For Instructional Use Only.

REVISIONS				
ZONE	REV.	DESCRIPTION	DATE	APPROVED

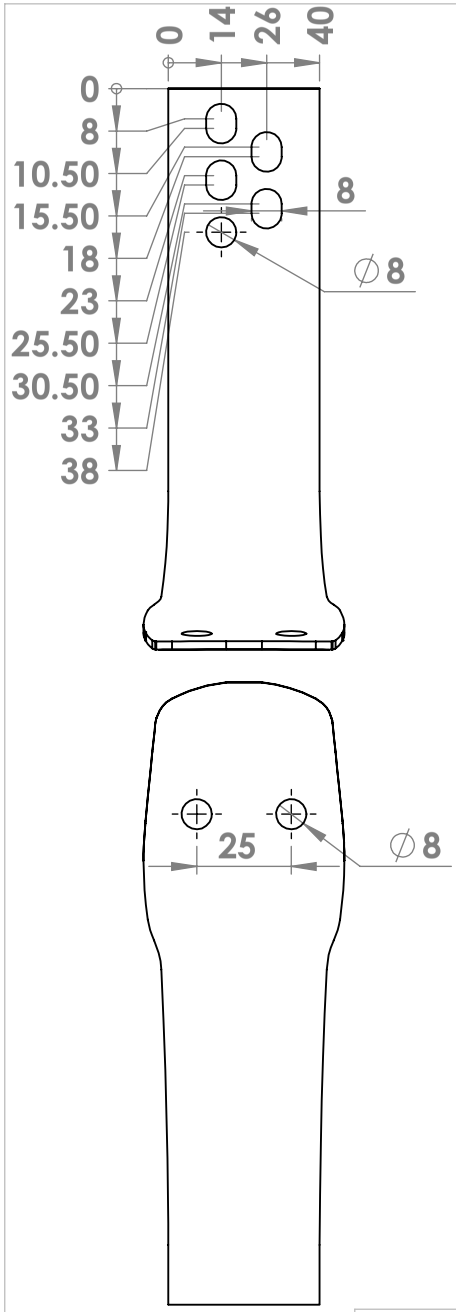

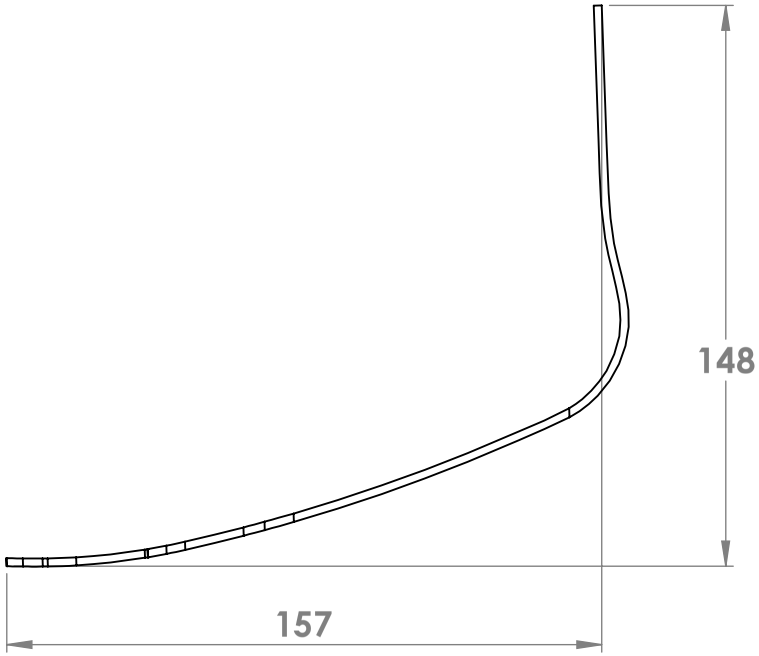

PROPRIETARY AND CONFIDENTIAL
THE INFORMATION CONTAINED IN THIS DRAWING IS THE SOLE PROPERTY OF MIT MEDIA LAB BIOMECHATRONICS. ANY REPRODUCTION IN PART OR AS A WHOLE WITHOUT THE WRITTEN PERMISSION OF MIT MEDIA LAB BIOMECHATRONICS IS PROHIBITED.

All dimensions are in *mm* and apply to finished (after plating) parts unless noted otherwise.

Break all sharp corners 0.25 max

Metric	[Inch]
.0 ± .2	.0 ± .01
.00 ± .1	.00 ± .005
.000 ± .02	.000 ± .001
	.0000 +.0005/-0.0

biomechatronics

Massachussetts Institute of Technology
Media Lab Biomechatronics
75 Amherst St. Room E14-374N
Cambridge, MA 02142
+1 (617)680-0048
emrogers@mit.edu

This Drawing is the property of MIT Media Lab Biomechatronics, and can not be reproduced without the expressed written consent of MIT Media Lab Biomechatronics.

1/9/2023

Scale 1:2

Sheet 1 of 1

VSA04_01_023_spring3

Rev - A-01

Material: UD Carbon Fiber Composite

SOLIDWORKS Educational Product. For Instructional Use Only.

REVISIONS				
ZONE	REV.	DESCRIPTION	DATE	APPROVED

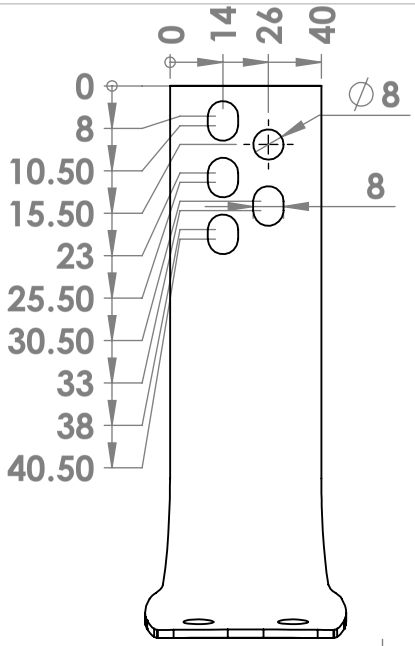

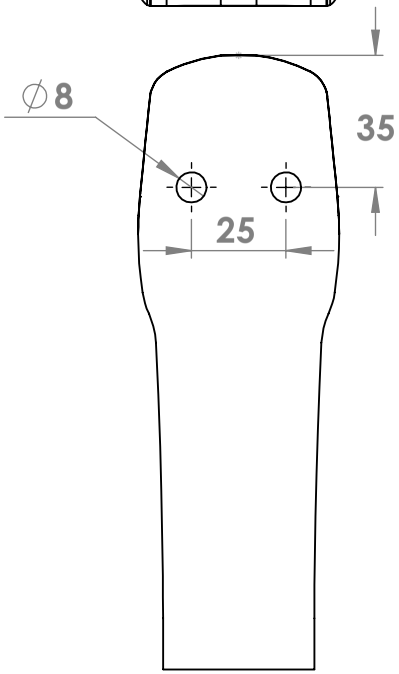

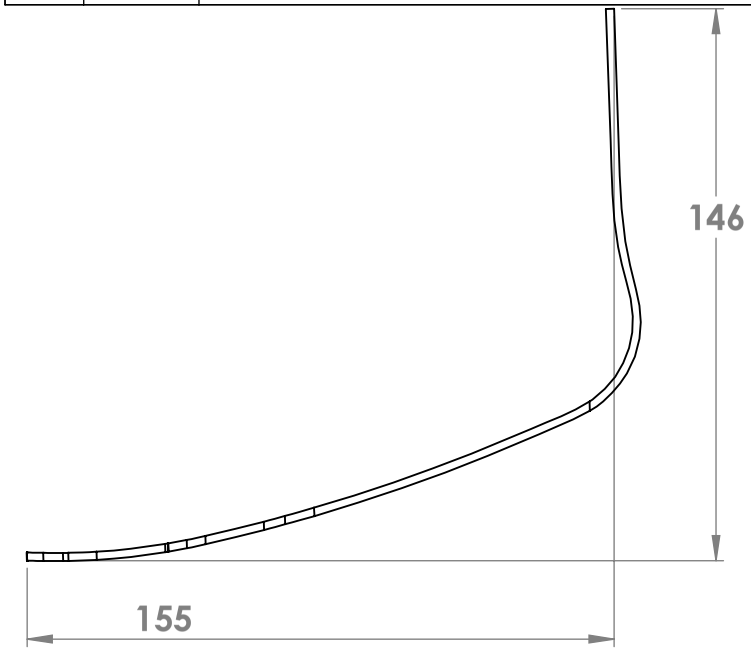

PROPRIETARY AND CONFIDENTIAL
THE INFORMATION CONTAINED IN THIS DRAWING IS THE SOLE PROPERTY OF MIT MEDIA LAB BIOMECHATRONICS. ANY REPRODUCTION IN PART OR AS A WHOLE WITHOUT THE WRITTEN PERMISSION OF MIT MEDIA LAB BIOMECHATRONICS IS PROHIBITED.

All dimensions are in *mm* and apply to finished (after plating) parts unless noted otherwise.

Break all sharp corners 0.25 max

Metric	[Inch]
.0 ± .2	.0 ± .01
.00 ± .1	.00 ± .005
.000 ± .02	.000 ± .001
	.0000 +.0005/-0.0

biomechatronics

Massachussetts Institute of Technology
Media Lab Biomechatronics
75 Amherst St. Room E14-374N
Cambridge, MA 02142
+1 (617)680-0048
emrogers@mit.edu

This Drawing is the property of MIT Media Lab Biomechatronics, and can not be reproduced without the expressed written consent of MIT Media Lab Biomechatronics.

1/9/2023

Scale 1:2

Sheet 1 of 1

VSA04_01_024_spring4

Rev - A-01

Material: UD Carbon Fiber Composite

SOLIDWORKS Educational Product. For Instructional Use Only.

REVISIONS				
ZONE	REV.	DESCRIPTION	DATE	APPROVED

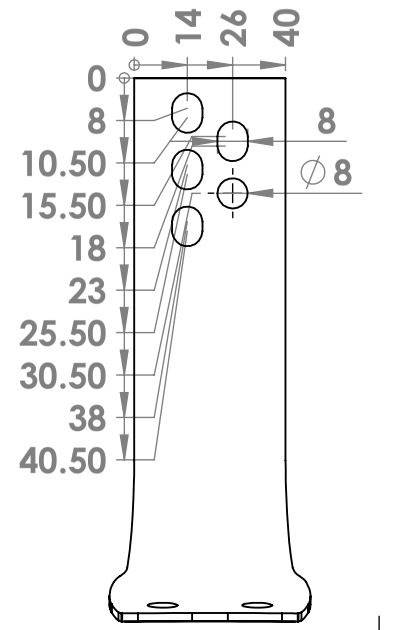

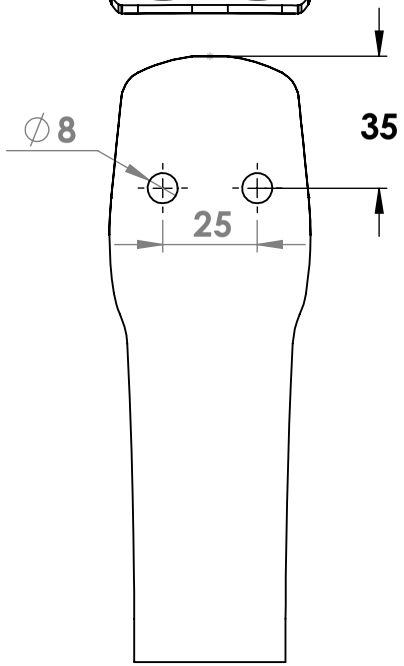

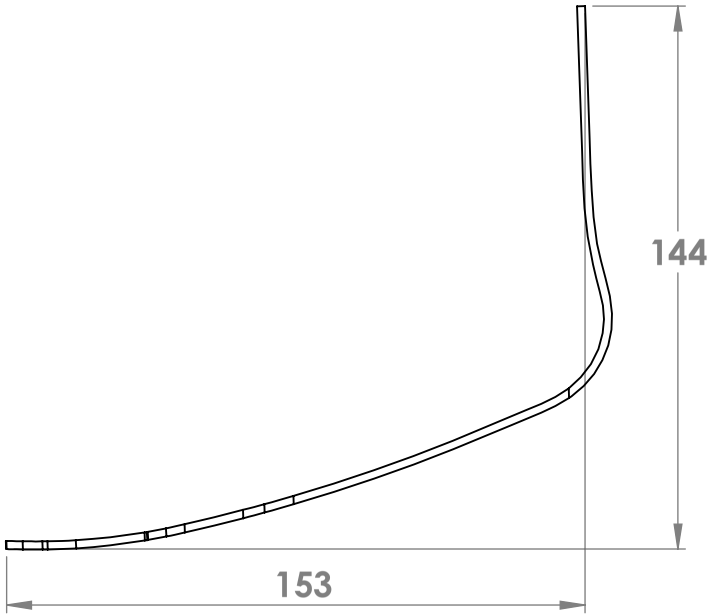

PROPRIETARY AND CONFIDENTIAL
THE INFORMATION CONTAINED IN THIS DRAWING IS THE SOLE PROPERTY OF MIT MEDIA LAB BIOMECHATRONICS. ANY REPRODUCTION IN PART OR AS A WHOLE WITHOUT THE WRITTEN PERMISSION OF MIT MEDIA LAB BIOMECHATRONICS IS PROHIBITED.

All dimensions are in *mm* and apply to finished (after plating) parts unless noted otherwise.

Break all sharp corners 0.25 max

Metric	[Inch]
.0 ± .2	.0 ± .01
.00 ± .1	.00 ± .005
.000 ± .02	.000 ± .001
	.0000 +.0005/-0.0

biomechatronics

Massachussetts Institute of Technology
Media Lab Biomechatronics
75 Amherst St. Room E14-374N
Cambridge, MA 02142
+1 (617)680-0048
emrogers@mit.edu

This Drawing is the property of MIT Media Lab Biomechatronics, and can not be reproduced without the expressed written consent of MIT Media Lab Biomechatronics.

1/9/2023

Scale 1:2

Sheet 1 of 1

VSA04_01_025_spring5

Rev - A-01

Material: UD Carbon Fiber Composite

SOLIDWORKS Educational Product. For Instructional Use Only.

REVISIONS				
ZONE	REV.	DESCRIPTION	DATE	APPROVED

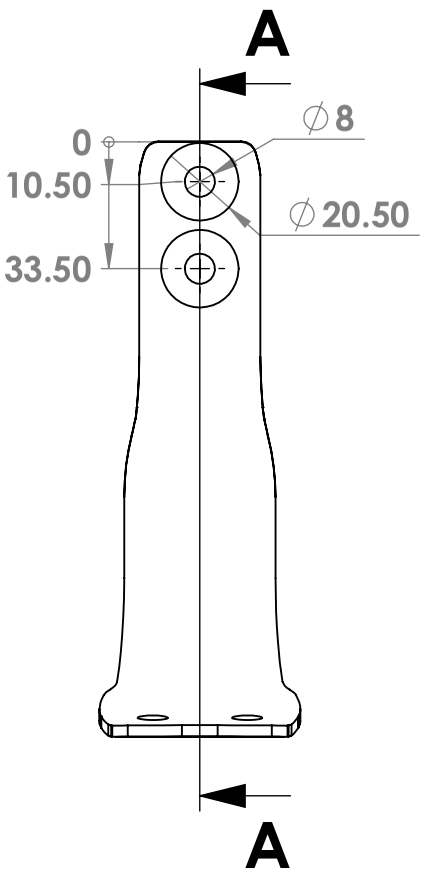

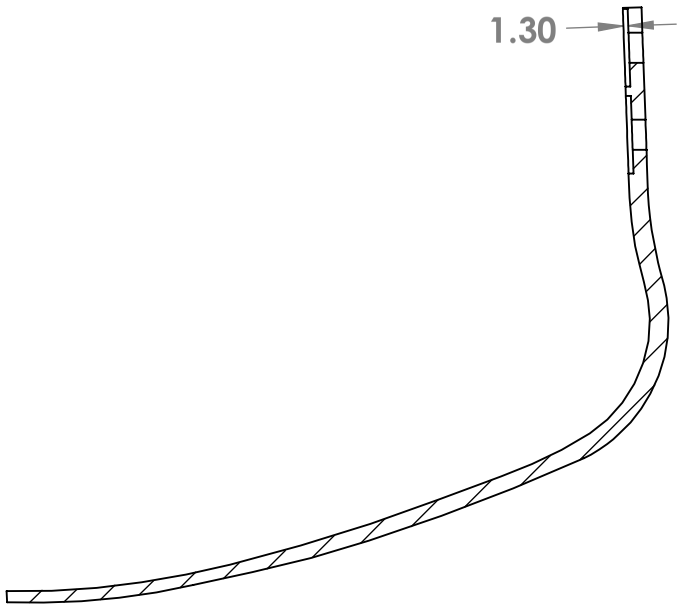

SECTION A-A

PROPRIETARY AND CONFIDENTIAL
THE INFORMATION CONTAINED IN THIS DRAWING IS THE SOLE PROPERTY OF MIT MEDIA LAB BIOMECHATRONICS. ANY REPRODUCTION IN PART OR AS A WHOLE WITHOUT THE WRITTEN PERMISSION OF MIT MEDIA LAB BIOMECHATRONICS IS PROHIBITED.

All dimensions are in *mm* and apply to finished (after plating) parts unless noted otherwise.

Break all sharp corners 0.25 max

Metric	[Inch]
.0 ± .2	.0 ± .01
.00 ± .1	.00 ± .005
.000 ± .02	.000 ± .001
	.0000 +.0005/-0.0

biomechatronics

Massachussetts Institute of Technology
Media Lab Biomechatronics
75 Amherst St. Room E14-374N
Cambridge, MA 02142
+1 (617)680-0048
emrogers@mit.edu

This Drawing is the property of MIT Media Lab Biomechatronics, and can not be reproduced without the expressed written consent of MIT Media Lab Biomechatronics.

1/9/2023

Scale 1:2

Sheet 1 of 1

VSA04_01_026_spring6

Rev - A-01

Material: UD Carbon Fiber Composite

SOLIDWORKS Educational Product. For Instructional Use Only.

Appendix B

Appendix B

B.1 Bill of Materials

Table B.1: Bill of Materials.

Component	**Qty**	**Vendor**	**Part number**	**Description**
Housing back	1	Custom	VSA04-01-001-housingback	
Pyramid	1	Custom	VSA04-01-002-pyramid	
Actuator housing	5	Custom	VSA04-01-003-actuatorhousing	
Housing front	1	Custom	VSA04-01-010-housingfront	
Insert	5	Custom	VSA04-01-011-insert	
Shaft 1	1	Custom	VSA04-01-016-shaft1	
Shaft 2	1	Custom	VSA04-01-017-shaft2	
Shaft 3	1	Custom	VSA04-01-018-shaft3	
Shaft 4	1	Custom	VSA04-01-019-shaft4	
Shaft 5	1	Custom	VSA04-01-020-shaft5	
Spring 1	1	Custom	VSA04-01-021-spring1	
Spring 2	1	Custom	VSA04-01-022-spring2	
Spring 3	1	Custom	VSA04-01-023-spring3	
Spring 4	1	Custom	VSA04-01-024-spring4	
Spring 5	1	Custom	VSA04-01-025-spring5	
Spring 6	1	Custom	VSA04-01-026-spring6	
Shoulder Screw	5	McMaster	91829A750	Pin attachment
Ledex Solenoid	5	Ledex	151094-234	Solenoid
Weld nuts	4	McMaster	90563A620	
Alloy Steel, M6 x 1.00 mm, 22 mm Long	2	McMaster	91239A324	Toe connection
Alloy Steel, M6 x 1.00 mm, 12 mm Long	2	McMaster	91239A318	Ground spring
Black-Oxide, M6 x 1 mm Thread, 20 mm Long	1	McMaster	91290A326	Pyramid bolted joint
Belville washer	1	McMaster	97125K123	pyramid bolted joint
Shoulder Screw 7/32" Diameter	4	McMaster	91259A421	Housing bolts
Belville washer	8	McMaster	9713K64	Housing bolted joint
iglidur P210, sleeve bearing	5	igus	P210SM-0507-10	Actuator bushing
0-80 Hex Nut	5	McMaster	90730A001	actuator nut
Polyurethane washer	5	McMaster	93650A110	Actuator hard stop
Retaining ring	5	McMaster	98543A112	
Strain gauge	1	Micromeasurements	CEA-06-250UTA-350	Strain gauge
350vOhm Resistor	2	Mouser	279-UPF50B350RV	resistor
DP 420 Epoxy	1	McMaster	7467A51	Structual epoxy

Appendix C

Appendix C

C.1 Parametric Model

```
% Stiffness Model
% Castigliano's Thm
% Shigley's ch 4-4 & 4-5
% Emily Rogers 03/25/2020

%% Parallel springs

E=70*10^9;
F=700;
L2=.12;
L1=.08;
G=5*10^9;
C=1.2;
R=.019;
ro=.01986;
ri=.01814;
b=.04;
h = .001742; % section thickness
```

```
A=b*h;
I=(b*h^3)/12; % area moment of inertia of thin springs
rn=h/log(ro/ri);
e=((rn+ri)/2)-rn;

%% bending moment
fun= @(theta) (1./(A.*E.*e)).*(F.*((R.*sin(theta)+L2).^2));
delta_1_bc = integral(fun,0, pi/2);
delta_1_cd = (1./(3.*E.*I)).*(F.*L2.^3);
delta_1_ab = (1./(2.*E.*I)).*(F.*(L2+R).*L1.^2);

%% axial load
fun= @(theta) (R./(A.*E)).*(F.*(sin(theta)).^2);
delta_2_bc = integral(fun,0, pi/2);
delta_2_ab = (F*L1)/(A*E); % shigley eq 4-29

%% coupling term
fun= @(theta) -(1./(A.*E)).*(2.*F.*R.*(sin(theta)).^2);
delta_3_bc = integral(fun,0, pi/2);

%% transverse shear
fun= @(theta) ((C.*R.*F.*cos(theta))./(A.*G)).*(cos(theta));
delta_4_bc = integral(fun,0, pi/2);

%% Total deflection parallel springs
delta_bc=delta_1_bc+delta_2_bc+delta_3_bc+delta_4_bc;
delta_ab=delta_1_ab+delta_2_ab;
delta_cd=delta_1_cd;
delta_parallel=delta_ab+delta_bc+delta_cd;
k_parallel=F/delta_parallel;
```

```
%% Ground spring

 R2=.021;
 ro2=.023;
 ri2=.019;
 b2=.04;
 h2 = .004; % section thickness
 A2=b2*h2;
 I2=(b2*h2.^3)/12; % area moment of inertia of thin springs
 rn2=h2/log(ro2/ri2);
 e2=((rn2+ri2)/2)-rn;

%% Bending
% A varies w/ cross section A(x)=b*(.004+.001.*(x./L2))
fun= @(x) (1./(2.*E.*((b2.*(.004+.001.*(x./L1)).^3)./12))).*(F.*(L2+R2).*L1.^2);
delta_1_ground_ab = integral(fun,0, L1);
fun= @(theta) (1./(A2.*E.*e2)).*(F.*((R2.*sin(theta)+L2).^2));
delta_1_ground_bc = integral(fun,0, pi/2) ;
fun= @(x) (1./(E.*((b2.*(.003+.001.*(x./L2)).^3)./12))).*(F.*(x).^2);
delta_1_ground_cd = integral(fun,0, L2);

%% axial load
fun= @(x) (F.*L2)./(b2.*(.004+.001.*(x./L1)).*E); % shigley eq 4-29
delta_2_ground_ab = integral(fun,0, L1);
fun= @(theta) (R2./(A2.*E)).*(F.*(sin(theta)).^2);
delta_2_ground_bc = integral(fun,0, pi/2);

%% coupling term
fun= @(theta) -(1./(A2.*E)).*(2.*F.*R2.*(sin(theta)).^2);
```

```
delta_3_ground_bc = integral(fun,0, pi/2) ;

%% transverse shear
fun= @(theta) ((C.*R2.*F.*cos(theta))./(A2.*G)).*(cos(theta));
delta_4_ground_bc = integral(fun,0, pi/2);

%% total ground spring
delta_ground_ab=delta_1_ground_ab+delta_2_ground_ab;
delta_ground_bc=delta_1_bc+delta_2_ground_bc+delta_3_ground_bc+delta_4_ground_bc;
delta_ground_cd=delta_1_ground_cd;

delta_ground=delta_ground_ab+delta_ground_bc+delta_ground_cd;
k_ground=F/delta_ground;

%% total stiffness unlocked
k_total=k_ground+5*k_parallel; % total stiffness N/m
lin_deflection=F/k_total;
rot_deflection=asin(lin_deflection/(L2));
rot_k=F*(L2)/rot_deflection;

%% Actuator Stiffness
syms x y z
F=100;
clearance=.0004;
E=210*10^9;
d=.0047;
I=pi*(d^4)/64;
l_shaft=.01;

% k bearing
```

```
E_1=205*10^9; %E steel
v_1=0.29; % v shaft
d_1=5.0;
R_1=d_1/2;
% teflon
E_2=2.5*10^9; %E teflon
v_2=0.4; % v bearing
d_2=-5.068
R_2=-d_2/2;
sigma_yield=50*10^6;
l_bearing=.01;
P=F/l_bearing;
R_c = .001*(1/((1/R_1)+(1/R_2)));
E_c=1/(((1-v_1^2)/E_1)+((1-v_2^2)/E_2));
b=((4*P*R_c)/(pi*E_c))^.5
E_c1=1/(((1-v_1^2)/E_1));
E_c2=1/(+((1-v_2^2)/E_2));
delta_1=((2*P)/(pi*E_c1))*(log(2*d_1/b)-1/2);
delta_2=((2*P)/(pi*E_c2))*(log(2*d_1/b)-(v_1/(2*(1-v_1))));
delta_system=2*(delta_1+delta_2)
k_bearing=F/delta_system
k_rotbearing=(F*(l_bearing/2))/asin((F/k_bearing)/(l_bearing/2));
Pb=[0;0;0;1];
Tbearing=F*(l_shaft+(l_bearing/2));
thetaz_bearing=Tbearing/k_rotbearing;
dy_bearing=F/k_bearing
aHb=rotation(z,thetaz_bearing)
Hb=translation(l_bearing/2,dy_bearing,0);

% shaft deflection
```

```
thetaz_shaft = F*(l_shaft^2)/(2*E*I);
dy_shaft =F*(l_shaft^3)/(3*E*I);
Pc=[l_shaft;0;0;1];
cHc=rotation(z,thetaz_shaft)
Hc=translation(0,dy_shaft,0);

% axial compression of spring
A_spring=(1.75*10^-3)*(40*10^-3);
l_spring=.2;
E_cf=135*10^9;
k_axial=(A_spring*E_cf/l_spring)
dy_spring=F/k_axial
Ph=[0;0;0;1]
He=translation(0,dy_spring,0);

% axial clearance in pin/slot interface
dy_clearance = clearance;
Hf=translation(0,dy_clearance,0);

% deflectionof slot/bushing
E_1=200*10^9; %E steel
v_1=0.27; % v shaft
d_1=.005;
R_1=d_1/2;
E_2=210*10^9; %E steel
v_2=0.27; % v bearing
sigma_yield=1241*10^6;
l=.0025;
d_2=-.0051;
R_2=d_2/2;
```

```
P=F/l;
R_c = 1/((1/R_1)+(1/R_2));
E_c=1/(((1-v_1^2)/E_1)+((1-v_2^2)/E_2));
b=((4*P*R_c)/(pi*E_c))^.5
E_c1=1/(((1-v_1^2)/E_1));
E_c2=1/(+((1-v_2^2)/E_2));
delta_1=((2*P)/(pi*E_c1))*(log(2*d_1/b)-1/2);
delta_2=((2*P)/(pi*E_c2))*(log(2*d_1/b)-(v_1/(2*(1-v_1))));
delta_system=2*(delta_1+delta_2)
k_slot=F/delta_system
Hg=translation(0,delta_system,0);
P=[0;0;0;1]
delta_total=aHb*Hb*cHc*Hc*He*Hf*Hg*P

k_actuator=F/delta_total(2,1)

deflectionratio=(asin(delta_ground/L2)/(2*pi))*(.00173)*2*pi/delta_ground
k_locked=deflectionratio*5*k_actuator+k_total
increase=k_locked/k_total
```

References

[1] K. Ziegler-Graham, E. J. MacKenzie, P. L. Ephraim, T. G. Travison, and R. Brookmeyer, "Estimating the prevalence of limb loss in the united states: 2005 to 2050," *Archives of physical medicine and rehabilitation*, vol. 89, no. 3, pp. 422–429, 2008.

[2] R. Gailey, K. Allen, J. Castles, J. Kucharik, M. Roeder, *et al.*, "Review of secondary physical conditions associated with lower-limb amputation and long-term prosthesis use," *Journal of rehabilitation research and development*, vol. 45, no. 1, p. 15, 2008.

[3] P. A. Struyf, C. M. van Heugten, M. W. Hitters, and R. J. Smeets, "The prevalence of osteoarthritis of the intact hip and knee among traumatic leg amputees," *Archives of physical medicine and rehabilitation*, vol. 90, no. 3, pp. 440–446, 2009.

[4] D. C. Morgenroth, A. D. Segal, K. E. Zelik, J. M. Czerniecki, G. K. Klute, P. G. Adamczyk, M. S. Orendurff, M. E. Hahn, S. H. Collins, and A. D. Kuo, "The effect of prosthetic foot push-off on mechanical loading associated with knee osteoarthritis in lower extremity amputees," *Gait & posture*, vol. 34, no. 4, pp. 502–507, 2011.

[5] H. M. Herr and E. A. Rogers, "Leaf spring with high resolution stiffness control," PCT/US2021/049526, Sept. 2020.

[6] E. Rogers-Bradley, S. H. Yeon, C. Landis, and H. M. Herr, "Design and evaluation of a quasi-passive variable stiffness prosthesis for walking speed adaptation in people with transtibial amputation," *under review*, pp. 1–11, Oct 2022.

[7] M. J. Hsu, D. H. Nielsen, S. J. Lin-Chan, and D. Shurr, "The effects of prosthetic foot design on physiologic measurements, self-selected walking velocity, and physical activity in people with transtibial amputation," *Archives of Physical Medicine and Rehabilitation*, vol. 87, no. 1, pp. 123–129, 2006.

[8] A. E. Ferris, J. M. Aldridge, C. A. Rábago, and J. M. Wilken, "Evaluation of a powered ankle-foot prosthetic system during walking," *Archives of physical medicine and rehabilitation*, vol. 93, no. 11, pp. 1911–1918, 2012.

[9] Ottobock, "Empower." `https://www.ottobockus.com/products/empower-ankle/`. Accessed Oct 26, 2022.

[10] F. Gao, Y. Liu, and W.-H. Liao, "Design of powered ankle-foot prosthesis with nonlinear parallel spring mechanism," *Journal of Mechanical Design*, vol. 140, no. 5, p. 055001, 2018.

[11] A. H. Shultz, B. E. Lawson, and M. Goldfarb, "Variable cadence walking and ground adaptive standing with a powered ankle prosthesis," *IEEE Transactions on Neural Systems and Rehabilitation Engineering*, vol. 24, no. 4, pp. 495–505, 2015.

[12] S. K. Au, J. Weber, and H. M. Herr, "Powered ankle-foot prosthesis improves walking metabolic economy," *IEEE Transactions on robotics*, vol. 25, no. 1, pp. 51–66, 2009.

[13] B. Morrison and D. Topping, "Robotic prosthetic availability analysis an interactive qualifying project report," *Worcester Polytechnic Institute*, 2012.

[14] G. McGimpsey and T. C. Bradford, "Limb prosthetics services and devices," *Bioengineering Institute Center for Neuroprosthetics Worcester Polytechnic Institution*, 2008.

[15] R. C. Browning, J. R. Modica, R. Kram, A. Goswami, *et al.*, "The effects of adding mass to the legs on the energetics and biomechanics of walking," *Medicine and science in sports and exercise*, vol. 39, no. 3, p. 515, 2007.

[16] Ottobock, "Taleo." `https://shop.ottobock.us/Prosthetics/Lower-Limb-Prosthetics/Feet---Mechanical/Taleo/p/1C50`. Accessed Nov 3, 2022.

[17] Fillauer, "Allpro." `https://fillauer.com/allpro/`. Accessed Nov 21, 2022.

[18] Ossur, "Pro flex." `https://www.ossur.com/en-us/prosthetics/feet/pro-flex-xc`. Accessed Nov 20, 2022.

[19] H. Houdijk, D. Wezenberg, L. Hak, and A. G. Cutti, "Energy storing and return prosthetic feet improve step length symmetry while preserving margins of stability in persons with transtibial amputation," *Journal of NeuroEngineering and Rehabilitation*, vol. 15, no. 1, pp. 1–8, 2018.

[20] Össur, "Prioprio foot." `https://www.ossur.com/en-us/prosthetics/feet/proprio-foot`. Accessed Oct 26, 2022.

[21] Fillauer, "Motion foot slx." `https://fillauer.com/products/motion-foot-slx/`. Accessed Oct 26, 2022.

[22] M. K. Shepherd and E. J. Rouse, "The vspa foot: A quasi-passive ankle-foot prosthesis with continuously variable stiffness," *IEEE Transactions on Neural Systems and Rehabilitation Engineering*, vol. 25, no. 12, pp. 2375–2386, 2017.

[23] Ottobock, "Meridium." https://www.ottobockus.com/products/meridium/. Accessed Oct 26, 2022.

[24] Blanchford, "Elan." https://www.blatchfordus.com/products/elan/. Accessed Oct 26, 2022.

[25] E. M. Glanzer and P. G. Adamczyk, "Design and validation of a semi-active variable stiffness foot prosthesis," *IEEE Transactions on Neural Systems and Rehabilitation Engineering*, vol. 26, no. 12, pp. 2351–2359, 2018.

[26] S. H. Collins and A. D. Kuo, "Recycling energy to restore impaired ankle function during human walking," *PLoS one*, vol. 5, no. 2, p. e9307, 2010.

[27] E. A. Rogers, M. E. Carney, S. H. Yeon, T. R. Clites, D. Solav, and H. M. Herr, "An ankle-foot prosthesis for rock climbing augmentation," *IEEE Transactions on Neural Systems and Rehabilitation Engineering*, vol. 29, pp. 41–51, 2021.

[28] D. A. Winter, "Energy generation and absorption at the ankle and knee during fast, natural, and slow cadences.," *Clinical orthopaedics and related research*, no. 175, pp. 147–154, 1983.

[29] M. Sartori, M. Maculan, C. Pizzolato, M. Reggiani, and D. Farina, "Modeling and simulating the neuromuscular mechanisms regulating ankle and knee joint stiffness during human locomotion," *Journal of neurophysiology*, vol. 114, no. 4, pp. 2509–2527, 2015.

[30] D. J. Farris and G. S. Sawicki, "The mechanics and energetics of human walking and running: a joint level perspective," *Journal of The Royal Society Interface*, vol. 9, no. 66, pp. 110–118, 2012.

[31] K. Shamaei, G. S. Sawicki, and A. M. Dollar, "Estimation of quasi-stiffness and propulsive work of the human ankle in the stance phase of walking," *PloS one*, vol. 8, no. 3, p. e59935, 2013.

[32] G. Bovi, M. Rabuffetti, P. Mazzoleni, and M. Ferrarin, "A multiple-task gait analysis approach: kinematic, kinetic and emg reference data for healthy young and adult subjects," *Gait & posture*, vol. 33, no. 1, pp. 6–13, 2011.

[33] M. Vlutters, T. Boonstra, A. C. Schouten, and H. van der Kooij, "Direct measurement of the intrinsic ankle stiffness during standing," *Journal of biomechanics*, vol. 48, no. 7, pp. 1258–1263, 2015.

[34] W. L. Childers and K. Z. Takahashi, "Increasing prosthetic foot energy return affects whole-body mechanics during walking on level ground and slopes," *Scientific reports*, vol. 8, no. 1, pp. 1–12, 2018.

[35] K. E. Zelik, S. H. Collins, P. G. Adamczyk, A. D. Segal, G. K. Klute, D. C. Morgenroth, M. E. Hahn, M. S. Orendurff, J. M. Czerniecki, and A. D. Kuo, "Systematic variation of prosthetic foot spring affects center-of-mass mechanics

and metabolic cost during walking," *IEEE Transactions on Neural Systems and Rehabilitation Engineering*, vol. 19, no. 4, pp. 411–419, 2011.

[36] N. P. Fey, G. K. Klute, and R. R. Neptune, "Altering prosthetic foot stiffness influences foot and muscle function during below-knee amputee walking: a modeling and simulation analysis," *Journal of Biomechanics*, vol. 46, no. 4, pp. 637–644, 2013.

[37] D. C. Norvell, J. M. Czerniecki, G. E. Reiber, C. Maynard, J. A. Pecoraro, and N. S. Weiss, "The prevalence of knee pain and symptomatic knee osteoarthritis among veteran traumatic amputees and nonamputees," *Archives of physical medicine and rehabilitation*, vol. 86, no. 3, pp. 487–493, 2005.

[38] A. Mündermann, C. O. Dyrby, and T. P. Andriacchi, "Secondary gait changes in patients with medial compartment knee osteoarthritis: increased load at the ankle, knee, and hip during walking," *Arthritis & rheumatism*, vol. 52, no. 9, pp. 2835–2844, 2005.

[39] N. Foroughi, R. Smith, and B. Vanwanseele, "The association of external knee adduction moment with biomechanical variables in osteoarthritis: a systematic review," *The Knee*, vol. 16, no. 5, pp. 303–309, 2009.

[40] Z. Ding, H. L. Jarvis, A. N. Bennett, R. Baker, and A. M. Bull, "Higher knee contact forces might underlie increased osteoarthritis rates in high functioning amputees: A pilot study," *Journal of Orthopaedic Research®*, vol. 39, no. 4, pp. 850–860, 2021.

[41] A. M. Grabowski and S. D'Andrea, "Effects of a powered ankle-foot prosthesis on kinetic loading of the unaffected leg during level-ground walking," *Journal of Neuroengineering and Rehabilitation*, vol. 10, no. 1, pp. 1–12, 2013.

[42] D. A. Winter, *Anthropometry*, ch. 4, pp. 82–106. John Wiley & Sons, Ltd, 2009.

[43] A. R. Tilley and H. D. Associates, *The Measure of Man and Woman : Human Factors in Design*. Wiley, revised ed., 2001.

[44] "International organization for standardization: Prosthetics-structural testing of lower-limb prostheses - requirements and test methods," *ISO-10328*, 2016.

[45] R. F. Weir, J. W. Sensinger, and M. Kutz, "Design of artificial arms and hands for prosthetic applications," *Biomedical Engineering and Design Handbook*, vol. 2, pp. 537–598, 2009.

[46] R. D. Budynas and J. K. Nisbett, "Deflection of curved members." Shigley's Mechanical Engineering Design, Section 4.4-4.9, McGraw Hill, New York, NY, 2011.

[47] L. Performance Composites, *Mechanical Properties of Carbon Fibre Composite Materials*. 2009. http://www.performance-composites.com/carbonfibre/mechanicalproperties_2.asp. Accessed Nov 1, 2022.

[48] B. F. Sørensen and S. Goutianos, "Prediction of fatigue limit for unidirectional carbon fibre/epoxy composites," in *IOP Conference Series: Materials Science and Engineering*, vol. 388, p. 012017, IOP Publishing, 2018.

[49] N. Morita, Y. Mino, N. Yoshikawa, and M. Hojo, "Versatile fatigue strength evaluation of unidirectional cfrp specimen based on micro-stress analysis of resin," *Composite Structures*, vol. 276, p. 114539, 2021.

[50] T. El Shafei, R. Arnell, and J. Halling, "An experimental study of the hertzian contact of surfaces covered by soft metal films," *ASLE transactions*, vol. 26, no. 4, pp. 481–486, 1983.

[51] K. Johnson, "Chapter 7: Tangential loading and sliding contact." Contact Mechanics, Cambridge University Press, 1985.

[52] K. Johnson, "Chapter 4: Normal contact of elastic solids, hertz theory." Contact Mechanics, Cambridge University Press, 1985.

[53] MatWeb, *Overview of materials for Epoxy Cure Resin*. https://www.matweb.com/search/datasheet_print.aspx?matguid=956da5edc80f4c62a72c15ca2b923494. Accessed Nov 2, 2022.

[54] R. G. Solutions, *Virgin PTFE Material Specification Sheet*. 2008. https://www.ramgaskets.com/wp-content/uploads/2020/08/Virgin-PTFE.pdf. Accessed Oct 26, 2022.

[55] MatWeb, *AISI 4140 Steel*. https://www.matweb.com/search/DataSheet.aspx?MatGUID=8b43d8b59e4140b88ef666336ba7371a. Accessed Nov 2, 2022.

[56] MatWeb, *Overview of materials for Nylon 66/6*. https://www.matweb.com/search/datasheet_print.aspx?matguid=26386631ec1b49eeba62c80a49730dc4. Accessed Nov 2, 2022.

[57] igus, *iglidur P210, Sleeve bearing: technical specifications*. https://www.igus.eu/product/13?artNr=P210SM-0405-04. Accessed Nov 2, 2022.

[58] Xometry, *Steel CNC Machining: 4140 PH Steel*. https://www.xometry.com/capabilities/cnc-machining-service/cnc-steel/. Accessed Nov 2, 2022.

[59] R. D. Budynas and J. K. Nisbett, "Joints: Fastener stiffness." Shigley's Mechanical Engineering Design, Section 8.4-8.5, McGraw-Hill, New York, NY, 2011.

[60] V. Micro Measurements, *250UT/250UTA Datasheet*. 2021. https://docs.micro-measurements.com/?id=2580. Accessed Nov 3, 2022.

[61] S. Yang and Q. Li, "Imu-based ambulatory walking speed estimation in constrained treadmill and overground walking," *Computer methods in biomechanics and biomedical engineering*, vol. 15, no. 3, pp. 313–322, 2012.

[62] S. Byun, H. J. Lee, J. W. Han, J. S. Kim, E. Choi, and K. W. Kim, "Walking-speed estimation using a single inertial measurement unit for the older adults," *PLoS one*, vol. 14, no. 12, p. e0227075, 2019.

[63] R. Stolyarov, M. Carney, and H. Herr, "Accurate heuristic terrain prediction in powered lower-limb prostheses using onboard sensors," *IEEE Transactions on Biomedical Engineering*, vol. 68, no. 2, pp. 384–392, 2020.

[64] M. K. Shepherd, A. F. Azocar, M. J. Major, and E. J. Rouse, "Amputee perception of prosthetic ankle stiffness during locomotion," *Journal of neuroengineering and rehabilitation*, vol. 15, no. 1, pp. 1–10, 2018.

[65] A. M. Willson, A. J. Anderson, C. A. Richburg, B. C. Muir, J. Czerniecki, K. M. Steele, and P. M. Aubin, "Full body musculoskeletal model for simulations of gait in persons with transtibial amputation," *Computer Methods in Biomechanics and Biomedical Engineering*, pp. 1–12, 2022.

[66] K. Werling, M. Raitor, J. Stingel, J. L. Hicks, S. Collins, S. Delp, and C. K. Liu, "Rapid bilevel optimization to concurrently solve musculoskeletal scaling, marker registration, and inverse kinematic problems for human motion reconstruction," *bioRxiv*, 2022.

[67] K. E. Zelik and E. C. Honert, "Ankle and foot power in gait analysis: Implications for science, technology and clinical assessment," *Journal of Biomechanics*, vol. 75, pp. 1–12, 2018.

[68] K. Z. Takahashi, T. M. Kepple, and S. J. Stanhope, "A unified deformable (ud) segment model for quantifying total power of anatomical and prosthetic below-knee structures during stance in gait," *Journal of biomechanics*, vol. 45, no. 15, pp. 2662–2667, 2012.

[69] R. M. Alexander and A. Jayes, "A dynamic similarity hypothesis for the gaits of quadrupedal mammals," *Journal of zoology*, vol. 201, no. 1, pp. 135–152, 1983.